Search for a new light particle produced in association with a top quark pair with the ATLAS Detector

Shreya Saha

Department of Physics
McGill University
Montréal, Canada

December 8, 2022

A thesis submitted to McGill University in partial fulfilment of the requirements of the degree of Doctor of Philosophy

To my family, friends and teachers

मंज़िल मिलेगी भटक कर ही सही,
गुमराह तो वो है जो घर से निकले ही नहीं।
- मिर्ज़ा ग़ालिब

Contribution of the Author

The ATLAS collaboration comprises technicians, engineers and scientists from across the world, and consists of approximately 5500 members and 3000 scientific authors. The construction and maintenance of the detector, as well as, recording and further processing of the data from the detector is a collaborative effort of several dedicated individuals over a long span of time. Furthermore, analysis softwares and tools used for reconstruction and calibration of events and uncertainty estimation are work done by respective specialised members in the collaboration. The analysis presented in this thesis uses the above softwares and tools to produce results.

The analysis relevant to the thesis has a working group consisting of five professors (Prof. Steven Robertson, Prof. Rafael Coelho Lopes de Sa, Prof. Heather Russell, Prof. Verena Martinez Outschroon and Prof. Aurelio Juste Rozas), two post-doctoral researchers (Dr. Ljiljana Morvaj and Dr. Adriana Milic) and 1 doctoral student (Shreya Saha). The professors are involved in the design of the analysis and played an advisory role. Prof. Rafael Coelho Lopes de Sa has been involved more closely with the analysis in terms of

the design and implementation, on a day-to-day basis. Prof. Heather Russell and the post-doctoral researchers are involved in developing and maintaining the technical framework of the analysis. Prof. Rafael Coelho Lopes de Sa and Prof. Verena Martinez Outschroon have been instrumental in the documentation of the analysis. The doctoral student is the principal analyzer, and has undertaken the tasks of maintenance of the technical framework, carrying out the design and validation of the analysis as well as documentation of the same.

The work presented in this thesis is the first analysis of this kind in the ATLAS collaboration, and is considered an original and distinct contribution to knowledge. A summary of contributions based on each chapter is presented below:

- Chapter 1: The author provides an introduction and motivation for the search for a new light particle in association with a top quark pair.

- Chapter 2: An overview of the relevant theoretical framework is presented by the author.

- Chapter 3: The author summarizes the Large Hadron Collider and the ATLAS detector and its respective experimental setup, which has contributions from various past and existing members of the ATLAS Collaboration as well as CERN.

  The author has contributed significantly to the development and validation of a novel trigger (related to bottom quark studies) which aided in the analysis for the possible violation in lepton flavour universality. The project was completed in collaboration

with co-members and the author was supervised by Prof. Heather Russell. This work will not be described further in this thesis.

The author has contributed to technical shifts in the detector control room, along with members of the collaboration for a limited time from 2018-2019. The author has taken online data reconstruction shifts to monitor data quality for a certain duration.

- Chapter 4: The author has detailed the physics objects definition and reconstruction, based on the work done by ATLAS co-authors in various specialised groups.

  The author has contributed to the studies regarding electron identification and reconstruction with regards to the trigger development, mentioned previously. The author has contributed to efforts in harmonizing validation and development between the specialised working group for muon reconstruction and the Higgs and Diboson Searches working group from 2020-2021.

- Chapter 5: The author presents the data and simulation used in the analysis.

  The author has contributed in the processing and maintaining data and simulation samples for the analysis, as well as within the larger working group (Higgs and Diboson Searches) within the collaboration from 2019-2021, along with members of the respective specialised working group.

- Chapter 6: The chapter consists of contribution from all the members of the analysis

working group in terms of designing the analysis strategy.[1]

- Chapter 7: The author has contributed significantly in carrying out the work regarding the signal and background modeling of the analysis, in collaboration with inputs from the professors.

- Chapter 8: Systematic uncertainties used as an input for the analysis are prescribed by the specialized working groups. Statistical uncertainties are provided as studied by the analysis working group. The effects of systematic uncertanties have been studied and presented by the author and Prof. Rafael Coelho Lopes de Sa and Prof. Steven Robertson.

- Chapter 9: The statistical framework for the analysis has been designed in part by the author, Prof. Rafael Coelho Lopes de Sa and Prof. Steven Robertson. The tools for the implementation of the design is developed by ATLAS co-authors.

- Chapter 10: The results of the analysis are produced and presented by the author.

- Chapter 11: A brief summary and outlook of the analysis is detailed by the author.

[1] An initial analysis strategy was developed in parallel with another PhD student, who later parted ways with the analysis. The strategy was revisited and modified by the author and the analysis working group.

Abstract

This thesis presents the first dedicated search for a new light pseudoscalar particle decaying into a pair of muons, and produced in association with a top quark pair. Pseudoscalars are well motivated phenomenologically in various theories beyond the Standard Model of particle physics, such as 2HDM+a and NMSSM, and can provide insights into new physics. The search targets specific decays of the signal process, where one of the top quarks decays into an electron or muon, leading to two distinct regions with three leptons: an electron and two muons ($e\mu\mu$) and three muons final states ($\mu\mu\mu$), within a dimuon invariant mass window of 12 - 77 GeV. The search uses data recorded by the ATLAS detector at CERN, from 2015 to 2018, at centre of mass energy of $\sqrt{s} = 13$ TeV, corresponding to an integrated luminosity of 139 fb^{-1}. Considering statistical and systematic uncertainties, a 95% confidence level upper limit is set on the cross-section times the branching ratio of the pseudoscalar particle decaying into muons and signal significance of the decay process is presented.

Abrégé

Cett thèse présente la toute première recherche dédiée à une nouvelle particule pseudoscalaire légère se désintégrant en une paire de muons et produite en association avec une paire de quarks “top”, Les pseudoscalaires sont bien motiv’es phénoménologiquement dans plusieurs théories au-delà du Modèle Standard de la physique des particules, telles que 2HDM+a et NMSSM, et peuvent donner d’excellents renseignements sur de la nouvelle physique. Cette recherche cible des modes de désintégration spécifiques du processus envisagé, où un des quarks “top” se désintègre en un électron ou un muon, menant à deux régions distinctes avec trois leptons: des états finaux avec un électron et deux muons ($e\mu\mu$) et trois muons ($\mu\mu\mu$), à l’intérieur d’une fenêtre de masse invariante dimuon de 12 - 77 GeV. Cette recherche utilise les données prises par le détecteur ATLAS au CERN entre 2015 et 2018, à une énergie du centre de masse $\sqrt{s} = 13$ TeV et correspondant à une luminosité de 139 fb^{-1}. En tenant compte des incertitutes statistiques et systématiques, une limite supérieure prévue à un niveau de confiance de 95% est determinée sur le produit de la section efficace et du taux de branchement de la articule pseudoscalaire se désintegrant en muons.

Acknowledgements

A mere section in this thesis is not nearly enough to express gratitude towards everyone who has been a part of this journey.

First, I would like to express my deepest gratitude towards Prof. Steven Robertson for guiding me and providing me with the freedom to push boundaries in research. I would never be able to thank Prof. Rafael Coelho Lopes de Sa enough for encouraging me to be extremely thorough with my knowledge, and always answering my unending questions about the thesis, and Prof. Verena Martinez Outschroon and Prof. Aurelio Juste Rozas for guiding me through my doctoral work. A special thanks to Rafael and Verena for inviting me to The University of Massachusetts, Amherst to work on the research paper, and for all their hospitality, from letting me stay at their home as well as for the meals and conversations. I would like to express my sincere gratitude towards Prof. Heather Russell for her guidance throughout these years, and especially for supervising my qualification task with the ATLAS collaboration. I would like to thank my summer student William Rettie, for being ever enthusiastic about the analysis, and contributing immensely in terms of the physics as well

as technical knowledge of coding in Python and C++.

I am indebted to the editorial board members for the analysis and various working group conveners for their valuable feedback on the analysis. I am extremely thankful to the ATLAS-McGill professors, Francois Corriveau, Andreas Warburton and Brigitte Vachon as well as fellow members, especially, Auriane and Christina. I would like to thank Lily and Adriana for all the support in the analysis as well as all our enlightening discussion sessions at CERN. Special thanks to Elham, Shilpi Di, and Gitanjali, for helping me feel at home in Geneva and for impromptu trips across Europe.

Words would fail to express the amount of support shown by my friend and roommate, Pragya Chawla, throughout the past six years. We have lived through our Masters and PhD studies together, and have learned and unlearned millions of things, and shared both successes and hardships, for which I will be forever grateful. The Covid lockdown would not be tolerable without you. Bryce, thank you for being there since my day 1 at McGill University. Thank you for all the physics study sessions and helping me though the graduate courses, and for sharing all what we been through together. I would like to thank Andrea from being neighbours in Montreal to completing this journey together. Thank you Matteo for the constant office banter, for the walks during Covid lockdown, and for the Italian chef in you. Thank you Alessandro, for being a lab rat to my stress cooking sessions, and for sharing life stories as we know it. Thank you Damini Di, for having my back during tough times, giving me clarity, and sharing appreciation for Korean dramas. Thank you Nilotpal

for all the hiking escapades and chilling sessions, especially during Covid. Special thanks to Avishek for the spontaneous *Bangaliyana*. A huge thanks to Antara for being there in the final years of my PhD, to share the joys and stresses of thesis writing and deadlines, along with the endless support. I would like to thank Fathima Afsal for being my roommate in the final year of my PhD, and absorbing my stressful outbursts, without complaints. A very special thanks to my Bharatanatyam Guru Rajesh Chenthy and dance friends, for teaching me life lessons through dance and stage performances, and easing my stressful days by immersing myself in the same. My sincere gratitude towards Nauveen, for always letting me to talk it out.

Last but not the least, I would be forever indebted to my parents, grandparents, sisters, Sukanya, Sanchari didi, my brother-in-law, Shantamoy, and my entire extended family for always being by my side, and giving me the perspective that the meaning of life often lies in the joy of nothingness.

Contents

List of Figures

List of Tables

Chapter 1

Introduction

Light pseudoscalar particles are present in various extensions of the Standard Model of particle physics. They are phenomenologically motivated to explain the excess of γ-ray emissions from the center of our galaxy [1, 2, 3, 4] in the context of Coy Dark Matter models [5, 6, 7], and they are an essential ingredient for electroweak baryogenesis [8, 9, 10]. In this thesis, a search for a light pseudoscalar particle, a, in association with a top quark pair ($t\bar{t}a$) is performed, where the a-boson decays into a pair of muons. The dimuon mass range is chosen to be within 12 - 77 GeV[1], bounded by the Υ and Z^0-boson resonances. Two potential signal models are targeted, based on the semi-leptonic decay modes of the top quark pair, where triggering of the event is based on the lepton coming from the top quark decay. The analysis looks for a narrow resonant peak in the $a \to \mu\mu$ decay, above a smooth

[1]Natural units are used throughout this thesis: $c = \hbar = k_B = 1$.

background spectrum, predicted by the Standard Model. A test hypothesis is developed for the a-boson, by stepping through the dimuon invariant mass region in step sizes comparable to the detector resolution. Finally, an upper limit is placed on the cross-section of the $t\bar{t}a, a \to \mu\mu$ process, using the full Run 2 dataset collected by the ATLAS detector.

The structure of the thesis is as follows: the fundamentals of the theoretical background are outlined in Chapter 2, succeeded by a description of the design and performance of the experimental setup, including the LHC and the ATLAS detector, in Chapter 3. A short discussion regarding Monte Carlo simulations is also included in the latter section of Chapter 3. Chapter 4 explains the various physics object reconstructions used in the analysis. Monte Carlo samples used in the analysis, to study the signal and Standard Model physics processes, are described in Chapter 5. The analysis strategy developed to select events for the two signal topologies is presented in Chapter 6. Chapter 7 details the signal and background modeling in the analysis, using simulation as well as data-driven techniques. Sources of various uncertainties, affecting the analysis, are mentioned in Chapter 8, followed by a description of the statistical framework in Chapter 9. Chapter 10 presents the results of the analysis, followed by a short conclusion and outlook of the thesis, in Chapter 11.

Chapter 2

Theory

The following chapter details the theoretical framework, which forms the backbone of the physics analysis presented in this thesis. Section 2.1 provides an overview of the Standard Model (SM) of particle physics, including its mathematical formulation and a detailed description of the Brout-Englert-Higgs Mechanism. The following Section 2.2 presents a brief discussion on the shortcomings of the SM, and introduces models involving new physics. Finally, Section 2.2.1 includes a discussion on the nature of simplified models and its relevance to the presented analysis.

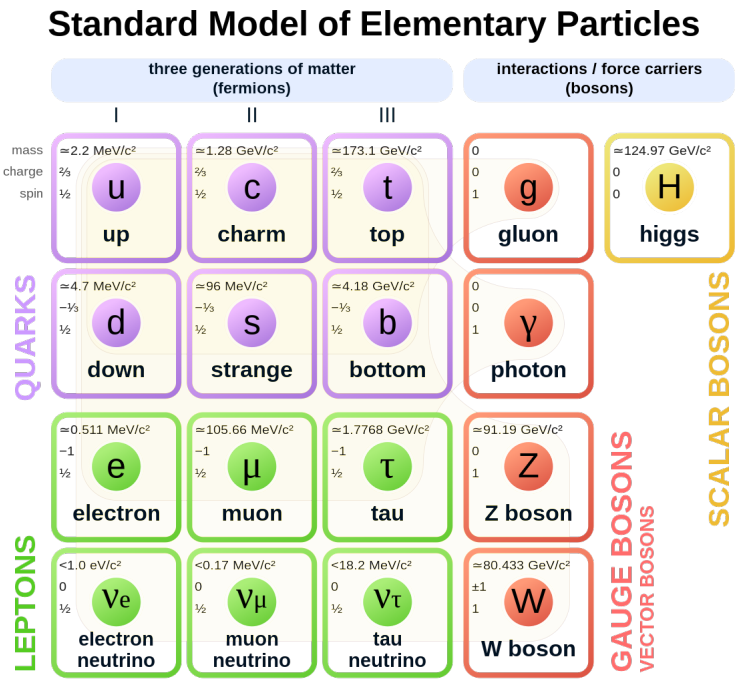

Figure 2.1: Particle content of the Standard Model [11]

2.1 The Standard Model

2.1.1 Particle Content

The Standard Model (SM) of particle physics is constructed from the combination of relativistic quantum field theories, describing the basic constituents of matter and their interactions using three fundamental forces in nature: electromagnetic, strong and weak forces. The fourth fundamental force of gravity is not incorporated into the SM.

The particle content of the SM can be broadly classified into two categories, based on the intrinsic spin of the particles. Particles with half-integer spins are known as fermions, and

integer spin particles are known as bosons. Fermions obey Fermi-Dirac statistics, whereas bosons act in accordance with Bose-Einstein statistics. Fermions are further divided into quarks and leptons as shown in Figure 2.1. The corresponding anti-particles, with opposite quantum numbers, for the quarks and the leptons exist as well, and are not shown explicitly in Figure 2.1.

Quarks are known to interact with all the forces in the SM. They possess electric charge and weak isospin, as well as an additional charge known as "color", which allows them to interact via the electromagnetic, weak and strong forces, respectively. There are six flavours of quarks, namely, up, down, charm, strange, top and bottom. Due to a phenomenon termed as *color confinement*, quarks are only observed in combination with other quarks, such that the total color charge is zero (colorless states). Naked quarks cannot be observed in nature, they combine to form hadrons, which are classified into mesons and baryons. Mesons consist of a quark and an anti-quark, and baryons are formed of three quarks/anti-quarks, both of these quark states have zero color charge. The only exception to this above rule is the top quark. The top quark has a mass of 172.5 GeV, which is much heavier as compared to the other quarks. Hence, it has a shorter lifetime of $\sim 5 \times 10^{-25}$ s [12], which is much smaller than the time needed to form bound quark states, causing the top quark to decay via the weak interaction, before it can form colourless states [13].

Leptons consist of neutrinos (ν_e, ν_μ, ν_τ) and charged leptons (e, μ, τ). Neutrinos are electrically neutral and interact via the weak force only, whereas the charged leptons possess

electric charge and interact via the weak and the electromagnetic forces.

Spin-1 vector bosons are the particles which mediate the three forces in the SM. There are a total of eight colored gluons, which mediate the strong force, the $W^{\pm}$ and Z^0-bosons participate in the weak force, and the photon is responsible for electromagnetic interactions. The Higgs boson is the only spin-0 scalar boson in the SM, and it is not one of the force mediators. Instead, the field associated with the Higgs boson gives mass to the Z^0 and the $W^{\pm}$ bosons, through the Brout-Englert-Higgs mechanism, and consequentially, the fermion masses arise via the Yukawa couplings, detailed in Section 2.1.5. The origin of neutrino masses is not explained with the above mechanism and will not be discussed further in this thesis.

2.1.2 Mathematical formulation

The mathematical formulation of the SM is based on the concepts of quantum mechanics and special relativity [14]. Hence, quantum field theory is used for mathematical formulation of the SM. A more detailed description can be found in [15, 16, 14, 17, 12]. The SM is a gauge theory, which means that the theory is invariant under the $SU(3)_C \otimes SU(2)_L \otimes U(1)_Y$ group, using local gauge transformations. $SU(3)_C$ refers to the strong interaction in the context of quantum chromodynamics, as explained in 2.1.4. $SU(2)_L \times U(1)_Y$ denote the electroweak interactions, detailed in Section 2.1.3.

2.1.3 Quantum Electrodynamics

In quantum field theory, a free propagator for a fermion with mass m can be written using the Dirac formalism, as shown in Equation 2.1 [16]. In this equation, γ^μ is the Dirac matrix and ψ refers to the fermion field.

$$(i\gamma^\mu\partial_\mu - m)\psi = 0 \tag{2.1}$$

The Lagrangian density for the above equation can be expressed as:

$$\mathcal{L} = \bar{\psi}\left(i\gamma^\mu\partial_\mu - m\right)\psi \tag{2.2}$$

If we look at a global phase transformation using the form, $\psi \rightarrow e^{iq\alpha}\psi$, the above Lagrangian is invariant, where q is the charge of the fermion and α is a constant. This is referred to as $U(1)$ symmetry group. In the SM, local gauge invariance has to be satisfied. Hence, the equation has to be modified to include a covariant derivative, $\mathcal{D} = \partial_\mu - iqA_\mu$. This introduces a new vector field, A_μ, which is the electromagnetic field vector. The Lagrangian density is re-expressed in Equation 2.3.

$$\begin{aligned}\mathcal{L} &= \bar{\psi}\left(i\gamma^\mu\mathcal{D}_\mu - m\right)\psi \\ &= \bar{\psi}i\gamma^\mu\partial_\mu\psi - m\bar{\psi}\psi - q\bar{\psi}\gamma^\mu A_\mu\psi\end{aligned} \tag{2.3}$$

Quantum Electrodynamics (QED) refers to the field theory, wherein a fermion interacts with the electromagnetic field via a massless photon. The Lagrangian density for QED can be written as shown in Equation 2.4. $\mathcal{F}^{\mu\nu}$ is the electromagnetic field tensor defined as $\mathcal{F}^{\mu\nu} = \partial_\mu A_\nu - \partial_\nu A_\mu$.

$$\mathcal{L}_{QED} = \underbrace{\bar{\psi} i\gamma^\mu \partial_\mu \psi}_{\text{fermion kinetic term}} - \underbrace{m\bar{\psi}\psi}_{\text{fermion mass term}} - \underbrace{\frac{1}{4}\mathcal{F}^{\mu\nu}\mathcal{F}_{\mu\nu}}_{\text{field kinetic term}} - \underbrace{q\bar{\psi}\gamma^\mu A_\mu \psi}_{\text{interaction term}} \tag{2.4}$$

2.1.4 Quantum Chromodynamics

The behaviour of the strong force and its mediation by the gluons, falls under the subject of *Quantum Chromodynamics* (QCD) [18]. It is a gauge theory based on the $SU(3)_C$ symmetry group. There are three types of color charge possessed by the quarks and gluons, which have no physical meaning : *red*, *green* and *blue*. In order to achieve local gauge invariance using Equation 2.2, ∂_μ is replaced by the covariant derivative $\mathcal{D}_\mu = \partial_\mu - ig_3 T_a G_{a\mu}$. g_3 is the coupling strength of the respective gluon field, T_a are the generators of the $SU(3)$ group (also known as the Gell-Mann matrices), and G_a represents the eight gluon fields, where $a \in (1, 2, ..., 8)$. The QCD Lagrangian can be written as below:

$$\mathcal{L}_{QCD} = \underbrace{\bar{\psi}_f i\gamma^\mu \partial_\mu \psi_f}_{\text{quark kinetic term}} - \underbrace{m\bar{\psi}_f \psi_f}_{\text{quark mass term}} - \underbrace{\frac{1}{4}\mathcal{G}_a^{\mu\nu}\mathcal{G}_{a\mu\nu}}_{\text{field kinetic term}} - \underbrace{g_3\bar{\psi}_f\gamma^\mu T_a G_{a\mu}\psi_f}_{\text{interaction term}} \tag{2.5}$$

Here, $\mathcal{G}_a^{\mu\nu}$ is the gluon field strength defined as, $\mathcal{G}_a^{\mu\nu} = \partial^\mu G_a^\nu - \partial^\nu G_a^\mu - g_3 f_{abc} G_b^\mu G_c^\nu$. f

represents the 6 flavors of the quarks, which is summed over all the three colors.

2.1.5 Electroweak Interaction

Above a certain energy range of 100 GeV, the electromagnetic and weak forces are united, which gives rise to electroweak interactions [19, 15]. These interactions respect the symmetry of the $SU(2)_L \otimes U(1)_Y$ gauge group. The subscript L refers to the fact that only left-handed fermions are involved in the gauge transformations in the electroweak sector. $SU(2)_L$ is also known as the weak isospin group and contains three gauge fields, W_μ^a, where $a = 1, 2, 3$. $U(1)_Y$ is the weak hypercharge group and it contains one associated gauge field, B_μ. Here, Y denotes the weak hypercharge, which is a conserved quantum number, and relates the electric charge q to the third component of the weak isospin, I_3, using Gell–Mann–Nishijima formula, $q = I_3 + \frac{Y}{2}$ [20]. The covariant derivative for the electroweak interaction can be written as :

$$\mathcal{D}_\mu = \partial_\mu - \frac{1}{2} i g_W \sigma_a W_\mu^a - \frac{1}{2} i g_Y Y B_\mu^a \tag{2.6}$$

Here, g_W and g_Y refer to the weak and electromagnetic coupling constant. $\sigma_a, a = 1, 2, 3$ are the Pauli matrices, which are the generators of the $SU(2)_L$ group. The electroweak Lagrangian can be written as a combination of 4 terms : $\mathcal{L}_{EW} = \mathcal{L}_{BW} + \mathcal{L}_F + \mathcal{L}_H + \mathcal{L}_Y$. $\mathcal{L}_{BW}$ refers to the gauge fields and L_F refers to the fermion fields as shown in equations 2.7 and 2.8, respectively. As seen in the equations below, local gauge invariance of $SU(2)_L \otimes U(1)_Y$ forbids the presence of massive gauge bosons. The masses rendered to the bosons and the fermions

in the SM, is explained by the Brout-Englert-Higgs mechanism presented in Section 2.1.6.

$$\mathcal{L}_{BW} = -\frac{1}{4}W^a_{\mu\nu}W^{\mu\nu,a} - \frac{1}{4}B_{\mu\nu}B^{\mu\nu} \tag{2.7}$$

$$\mathcal{L}_F = \sum_{j=1}^{6} \bar{\psi}^j_L i\gamma^\mu \left(\partial_\mu - ig_W \frac{\sigma^a}{2}W^a_\mu + ig_Y \frac{Y}{2}B_\mu\right)\psi^j_L + \sum_{j=1}^{9} \bar{\psi}^j_R i\gamma_\mu \left(\partial_\mu + ig_Y \frac{Y}{2}B_\mu\right)\psi^j_R \tag{2.8}$$

2.1.6 Spontaneous Symmetry Breaking

At low enough energies, $SU(2)_L \otimes U(1)_Y$ is broken, which provides mass to the gauge bosons and consequently to the fermions via the Yukawa couplings. An additional complex scalar field is added to the theory for this purpose [21, 22]. Equation 2.9 shows the form of the doublet scalar field. The Brout-Englert-Higgs mechanism explains the interactions between this new scalar field and the gauge and fermion fields, respecting gauge invariance of the SM.

$$\phi(x) = \begin{pmatrix} \phi^+(x) \\ \phi^0(x) \end{pmatrix} = \frac{1}{\sqrt{2}} \begin{pmatrix} \phi_1(x) + i\phi_2(x) \\ \phi_3(x) + i\phi_4(x) \end{pmatrix} \tag{2.9}$$

Here, $\phi_i, (i \in 1, .., 4)$ are real scalar fields. The Higgs Lagrangian, $\mathcal{L}_H$ can be written as in Equation 2.10. Here, $\mathcal{D}_\mu$ corresponds to the definition of the electroweak covariant derivative defined in Equation 2.6. $V(\phi)$ is referred as the Higgs potential defined in Equation 2.11, μ and λ are scalar constants.

$$\mathcal{L}_{\text{Higgs}} = (\mathcal{D}_\mu\phi)^\dagger (\mathcal{D}_\mu\phi) - V(\phi) \tag{2.10}$$

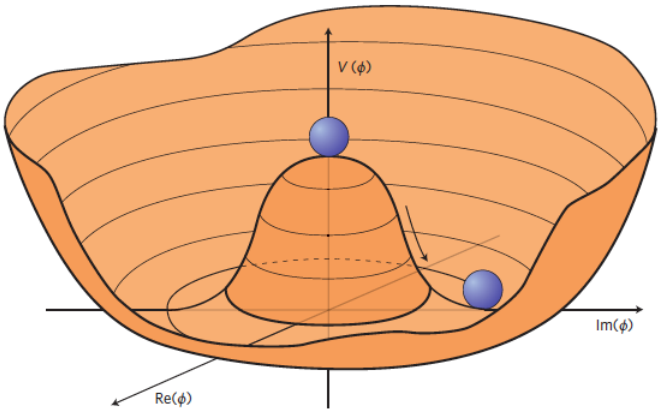

Figure 2.2: Higgs potential for $\mu^2 < 0$, where the minimum is at $|\phi^2| = \frac{-\mu^2}{2\lambda}$. If we choose any of the points at the bottom of the potential, the rotational symmetry of the $U(1)$ group will be broken [23].

$$V(\phi) = \mu^2 \phi^\dagger \phi + \frac{\lambda}{4}\left(\phi^\dagger \phi\right)^2 \tag{2.11}$$

The sign of μ^2 in Equation 2.11, determines the shape of the potential. In the case of spontaneous symmetry breaking, $\mu^2 < 0$ and $\lambda > 0$, which gives rise to a potential illustrated in Figure 2.2. The vacuum state is at the minimum of the potential, and choosing a specific value of vacuum states as shown in Equation 2.12, breaks the rotational symmetry of the potential. For the cases where $\mu^2 < 0$, we get a set of minima on a circle of radius $\sqrt{-\mu^2/(2\lambda)}$. If we choose one of the minima, it breaks the rotational $U(1)$ symmetry spontaneously.

$$\phi^2_{1,\min} = \phi^2_{2,\min} = \phi^2_{4,\min} = 0 \quad \text{and} \quad \phi^2_{3,\min} = -\frac{\mu^2}{2\lambda} = \nu^2 \tag{2.12}$$

ν in the above equation is the vacuum expectation value for the $V(\phi)$ potential in

Equation 2.11 . The vacuum can be written in the following form :

$$\phi = \frac{1}{\sqrt{2}} \begin{pmatrix} 0 \\ \\ \nu \end{pmatrix}, \quad \text{where } \nu = \sqrt{\frac{-\mu^2}{\lambda}} \tag{2.13}$$

As we know, there are currently three massless degrees of freedom associated with the ϕ field. The electroweak Lagrangian is perturbed using small oscillations, conserving gauge invariance, the new vacuum can be re-written as in Equation 2.14. Here, a neutral massive scalar field is introduced, which is the Higgs (h) field below.

$$\phi = \frac{1}{\sqrt{2}} \begin{pmatrix} 0 \\ \\ \nu + h \end{pmatrix} \tag{2.14}$$

The above choice of the vacuum field breaks the $SU(2)_L \otimes U(1)_Y$ symmetry, keeping the $U(1)_{EM}$ invariant. Hence, photons are massless, after the symmetry breaking. Using the new definition of the Higgs potential in Equation 2.14, the Lagrangian for the Higgs sector can be re-written as below:

$$
\begin{aligned}
\mathcal{L} =& \frac{1}{2}\partial_\mu h \partial^\mu h \quad - \lambda\nu^2 h^2 \\
&+ \frac{1}{2}\left(\frac{g_W^2\nu^2}{4}\left(\left|W_\mu^+\right|^2 + \left|W_\mu^-\right|^2\right) + \frac{\nu^2}{4}\left(g_Y^2 + g_W^2\right)|Z_\mu|^2\right) \\
&+ \frac{g_Y^2\nu}{4}\left(\left|W_\mu^+\right|^2 + \left|W_\mu^-\right|^2\right)h + \frac{g_Y^2}{8}\left(\left|W_\mu^+\right|^2 + \left|W_\mu^-\right|^2\right)h^2 \\
&+ \frac{\nu^2}{4}\left(g_Y^2 + g_W^2\right)|Z_\mu|^2 h + \frac{1}{8}\left(g_Y^2 + g_W^2\right)|Z_\mu|^2 h^2 \\
&- \lambda\nu h^3 \quad - \frac{\lambda}{4}h^4 \\
&+ \text{ constant.}
\end{aligned}
\tag{2.15}
$$

The masses of the electroweak gauge bosons can be read as shown in Equation 2.16. $m_{W^\pm}$, m_{Z^0}, m_A, m_h refers to the masses of the two charged $W^\pm$-bosons, and the neutral Z^0-boson, photon and Higgs boson, respectively.

$$
m_{W^\pm} = \frac{1}{2}\nu g_W, \quad m_Z = \frac{1}{2}\nu\sqrt{g_Y^2 + g_W^2}, \quad m_A = 0, \quad m_h = \nu\sqrt{2\lambda} \tag{2.16}
$$

The fermions in the SM (except the neutrinos), acquire mass in the same manner, by interacting with the Higgs field. The fermionic mass is described as, $m_{fi} = y_{fi}\nu/\sqrt{2}$. Here, i refers to the quark and lepton generations, and y is the Yukawa coupling. The Yukawa coupling can be explained as the strength of interaction between the Higgs field and the fermions. The interaction between the fields is directly proportional to the mass of the fermions, top quark being the heaviest fermion, with the highest value of Yukawa coupling in the SM.

2.1.7 Weak Interactions

The $W^{\pm}$ and Z^0 bosons are the force carriers of the weak interaction. Due to the high mass of these bosons, the weak force is a short-range force ($\sim 10^{-17}$m). The $W^{\pm}$ and Z^0 bosons mediate the charged and neutral current, respectively. In interactions involving the $W^{\pm}$, change of the flavour of the quarks is permitted, which futher depends on quark mixing properties described by the CKM matrix, unlike the neutral current, where flavor changing of the quarks is forbidden [24].

2.2 Physics beyond the Standard Model

The SM provides a good description of all known particle interactions, but it does have several shortcomings which will be discussed briefly in the following section. One of the most fundamental issues with the SM, is the hierarchy problem [25]. We know that the electroweak symmetry breaking occurs at an energy scale of order 100 GeV and the Planck energy scale is known to be 10^{19} GeV. This difference in magnitude cannot be explained by the current framework of the SM. The observed Higgs boson mass at 125 GeV [26] should also receive quantum corrections from SM particles in the order of 10^{17}, which is not the case. Moreover, the SM requires 19 input parameters, which include the masses, mixing angles and couplings, which do not have any theoretical ground [27]. The origin of the broad range of the fermion masses from the negligible electron neutrino mass to the massive top quark

mass is currently unexplained. There is also a strong CP (charge-parity) problem associated with QCD. The present formulation of QCD allows CP violation in particles interacting via the strong force, however there has been no experimental evidence for the same. There is no explanation in the SM, as to why CP should be conserved in such interactions, this is an instance of the *fine-tuning* issue in the SM [28, 29].

There are various proposed theories beyond the SM, which shed light on the above-mentioned puzzles. Supersymmetry is one of the extensions of the SM, which addresses the hierarchy problem, by introducing supersymmetric partners for each particle in the SM. Each fermion has a bosonic partner and each boson has a fermionic partner, leading to new interactions in the extended SM, which address the hierarchy problem. An in-depth discussion of Minimal Supersymmetric Model (MSSM) and Next-to-Minimal Supersymmetric Model (NMSSM) can be found in [27]. Another approach is to introduce new scalar particles in the form of simplified models, which will be discussed in Section 2.2.1.

2.2.1 Simplified Models

A simplified model is defined as an extension to the SM, by introducing an effective Lagrangian, which includes interactions of some new particles [30]. They can be described adequately in terms of the cross-sections of new physics processes as well as the masses of the new particles, which are are known to be one of the many observables in a particle

detector. This makes these models very effective in probing signs of new physics in detectors. There is a huge variety of simplified models motivated by the choice of theoretical models as well as the targeted particles in the detector.

In this specific thesis, a search is conducted for a new light CP-odd pseudoscalar particle (denoted by a), which is produced in association with a top quark pair ($t\bar{t}$). The chosen decay mode for the a-boson is into a pair of muons. Such particles, like the a, are phenomenologically motivated for explaining the observed γ-ray emissions from the center of the Milky Way [1, 2, 3, 4] with reference to Coy Dark Matter models [5, 6, 7]. They also play a part in electroweak baryogenesis [8, 9, 10]. These pseudoscalars are present in a number of Beyond the SM models, such as 2HDM+a [31, 32, 33] and NMSSM [34, 35], where the SM-like Higgs can mix with the new particle, wherein the new particle can achieve Yukawa-like couplings to the fermions as in the SM. Hence, top quark production along with the new pseudoscalar particle is motivated by the highest value of Yukawa coupling due to its dependency on the top-quark mass. Additionally, the a-boson is searched via the decay into a pair of muons, due to good detector resolution and discrimination against various other SM physics processes, as discussed in chapters 6 and 7. Various other decay modes of the particle can be considered, such as its decays into a pair of τ-leptons or a pair of bottom quarks, but it is beyond the scope of this thesis.

The Lagrangian of this specific simplified model can be written as a sum of the SM Lagrangian and an effective Lagrangian containing the interaction between the top quark

and the a-boson as shown below [32]:

$$\begin{aligned} \mathcal{L} &= \mathcal{L}_{\mathrm{SM}} + \mathcal{L}_{\mathrm{a}} \\ \mathcal{L}_{\mathrm{a}} &= i\frac{g_t y_t}{\sqrt{2}}\bar{t}\gamma_5 t a \end{aligned} \tag{2.17}$$

Here, g_t corresponds to the parametrization of the Yukawa coupling, y_t, which is defined previously in Section 2.1.5. In this analysis, the a-boson decays into a pair of muons 100% of the time. Further details about the various decay modes of the top quark pair is described in Chapter 6.

Chapter 3

Experimental Setup

3.1 Collider Physics

As high energy physicists, we are devoted to the study of elementary particles and their interactions in nature. Studying the outcome of particle collisions helps us to understand fundamental processes, in the Standard Model (SM) of particle physics, as well as beyond it. Physics beyond the SM is often interesting to shed light on unsolved questions, such as the baryon asymmetry of the universe and the nature of dark matter (DM) and dark energy.

There are two major kinds of accelerator-based experiments in particle physics - Fixed Target experiments and Collider experiments. In this section, we will focus on the different aspects of a collider experiment and discuss some of its basic principles. A circular particle collider consists of one or more rings, lined by magnets to direct the two counter-rotating

beams of charged particles, which are generally protons or electrons, although other fermions and heavy nuclei (lead or xenon) are also possible. In the context of this thesis, the beam of charged particles will refer to proton beams. The beams intersect at specific points within the Large Hadron Collider; these intersection points are where we place our detectors to study the properties of the particles produced from the collisions.

Each proton beam consists of 2808 bunches, and each bunch is made of 1.5×10^{11} protons. The distance between two consecutive bunches is set to 7.5 m. Hence, the time between the bunches, referred to as the bunch spacing, is calculated to be 25 ns, considering that each bunch is accelerated to a velocity of 0.999 c, where c is the speed of light.

Another important parameter used in accelerator physics is the instantaneous luminosity (L'), which is defined as the number of collisions per cm^2 per second, as shown in Equation 3.1. Here, N_1 and N_2 are the number of protons per bunch, f is the bunch crossing frequency, which is the inverse of the bunch spacing of 25 ns. σ_x and σ_y are the x and y components of cross-section of the colliding bunch.

$$L' = \frac{f N_1 N_2}{4\pi \sigma_x \sigma_y} \tag{3.1}$$

An estimate of the instantaneous luminosity is shown below, under the assumption that the

number of protons in each crossing bunch is identical -

$$N_1 = N_2 = 1.5 \times 10^{11}$$

$$f = \frac{1}{25 \times 10^{-9}} \text{ s}^{-1}$$

$$\sigma_x = \sigma_y = 16 \times 10^{-4} \text{ cm}$$

$$L = 10^{34} \text{ cm}^{-2} \text{ s}^{-1}$$

Since we are analysing the total data collected by the detector over its operation period, it is convenient to define the integrated luminosity, L, as below -

$$L = \int L' dt \tag{3.2}$$

L is often measured in b^{-1}, which is defined as the inverse of a barn, where 1 barn (b) $= 10^{-28}$ m^2. For the purpose of this analysis, data collected by the ATLAS detector in Run 1 (2009-2013) [36] and Run 2 (2015-18) [37] is used, which is recorded to be 139 fb^{-1}. Figure 3.1 shows the total integrated luminosity delivered by the detector during Run 2.

The cross-section (σ) is the measurement of the probability of a particular physics process to occur. The number of events per second for a specific process is given by Equation 3.3, where L is the luminosity.

$$N_{\text{events/s}} = L.\sigma \tag{3.3}$$

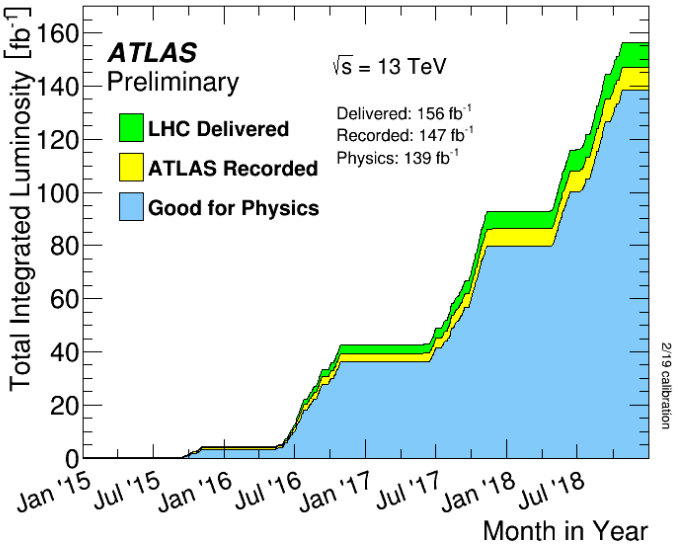

Figure 3.1: Total Integrated Luminosity delivered by the ATLAS Detector from 2015 - 2018 [37]

3.2 The Large Hadron Collider

The Large Hadron Collider (LHC) is a particle accelerator located at the Swiss-French border at the European Centre for Nuclear Research (CERN). It consists of a 27 km circumference tunnel located 100 m below the ground level, along with an elaborate accelerator complex as shown in Figure 3.2. The LHC houses four major experiments - A Large Toroidal LHC Apparatus (ATLAS) [38], Compact Muon Solenoid (CMS) [39], LHCb [40], and A Large Ion Collider Experiment (ALICE) [41]. ATLAS and CMS are general purpose detectors, testing the validity and limits of the Standard Model, LHCb is focused on studying bottom quarks and their properties, and ALICE is devoted to studying heavy ion collisions and quark gluon plasma.

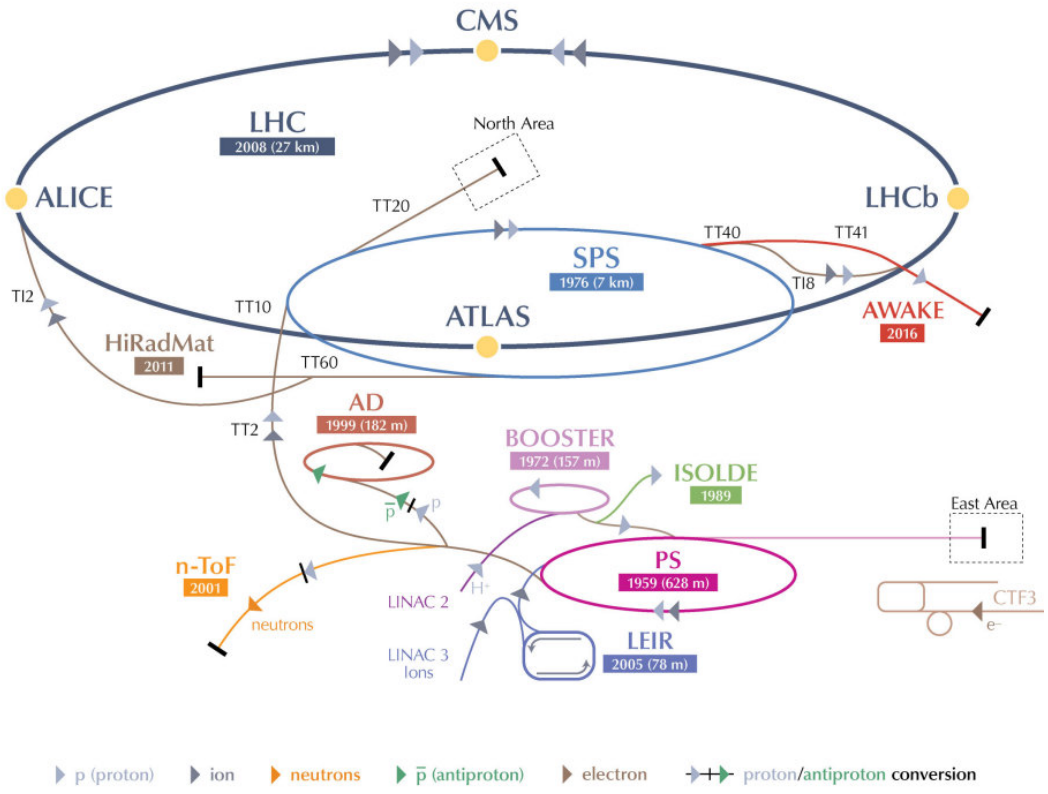

Figure 3.2: CERN Accelerator Complex [42]

Acceleration of the proton beams in the LHC tunnel, to travel at 0.999 c, is done in a step by step process as shown in Figure 3.2. First, the protons are sourced from a bottle of hydrogen gas by stripping off the electrons, and are accelerated to an energy of 50 MeV in the linear accelerator, LINAC 2. The next step is to increase the energy of the protons to 1.4 GeV, which happens in the Proton Synchotron Booster, after which the proton beam is injected into the Proton Synchrotron (PS). Here, the beam is accelerated to 25 GeV. Following the PS, the beam enters the Super Proton Synchrotron (SPS), to reach 450 GeV.

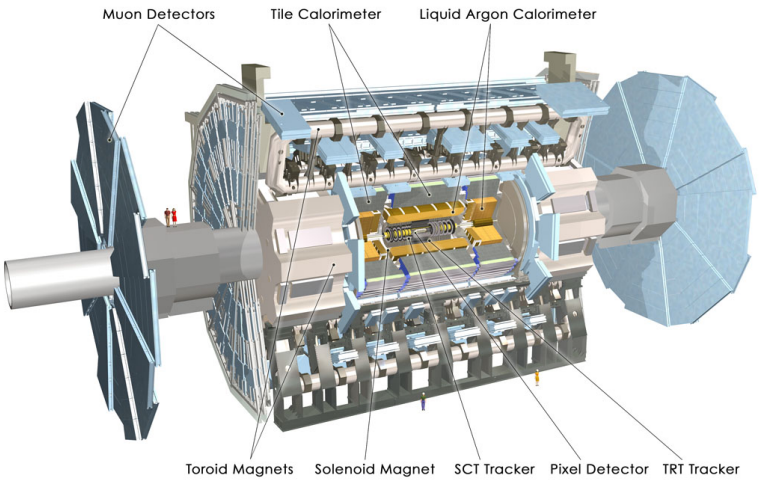

Figure 3.3: The ATLAS Detector [44]

The SPS injects the proton beam into the LHC tunnel into two counter-rotating beams. The LHC tunnel consists of several kinds of extremely powerful superconducting magnets to direct and focus the two beams. The dipole magnets are used to direct the proton beams in a circular path, and have a maximum magnetic field strength of 8.33 T [43]. The quadrupole magnets serve a different purpose of focusing the proton beams along the tunnel and near the four major interaction points at the site of the four detectors, to get maximum possible interactions.

3.3 The ATLAS Detector

The ATLAS detector is one of the four major detectors in the LHC. The following sections describe the coordinate system as well as the multi-layered structure of the detector.

3.3.1 Coordinate system

The ATLAS detector is a cylindrical detector, which is forward-backward symmetric about the interaction point. It is 46 m in length and 25 m in diameter. The coordinates of the detector follow a right-handed Cartesian system, with respect to the interaction point. The positive x-axis points from the collision point to the centre of the LHC ring, and the positive y-axis points upwards. The z-axis points along the beam line, and the positive and the negative z-axis are referred to as the A and C side of the detector respectively. For the sake of simplified calculations in the transverse $x - y$ plane, and owing to the cylindrical symmetry of the detector, position of particles are given in spherical coordinates of R, θ, ϕ. Here, ϕ is referred as the azimuthal angle, which is measured in the range of [-π, π], around the beam axis. The polar angle, θ, ranges from [0,π] and is measured from the beam axis. Both ϕ and θ are in units of radians.

Rapidity (y) and pseudorapidity (η) are two concepts used in hadron collider experiments to define the kinematics of outgoing particles. Rapidity tends to the pseudorapidity value for large momentum particles, where the mass of the particle is considered to be negligible with respect to its momentum. The following equations define both the above quantities, where E is the particle energy and p_z is the z-direction momentum -

$$y = \frac{1}{2}\ln(\frac{E + p_z}{E - p_z}) \tag{3.4}$$

$$\eta = -\ln(\tan(\frac{\theta}{2})) \tag{3.5}$$

ATLAS detector has an $|\eta|$ coverage from 0 to 4.9, where $\eta = 0$ in the y-axis direction, and is referred to as the central part of the detector. The value of $|\eta|$ increases in the forward or backward direction of the detector. Another important measure of particle kinematics is the angular distance between the final state particles, ΔR, which is defined in the η-ϕ plane as shown in Equation 3.6.

$$\Delta R = \sqrt{\Delta\eta^2 + \Delta\phi^2} \tag{3.6}$$

Final state particles are also distinguished based on their transverse momentum, $\vec{p}_T$. During the collision, the exact initial longitudinal momentum in the initial state, is unknown along the z-axis, whereas the initial $\vec{p}_T$ of the protons is 0. Hence, $\vec{p}_T$ can be calculated as shown in Equation 3.7. Here, the momenta of the particle in the x and y-direction is given by $\vec{p}_x$ and $\vec{p}_y$ respectively.

$$|\vec{p}_T| = \sqrt{\vec{p}_x^2 + \vec{p}_y^2} \tag{3.7}$$

The ATLAS detector has three main sub-systems for tracking and measuring purposes - the Inner Detector, the Calorimeters and the Muon Spectrometer, which in turn contain various sub-detectors. The following sections describe each of the sub-systems in detail.

3.3.2 Inner Detector

The section of the detector closest to the interaction point is known as the Inner Detector (ID). The functionality of the ID is to precisely measure the direction and momenta of charged particles as well as their respective production points (vertices). The transverse momentum threshold for charged particles is 0.5 GeV, and within $|\eta| < 2.5$. The ID also provides electron identification for $|\eta| < 2.0$ and transverse momentum ranging between 0.5 GeV and 150 GeV.

The total η coverage of the ID is $|\eta| < 2.5$, and it has complete coverage in the azimuthal angle, ϕ. The ID is enclosed in a cylindrical envelope of length 3512 mm and radius 1150 mm, within a solenoid magnet of 2 T, oriented in the z-direction [38]. There are three main subsections of the ID - the insertable B-layer (IBL) and the silicon pixel detector, the semiconductor tracker (SCT) and the transition radiation tracker (TRT).

The innermost layer is the IBL, which comprises an array of 26880 silicon pixels organized in an array of 80 columns and 336 rows. It is placed within a mean radius of 33 mm and has a coverage of $|\eta| < 3.0$ [46]. The main purpose of the IBL is to precisely detect primary and secondary hard scatter vertices, especially in mesons and baryons containing bottom quarks.

The IBL is followed by three layers of silicon pixel detector, which has an $|\eta|$ range of $|\eta| < 2.5$. These layers have extremely fine granularity for precise generation of space-point hits of the particle tracks. The layers are segmented in R-ϕ and z with intrinsic accuracies of 10 μm in R-ϕ and 115 μm in z plane.

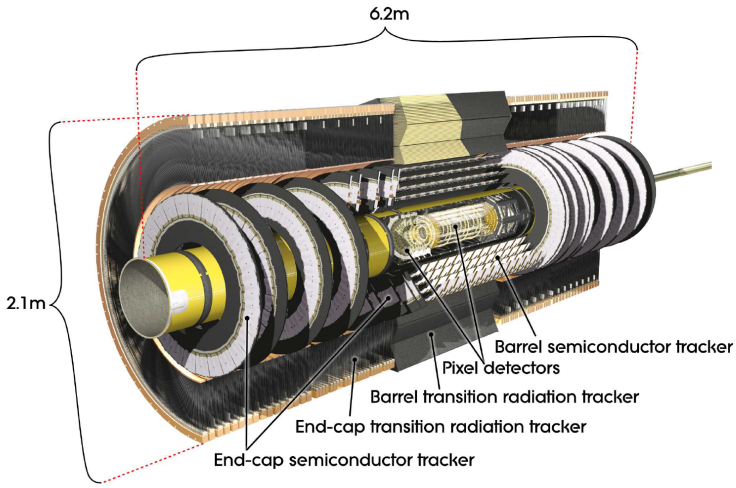

Figure 3.4: Cross-section of the ATLAS Inner Detector [45].

The next layer is the SCT, consisting of four layers of silicon microstrip detectors with a total surface area of 60 m^2. The SCT plays a major role in producing momentum measurements of the charged particle tracks and its respective trajectories. It covers an $|\eta|$ region of $|\eta| < 2.5$, and has a spatial resolution of 17 μm in R-ϕ and 580 μm in z plane.

The final layer of the ID is the TRT, which is a detector using a drift tube system. It is made up of 144 cm long, 4 mm diameter straw tubes, covering an $|\eta|$ range of $|\eta| < 2.0$. It provides spatial resolution in the R-ϕ plane up to 130 μm per straw. The TRT is responsible for providing robust tracking information, along with stand alone particle recognition (electron/pion recognition). The straws are filled with a specific gas mixture of Xenon, CO_2 and O_2 to aid in increasing the drift velocity of electrons as well as for photon-quenching. Differentiation between different particles utilizes the information from

the energy deposits in the TRT. Photon energy deposits are usually around the value of 8-10 keV, whereas pions deposit around 2 keV of energy [47]. For electron identification, the number of energy depositions for a given track, is used as a critical parameter.

3.3.3 Calorimetry

In addition to measuring the trajectories of the outgoing particles, measurement of their energy deposits is essential to precisely identify and reconstruct a physics event in the collision. When a particle passes through the various layers of the detector, it deposits energy progressively, leading to a cascade of secondary particles, which is known as a "shower". Calorimetry refers to the measurement of the deposited energy to infer their properties and the decay process. The ATLAS calorimeters are designed specifically to absorb the energy from the shower entirely and measure it to the best possible resolution. There are two main kinds of showers: electromagnetic (EM) showers and hadronic showers. Hence, there are two categories of calorimeters in the ATLAS detector: the Liquid Argon EM calorimeter and the Hadronic calorimeter.

At energies below 10 MeV, electrons and positrons mainly lose energy via ionization, Bhabha scattering, Moller scattering, and positron annihilation. At energies above 10 MeV, energy losses are dominated by Bremsstrahlung, as seen in Figure 3.5. Energy losses by photons is governed by e^+e^- pair production, above the production threshold (i.e. $2\times$ m_e). The longitudinal profile of an EM shower is characterized by the radiation length (X_0),

described in Equation 3.8. It is defined as the mean distance traveled by the electron before losing $1 - 1/e$, of its energy via Bremsstrahlung. In the case of photons, it refers to $\frac{7}{9}$ of the mean free path for pair production. The estimated thickness to contain 95% of the EM shower is defined in Equation 3.9. EM calorimeters are generally designed to be 15 - 30 times the radiation length. Additionally, the thickness of the material used in the calorimeter, is relevant to the density of the material.

$$X_0 = 716.4 \text{ g cm}^{-2} \frac{A}{Z(Z+1)\ln\frac{287}{\sqrt{Z}}} = 1433 \text{ g cm}^{-2} \frac{A}{Z(Z+1)(11.319 - \ln Z)} \tag{3.8}$$

Here, A and Z refer to the mass and atomic number of the material, respectively.

$$t_{95\%} = t_{\max} + 0.08Z + 9.6\,;\, t_{\max} = \ln\frac{E_c}{E_0} + C_i \tag{3.9}$$

E_c is the critical energy, defined as, the energy at which the energy loss by Bremsstrahlung is equal to the energy lost by ionization. E_0 is the incident energy of the particle. C_i is a constant set to 0.5 and -0.5 for photons and electrons, respectively. The transverse spread of an EM shower is described by the Moliere's radius as shown in the Equation3.9. Almost 99% of the energy of the shower is absorbed within $3.5R_M$.

$$R_M = \frac{21\text{MeV}}{E_c} X_0 \tag{3.10}$$

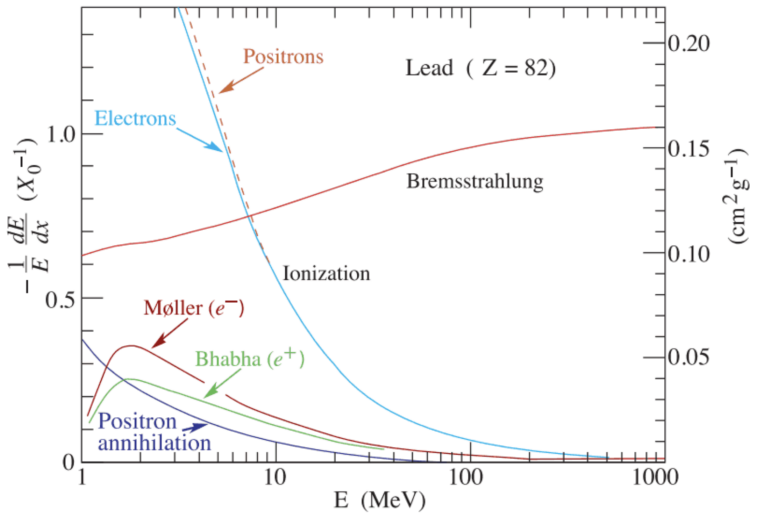

Figure 3.5: Fractional energy loss per radiation length in Lead [12].

In case of hadronic showers, the longitudinal profile is given by the characteristic nuclear interaction length, λ_I. The depth of hadronic calorimeters is restricted to 5 - 8 λ_I.

Electromagnetic Calorimeter

The electromagnetic calorimeter (refer Figure 3.6) encloses the ID and is responsible for absorbing and measuring the energy deposits from the showers generated from electrons, photons and hadrons, as well as provide an accurate position of the detected particles. The range of coverage of the EM calorimeter is up to $|\eta|$ <3.2 and the resolution of the calorimeter is given in Table 3.1. The alternating layers of the calorimeter consists of a metal absorber, made of copper, lead or tungsten, and liquid Argon (LAr) sandwiched as the active material [48]. The active material is primarily used for measuring the energy deposits, via the ionisation of the particles which pass through the medium. Liquid Argon is

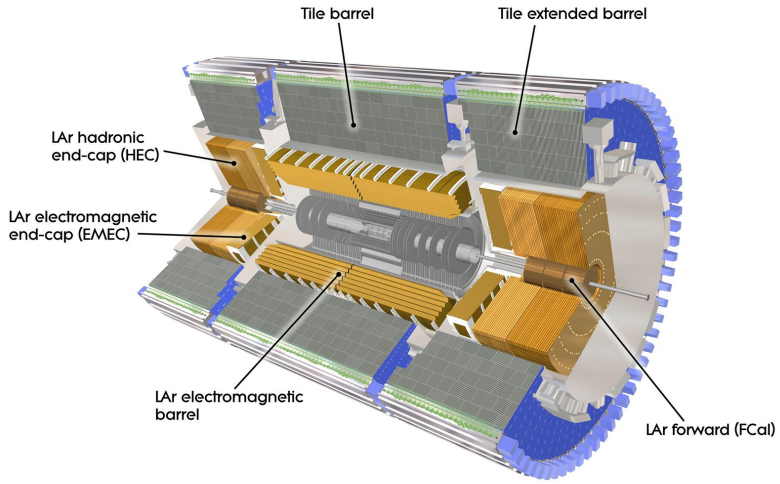

Figure 3.6: Cross-section of the ATLAS Calorimeter [49].

chosen as the active medium due to its radiation hardness and a high ionization yield. For maintaining the Argon in liquid state, the calorimeter is placed in a cryostat, maintained at -184°C. The ionisation current is then measured by an extensive readout system, outside the cryostat.

Hadronic Calorimeter

The hadronic calorimeter (refer Figure 3.6) is placed outside the EM calorimeter, to absorb the energy coming from hadronic showers, which deposit approximately 1/3 of their energy in the EM calorimeter. Table 3.1 lists the resolution and η coverage of the Hadronic calorimeter. There are three subsystems of the calorimeter - the hadronic tile calorimeter (TileCal), the LAr hadronic end-cap calorimeter (HEC) and the LAr forward calorimeter (FCAL).

The tile calorimeter consists of the barrel and the extended barrel regions which cover an

Detector component	Required resolution	η coverage	
		Measurement	Trigger
Tracking	$\sigma_{p_T}/p_T = 0.05\%\ p_T \oplus 1\%$	± 2.5	
EM calorimetry	$\sigma_E/E = 10\%/\sqrt{E} \oplus 0.7\%$	± 3.2	± 2.5
Hadronic calorimetry (jets)			
barrel and end-cap	$\sigma_E/E = 50\%/\sqrt{E} \oplus 3\%$	± 3.2	± 3.2
forward	$\sigma_E/E = 100\%/\sqrt{E} \oplus 10\%$	$3.1 < \lvert\eta\rvert < 4.9$	$3.1 < \lvert\eta\rvert < 4.9$
Muon spectrometer	σ_{p_T}/p_T=10% at p_T = 1 TeV	± 2.7	± 2.4

Table 3.1: Resolution and η coverage of ATLAS subdetectors. E and p_T and in units of GeV. [38]

$|\eta|$ range of $|\eta| < 1.0$ and $0.8 < |\eta| < 1.7$, respectively. It uses steel plates as the absorbing medium and plastic scintillator tiles as the active material [50]. When a particle passes through the absorber, it generates a shower of particles, which is converted to photons in the scintillators. The photons are collected by wavelength shifting (WLS) fibres at each end of the tile, which is then delivered to the photomultiplier (PMT) tubes, where the photons are converted into electrical signals. These signals are further stored by the readout electronics.

The second section of the calorimeter is the LAr HEC, which comprises copper plates as the metal absorber and liquid argon as the active material. It is placed behind the end caps of the EM calorimeter, and has an $|\eta|$ coverage of $1.5 < |\eta| < 3.2$.

The LAr FCAL is situated inside the HEC, and covers an $|\eta|$ range of $3.1 < |\eta| < 4.9$. The FCAL is further divided into three longitudinal sections, FCAL1 ($3.15 < |\eta| < 4.83$), FCAL2 ($3.24 < |\eta| < 4.81$) and FCAL3 ($3.32 < |\eta| < 4.75$). FCAL1 is the electromagnetic module, which uses copper as the absober. FCAL2 and FCAL3 are the hadronic modules,

which use Tungsten absorbers to contain the lateral spread of the hadronic shower. Owing to the high radiation toleration of liquid Argon, it is used as the active material in all three modules.

3.3.4 Muon Spectrometer

High energy muons lose energy mostly by ionization, Bremsstrahlung and photonuclear interactions. Since muons are approximately 200 times heavier than the electrons, the Bremsstrahlung cross-section for muons is suppressed by a factor of $1/M^2$ [51]. Consequently, muons do not tend to initiate showers in the calorimeters and mostly pass through the ID and the calorimeters. Hence, the outermost layer of the detector, the Muon Spectrometer (MS) is dedicated to tracking and transverse momentum, p_T, measurement of the muons (refer Figure 3.7). The muon p_T resolution is up to 10% for muons with $p_T = 1$ TeV, as shown in Figure 3.8. Along with the MS, p_T measurement in the ID is included for an overall determination of the muon momenta, as seen in Figure 3.8. There are four major sections of the MS: Monitored Drift Tube chambers (MDTs), Cathode Strip Chambers (CSCs), Resistive Plate Chambers (RPCs), and Thin Gap Chambers (TGCs).

The MDTs are used for precise momentum measurements in the MS. Each chamber has two multi-layers, and each layer consists of three to four layers of drift tubes. These tubes are made of aluminium and are filled with a gas mixture of Argon and CO_2 (93% - 7%) [53]. The resolution achieved per tube, is 80 μm, and the resolution of a multi-layer is 50 μm.

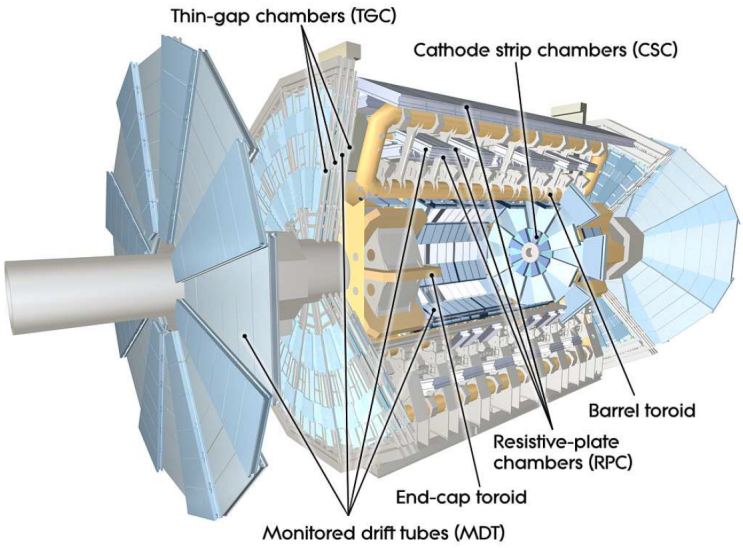

Figure 3.7: Cross-section of the ATLAS Muon Spectrometer [52].

MDTs cover an $|\eta|$ region of $|\eta| < 2.7$.

The CSCs are multiwire proportional chambers, which are used for muon tracking in the innermost end-cap regions from $|\eta|$ range of $2.0 < |\eta| < 2.7$. This is due to the fact that particle rates in this region are beyond the counting rate of the MDTs, which is 150 Hz/cm^2. The operation of CSCs is safe up to 1000 Hz/cm^2, which covers the particle rate in the $|\eta|$ region of $|\eta| < 2.7$. These are composed of two disks with eight chambers per disk. Each chamber consists of four planes of longitudinal and transverse cathode strips, along with anode wires woven in-between the panels. When muons pass through these chambers, the resultant ionisation is measured by the readout electronics. The tracking resolution of a chamber, in the plane containing the beam axis (bending plane), is approximately 40 μm,

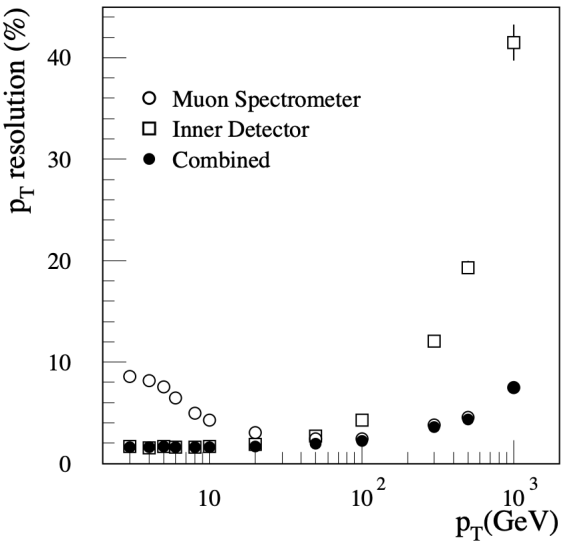

.

Figure 3.8: Muon p_T resolution with track reconstruction in the ID and in the MS [53]

and 5 mm in the transverse plane.

As muons do not lose much energy in the detector, RPCs are able to select muon tracks, based on various physics process of interest, within the barrel region of $|\eta| < 1.07$. This selection of dedicated muon tracks, is also known as "triggering" on the muons. The RPCs form three concentric layers (RPC1, RPC2 and RPC3) around the beam axis and is composed of a gas volume, Bakelite plates and readout electronics plates. RPC1 and RPC2 are responsible for triggering on low p_T muon tracks in the range of 6 - 9 GeV and RPC3 triggers on muon tracks with p_T between 9 - 35 GeV. The timing resolution is up to 7 ns and the spatial resolution is 10 mm in the bending plane as well as the transverse plane.

TGCs are mounted in the end-cap of the spectrometer covering an η region of 1.07

$< |\eta| < 2.7$. The goal of the TGCs is to trigger on muon tracks, as well as to provide a complementing azimuthal measurement of the tracks, in addition to the measurement from the MDTs, in the bending plane. These are multiwire proportional chambers, filled with a quenching gas mixture of CO_2 n-pentane. The timing resolution of the TGC is 4 ns and the chamber tracking resolution is 2-6 mm and 3-7 mm in the radial and azimuthal directions, respectively.

Bending of particle trajectories in the MS is assisted by the barrel and end-cap toroid magnets [54]. These superconducting magnets, cooled in liquid helium at 4.5 K, provide a magnetic field of 0.5 T and 1.5 T in the barrel and end-cap regions of the MS, respectively.

3.3.5 Trigger and Data Acquisition

The inelastic proton-proton cross-section is approximately 80 mb at the center-of-mass energy of $\sqrt{s} = 13$ TeV at the LHC. Hence, the LHC will produce 10^9 inelastic events per second, at the design luminosity of 10^{34} cm^{-2} s^{-1}, using Equation 3.3. Given that the bunch crossing is 25 ns, this indicates that there will be approximately 23 events per bunch crossing, for every potential new physics event. This poses a challenge to store the gigantic amount of data, in terms of resource availability. The Trigger and Data Acquisition (TDAQ) system for the ATLAS detector is dedicated to processing, selecting and storing events of interest for offline analyses. The TDAQ system collects only a small fraction of events, consisting of most interesting physics signatures. In the ATLAS Trigger, there are two distinct hierarchies

- the Level 1 trigger and the High Level Trigger (HLT).

The Level 1 trigger is hardware based and consists of the calorimeter (L1Calo) and the muon spectrometer (L1Muon) triggers. L1Calo is responsible for identifying energy clusters of interest, by using specific thresholds on the energy deposits and η and ϕ values. These triggered regions are known as Region of Interests, defined in η and ϕ. Similarly, L1Muon uses the information from the RPCs and TGCs to select events of interest. Events of interest correspond to events containing high p_T muons, electrons, showers containing hadrons, photons and τ-leptons, above a programmable threshold, depending on analyses requirements. It also includes information about total energy deposited as well as topological requirements, such as the angular distance between tracks as well as invariant masses. The L1 Trigger can accept input events up to an event rate of 40 MHz, and it reduces the rate further to 75 kHz. The maximum latency in the trigger decision is set to 2.5 μs, this latency includes the transfer of signal from the L1Calo and L1Muon to readout electronics.

The events accepted by L1 trigger are read out by the Front End detector electronics and fed into Read Out Drivers (RODs) for formatting. The data is then sent to Read Out System (ROS) before being fed into the HLT. The HLT consists of both online and offline algorithms, which analyse the momentum and angular distribution of the final state particles to reconstruct the event. There are various trigger "menus" which decide whether the event is interesting enough to be kept for offline analyses [55]. HLT reduces the event rate to approximately 1 kHz and has a decision latency of about 0.2 s [55]. The data accepted

by the HLT is sent to the Tier-0 facility at the computing centre at CERN, at the rate of 1.2 GB/s.

3.4 Simulation

3.4.1 Monte Carlo Generators

Particle physicists rely heavily on Monte Carlo (MC) simulations to mimic interesting physics processes guided by the Standard Model (SM), as well as to hunt for physics beyond the SM. MC simulations are used to generate final state particles, which are seen in the detector, and form the base of most physics analyses [56]. Simulations generally comprise two parts - event generation and detector simulation. Event generation refers to the generation of the required physics process, whereas detector simulation, refers to the simulation of final state particles through the detector medium.

3.4.2 Event Generation

Event generation is performed by various computer softwares, such as PYTHIA [57], HERWIG [58], Sherpa [59], MC@NLO [60] and POWHEG [61]. Generation of a physics process comprises a chain of steps. Feynman diagrams, relevant to the process, at leading order (and in some cases, next to leading order) are fed into the generators, along with the initial substructure composition of the colliding hadrons. The substructure is explained in

terms of partons, which are point-like constituents of the hadrons, matched to quarks and gluons.

The following sections provide a more detailed picture of the step by step process in an event generation -

Hard Scattering: In the regime of Quantum Chromodynamics(QCD), parton collisions are widely categorised into soft and hard scatter processes. Hard scatter refer to high momentum transfer between the partons, during the collision [62]. Perturbative QCD techniques are used to calculate the event rates and cross-sections of hard scatter. Figure 3.9 shows the various cross-sections of physics processes at the LHC. Additionally, various physics theory models can also be provided to the generators, for tuning the generation. Other parameters, such as the mass of incoming and outgoing particles, $\vec{p}_T$ threshold, lifetime and spin, can also be included in the generator interface.

Parton Shower: Hard scatter processes often produce radiation before and after the collision, known as Initial State Radiation (ISR) and Final State Radiation (FSR), respectively. This in turn radiates additional gluons or forms more quark combinations. Parton showers are a combination of all the above-mentioned perturbative processes and are generated by dedicated algorithms [64].

Hadronization: The momenta of the outgoing particles in the parton shower progressively decrease until the perturbative QCD limit is reached, after which, non-perturbative effects come into play. We are unable to observe naked quarks in nature

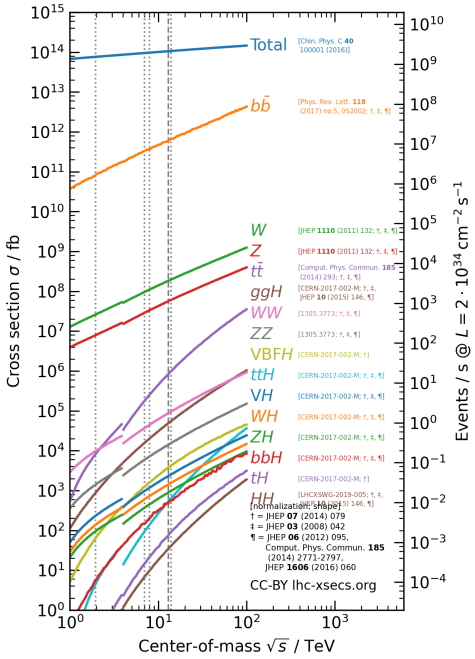

Figure 3.9: Cross-section of various physics processes at the Tevatron and the LHC [63]. The discontinuity in the cross-section at an energy of 4 GeV is due to the transition of proton - antiproton collisions to proton - proton collisions.

due to color confinement. These free quarks bind to form hadrons, which is referred to as hadronization [65]. We observe a cone of particles in the final state, as a result of hadronization. This stream of particles is termed a jet. Models simulating the production and decay of jets are included in the event generation.

3.4.3 Detector Simulation

The above information from event generation is fed into programs responsible for simulating an appropriate user-defined detector environment. Detector simulation encompasses information about the detector geometry and the interaction of particles in the detector medium. A well known toolkit, GEANT4 [66], is used to simulate the various layers of the ATLAS detector, namely the inner detector, calorimeters and the muon spectrometer. The trajectory of each particle is simulated in steps and their interactions with the detector media, such as Bremsstrahlung and Cherenkov radiation, are encoded in the simulation. Energy losses and scattering processes are well-modeled in GEANT4. The detector response to the simulated energy deposits and the subsequent readout are then simulated using a dedicated response simulation.

An important concept in studying simulations is truth-matching. Truth- matched events refer to events in simulated samples, in which the final state particles are matched to their parent particle at the simulation generator level.

Chapter 4

Object reconstruction and definition

In the aftermath of particle collisions, physics events of interest, also known as "signatures", are not directly observed in the detector. The presence of such signatures has to be inferred based on the reconstruction of the interactions of the particle of interest, such as electrons, muons and jets, with the sub-detector elements. Along with reconstructing a specific final state object, kinematic properties and detector interactions related to particle identification are considered. This chapter will focus on each final state object and its respective requirements, which are then used as input for the analysis.

4.1 Muons

Muon are reconstructed as tracks built from the segments in the inner detector and/or MS. This gives rise to two kinds of muon track definitions - Combined (CB) tracks and Muon

Extrapolated (ME) tracks. CB tracks take hit information from the ID and MS independently and perform a global refit to reconstruct a CB muon track [67]. Muon Extrapolated (ME) tracks use track information from the MS only. ME tracks significantly improve the muon acceptance within the $|\eta|$ range of $2.5 < |\eta| < 2.7$, where information from the inner detector is unavailable.

Muons are categorised into various identification (ID) selections, the ID used in this analysis is a *Medium* quality muon. *Medium* quality muons are required to have either a CB or ME track. CB tracks are required to have at least 3 hits in at least two MDT layers in the range of $|\eta| > 0.1$. For tracks with $|\eta| < 0.1$, at least 1 MDT layer hit and at most 1 MDT hole layer hit is allowed. ME tracks have to satisfy at least 3 hits in the MDT or CSC layers in the range of $2.5 < |\eta| < 2.7$ [67].

Muons candidates are also required to pass specific transverse and longitudinal impact parameter cuts. The impact parameter (IP) cuts aid in better rejection of muons coming from jets containing b-hadrons (b-jets), also known as non-prompt muons. This insures that most of the selected muons originate from the primary vertex (PV) of interaction and are isolated from other background activities in the detector.

The transverse impact parameter, d_0, refers to the distance of closest approach in the R-ϕ plane, of the particle track with respect to the PV. The cuts are imposed on the transverse impact parameter significance (d_0^{sig}), which is calculated as the transverse impact parameter divided by the uncertainty on its measurement, σ_{d_0}. z_0 is the longitudinal impact parameter,

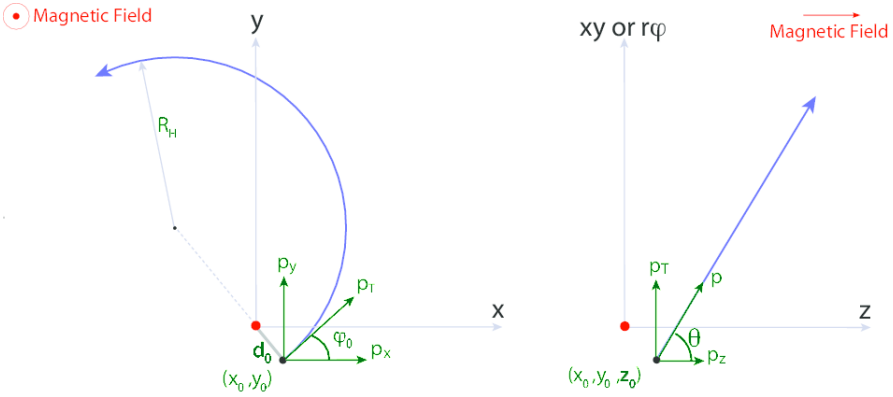

Figure 4.1: Left - Transverse impact parameter (d_0). Particle track is shown in blue, radius of the track is given by R_H, ϕ_0 is the azimuthal angle, and p_T is the transverse momentum. Right - Longitudinal impact parameter (z_0). θ is the polar angle. The red dot shows the primary vertex of interaction in both the figures [68].

which is defined as the distance between the particle track and the PV, along the z-axis. Figure 4.1 demonstrates a graphical representation of the above quantities.

In addition to ID requirements, muons are required to satisfy certain isolation criteria. Muons which originate from a hard scatter, such as from W, Z^0 or the Higgs boson, tend to be produced isolated from other particles. The isolation cuts improve the quality of the muon reconstruction, as well as suppresses background activity from other physics processes in the $R-\phi$ plane [67]. The specific isolation working point used here is `PFlowLoose_VarRad` [69].

In this analysis, we use two different selections of muons, for reasons detailed in Chapter 6 - *Loose* and *Tight* selection criteria. In both the selections, the muons are required to satisfy $|z_0 \sin\theta| < 0.5$mm. *Loose* muons do not require d_0^{sig}, and `PFlowLoose_VarRad` isolation cuts, whereas the *Tight* muons have to satisfy $|d_0^{\text{sig}}| < 3$ and `PFlowLoose_VarRad` isolation cuts,

as shown in table 4.1.

Along with the `PFlowLoose_VarRad` isolation working point, a novel isolation correction is applied, based on the kinematics of the muons from the a-boson in the targeted $t\bar{t}a$ signal. These muons are produced very close-by in the detector, meaning they have a low angular distance between them, $\Delta R < 0.2$, as seen in Figure 4.2. These close-by muons fail to meet the isolation requirements of `PFlowLoose_VarRad` working point and we observe a loss in signal events at low ΔR. The isolation correction acts on muons which have failed the required isolation working point. The algorithm searches for any additional *loose* muon within the isolation cone radius, and subtracts the p_T of the above track. After the subtraction, the isolation variables are re-calculated, to check whether the muon has passed the isolation threshold after the correction.

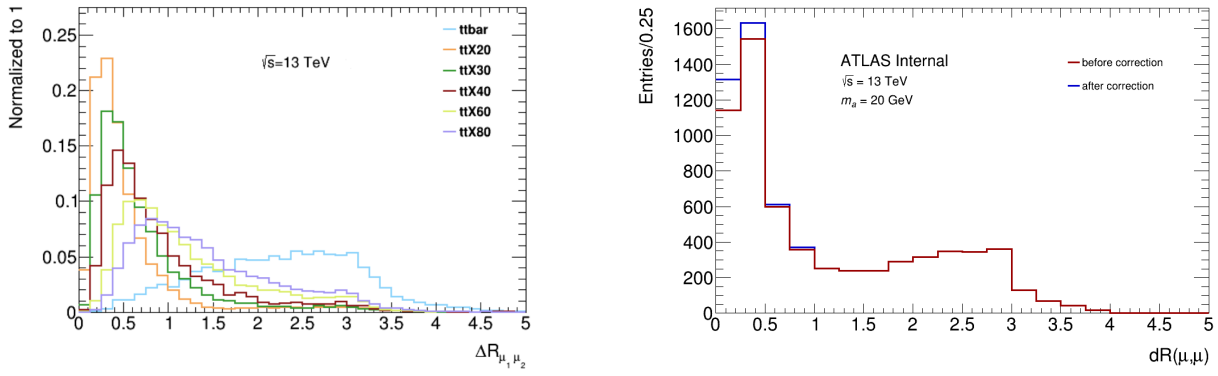

Figure 4.2: (Left) Separation between the two muons from the a-boson decay for a range of a-boson masses. One of the dominant backgrounds, the $t\bar{t}$ process, is also shown for comparison. (Right) Estimate of gain in signal yield for $m_a = 20$ GeV when using the isolation correction. A sizable increase in yield of signal events is seen at low ΔR.

Cut	*Loose* ID	*Tight* ID
ID	Medium	Medium
Acceptance	$\|\eta\| < 2.7$	$\|\eta\| < 2.7$
Isolation	-	`PFlowLoose_VarRad` + Isolation Correction
IP	-	$\|d_0^{\text{sig}}\| < 3$
	$\|z_0 \sin\theta\| < 0.5$ mm	$\|z_0 \sin\theta\| < 0.5$ mm

Table 4.1: Muon object definition.

4.2 Electrons

Reconstruction of electrons in the ATLAS detector uses information from the inner detector tracks to match the energy clusters deposited in the electromagnetic (EM) calorimeter. The EM calorimeter is divided into a 200 × 256 grid in η and ϕ. Each element in the grid has dimensions $\Delta\eta \times \Delta\phi = 0.025 \times 0.025$, which corresponds to the granularity of the second layer of the calorimeter. Specific calorimeter clustering algorithms are used to search for energy deposits above 2.5 GeV [70]. After the selection of clusters, these are further matched to the inner detector tracks, given the following requirement: $|\eta_{cluster} - \eta_{track}|$ <0.05 and -0.20 $< q \times [\Delta(\phi_{cluster}, \phi_{track})] < 0.05$. The asymmetry is due to the effects of Bremsstrahlung radiation of the electrons. Here, q refers to the charge of the electron ± 1. Following the matching of the tracks and clusters, the energy of the clusters is calibrated in detail, using several multivariate techniques, as discussed [71].

A likelihood-based algorithm is used for identifying electrons originating from hard-scatter decays, such as the $W^{\pm}$-boson and Z^0-boson, these electrons are also known as

prompt electrons. Several variables related to the shower shape of the energy cluster, and the tracking information are used as input to the likelihood. The specific electron ID used in the analysis is the `LHMedium` likelihood ID. A detailed discussion regarding the input variables and the calculation of the likelihood ratio can be found in [71]. Electrons in the $|\eta|$ region of $1.37 < |\eta| < 1.52$, also known as the "crack", are vetoed. This is because of the presence of inactive material between the barrel and the end-cap region of the EM calorimeter, which results in poor electron ID and energy resolution.

Additionally, electrons need to satisfy isolation criteria, for rejecting electrons arising from non hard-scatter decays. These electrons are mostly produced in the decay of heavy-flavour hadrons, and will be referred to as non-prompt electrons. In the context of this analysis, electrons have to satisfy requirements as dictated by the `PLVTight` working point [71], to suppress non-prompt electrons. Lastly, tracks for electron candidates have to pass the following IP cuts: $|d_0^{\text{sig}}| < 5$ and $|z_0 \sin\theta| < 0.5$ mm. A summary of electron object definition is presented in table 4.2.

Cut	Value/description
ID	`LHMedium`
Acceptance	$\|\eta\| < 2.47$
Isolation	`PLVTight`
IP	$\|z_0 \sin\theta\| < 0.5$ mm
	$\|d_0^{\text{sig}}\| < 5$

Table 4.2: Electron object definition.

4.3 Jets

Jets are produced as a result of hadronization of quarks and gluons in the detector. They leave tracks and energy deposits in the inner detector and the electromagnetic and hadronic calorimeters. The type of jets used as input to the analysis are known as `EMPflow` jets [72]. `EMPflow` jets are reconstructed using a particle flow algorithm, in which the information from both the inner detector and calorimeters, is utilized. An extensive discussion about the algorithm can be found in [73]. The geometrical acceptance of jets is in the range of $|\eta| < 2.5$.

Cut	Value/description
ID	`EMPflow`
Acceptance	$\|\eta\| < 2.5$
JVT	`Tight`
b-tagging	`DL1r`, $\epsilon_b = 70\%$

Table 4.3: Jets and b-jets object definitions.

Jets arising from non hard-scatter interactions, are referred to as *pileup* jets. These jets are treated as background for selecting jets which are a result of hard scatter interactions. Information from PVs and several track-based variables are used as input to a multivariate technique, known as the Jet-Vertex Tagger (JVT) [74]. Cuts are placed on this specific discriminant, to reduce *pileup* jets. The working point for JVT used in this analysis is `Tight`.

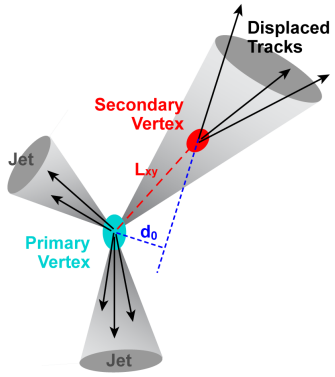

Figure 4.3: Production and reconstruction of b-jets. Primary and secondary vertices are shown, along with the p_T cones around the jets [75].

4.4 b-jets

A distinct class of jets, which is important with respect to this physics analysis, are b-jets. These jets arise from the production of b-quarks, and further hadronize to form b-hadrons. b-hadrons have a relatively longer lifetime, and travel approximately a fraction of a millimeter, before decaying further. Figure 4.3 shows the PV of the hard scatter, and the displaced vertex (secondary vertex) of the b-jet. A dedicated neural network based algorithm, know as `DL1r`, is used to identify the flavour of the parton originating from the jet [76]. In this search, b-jets have to satisfy the `DL1r` discriminant (ϵ_b) at 70% working point.

Beyond the above requirements, objects have to satisfy analysis-specific criteria, which will be discussed in the event selection section in chapter 6.

Chapter 5

Datasets

5.1 Data

The analysis is based on pp collision data collected by the ATLAS detector between 2015 and 2018, with a total integrated luminosity of 139 fb^{-1}, as shown in Figure 3.1. Data events suited for physics analyses have to satisfy the standard ATLAS data quality criteria. These events collectively form the so-called "Good Run Lists (GRLs)". An extensive list of the GRLs used in the analysis, is listed in table 5.1.

Year	Good Run List
2015	data15_13TeV.periodAllYear_DetStatus-v89-pro21-02_Unknown_PHYS_StandardGRL_All_Good_25ns.xml
2016	data16_13TeV.periodAllYear_DetStatus-v89-pro21-01_DQDefects-00-02-04_PHYS_StandardGRL_All_Good_25ns.xml
2017	data17_13TeV.periodAllYear_DetStatus-v99-pro22-01_Unknown_PHYS_StandardGRL_All_Good_25ns_Triggerno17e33prim.xml
2018	data18_13TeV.periodAllYear_DetStatus-v102-pro22-04_Unknown_PHYS_StandardGRL_All_Good_25ns_Triggerno17e33prim.xml

Table 5.1: Good Run Lists used for each year of data collection.

5.2 Signal Simulation

Signal events are generated using MadGraph5_aMC@NLO 2.7.3[77] MC generator at Next-to-Leading Order (NLO) precision, to study the expected signal behaviour. The simulated signal samples use the NNPDF 3.0 NLO [78] parton distribution function set. Pseudoscalar coupling is assumed between the a-boson and the top quarks. Scalar coupling is currently being considered in the next round of the analysis, and is beyond the scope of this timeline of this thesis. In case of a scalar coupling, the kinematic properties of the final state objects would be different from the pseudoscalar scenario. Three production mechanisms, namely, gluon-gluon fusion, quark-gluon fusion quark-quark initiated processes are included, as shown in Figure 5.1. `A14` tune is used to interface the events to Pythia[8.210] [79]. EvtGen 1.2.0 [80] program is used to simulate bottom and charm hadron decays. Geant4 [66, 81] is used for simulating the description of the ATLAS detector.

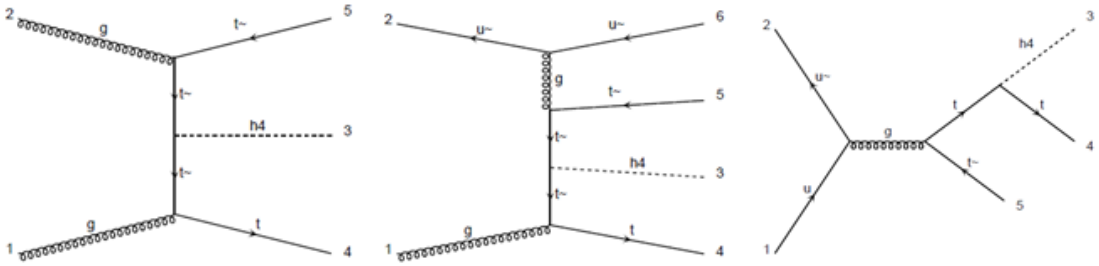

Figure 5.1: Feynman diagrams for the leading contributions to the $t\bar{t}a$, $a \to \mu\mu$ process for (left) gluon-gluon fusion, (center) quark-gluon fusion and (right) quark-quark initiated processes.

A total of 10 simulated mass points for the a-boson are generated, across the targeted mass range - 12, 16, 20, 25, 30, 40, 50, 60, 70 and 77 GeV. For each mass point of a, three distinct samples are generated, based on the $t\bar{t}$ decay mode:

- Semileptonic $t\bar{t}a$ decay mode : $t \to W^+(\to l^+\nu)\, b$, $\bar{t} \to W^-(\to q\bar{q})\, \bar{b}$, $a \to \mu\mu$
- Dileptonic $t\bar{t}a$ decay mode : $t \to W^+(\to l^+\nu)\, b$, $\bar{t} \to W^-(\to l^-\bar{\nu})\, \bar{b}$, $a \to \mu\mu$

Two samples are generated for the semileptonic $t\bar{t}$ decay mode, considering the permutation of $W^{\pm}$-boson decay. The total number of events per mass point of the a-boson, is 800,000 events. One sample is generated for dileptonic $t\bar{t}$ decay mode, since the $W^{\pm}$-boson decay is indistinguishable, totalling up to 200,000 events per mass point. Dihadronic cases are not considered in the scope of this analysis. Figure 5.2 shows key kinematic distributions at generator level.

5.3 Background simulation

Events from other Standard Model physics processes, which have similar final state signatures as the $t\bar{t}a$ signal, are collectively known as "background". These background processes are categorised into *irreducible* and *reducible* backgrounds. Simulated samples are used to describe these background processes, and estimate signal efficiency and acceptance. The following subsections describe the various simulations used in the analysis.

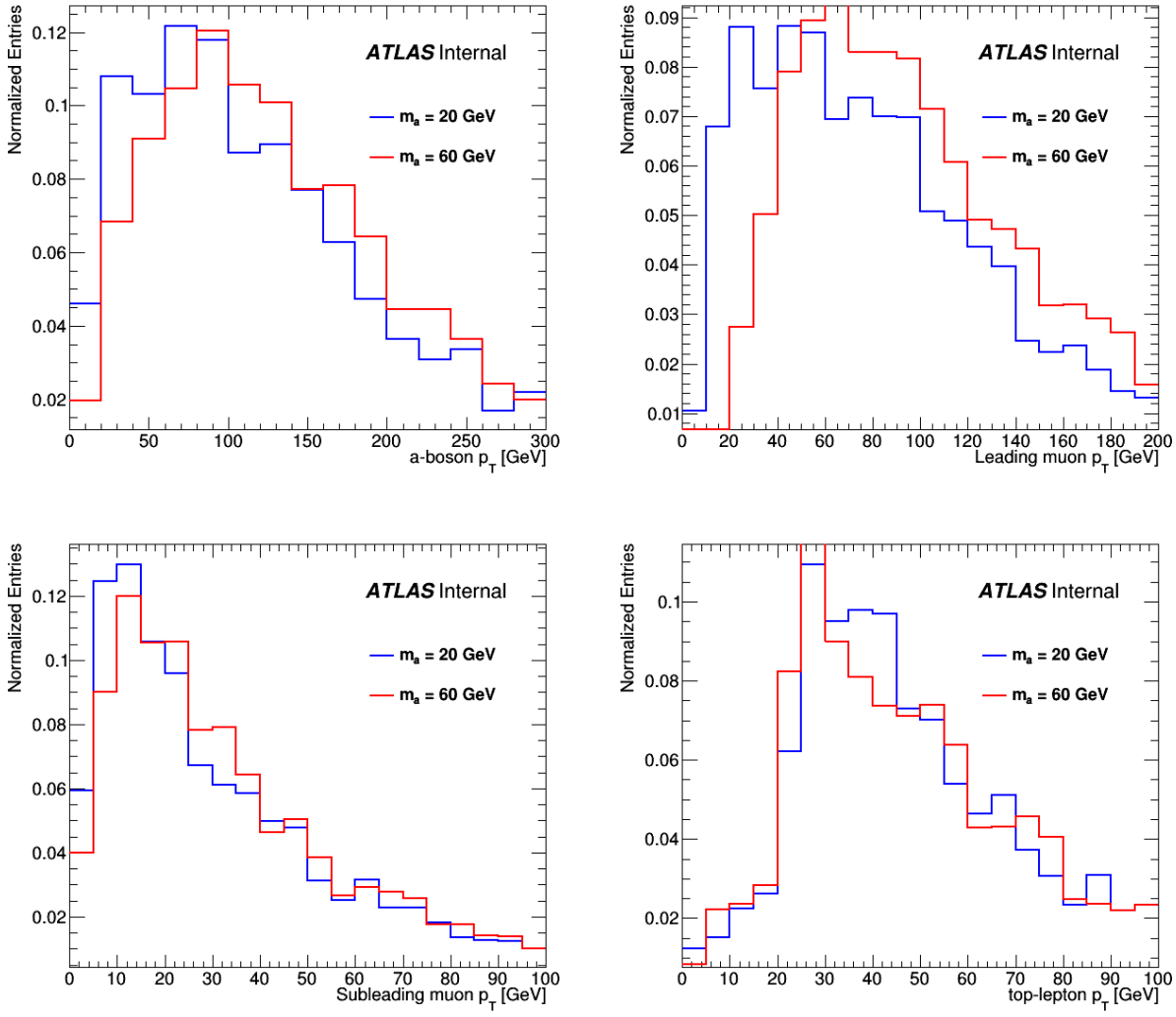

Figure 5.2: Distribution of key kinematic quantities used in this analysis at generator level. The a-boson p_T (top left), highest a-muon p_T (top right), second highest a-muon p_T (bottom left), and top-lepton p_T (bottom right).

5.3.1 Irreducible Background Samples

Leptons originating from hard scatter events (prompt leptons), mainly produced by decay of SM bosons, are indistinguishable with respect to the leptons originating from the $t\bar{t}a$ signal events. Hence, SM processes which produce three or more prompt leptons constitute the *irreducible* background processes. The dominant sources of this background arise from $t\bar{t}Z$, WZ, and the associated production of single top quarks with a Z^0-boson, tZ. Other rare processes, such as $t\bar{t}W$, $t\bar{t}H$, WWZ, WZZ, ZZZ and ZZ also contribute to the background.

MadGraph5_aMC@NLO 2.3.3 is used for generating $t\bar{t}Z$ events at NLO with NNPDF 3.0 NLO PDF. The events were interfaced to Pythia 8.210 using the A14 tune [82] and the NNPDF 2.3LO [83] PDF set. The decays of bottom and charm hadrons were simulated using the EvtGen 1.2.0 program. The WZ sample is modeled with Sherpa 2.2.1 [84]. Events were interfaced to Pythia 8.186 for the modeling of the parton shower, hadronization, and underlying event, with parameters set according to the AZNLO tune [85]. The EvtGen 1.2.0 program is used to decay bottom and charm hadrons.

The associated production of a single top quark with a Z^0-boson is simulated separately for the tZq and tWZ processes. Both processes were modeled using the MadGraph5_aMC@NLO 2.3.3 generator at NLO with the NNPDF 3.0nlo PDF. tZq (tWZ) events were interfaced with Pythia 8.230 (8.212) using the A14 tune and the Nnon-promptDF 2.3LO PDF set. The decays of bottom and charm hadrons were simulated using the EvtGen 1.2.0 program.

$t\bar{t}W$ is generated using MadGraph5_aMC@NLO and $t\bar{t}H$ is modeled by Powheg Box v2 [61]. WWZ, WZZ, ZZZ and ZZ processes are generated using Sherpa 2.2.2 [86].

5.3.2 Reducible Background Samples

Reducible backgrounds mainly consist of processes, where the leptons in the final state originate from hadronization of jets. These leptons are known as non-prompt leptons. Non-prompt muons are dominant in this background regime, and are directly estimated from data, as will be described in Section 7.3.2. Nevertheless, simulated samples, namely, $t\bar{t}$ is used to study the expected composition of non-prompt muons. Non-prompt electrons are sub-dominant and are estimated from $t\bar{t}$ and Z+jets MC samples. Additionally, conversion processes are taken into account by using $Z\gamma$ and $t\bar{t}\gamma$ samples. The leptons in conversion samples arise from the decay of the photon into a pair of electron and positron. $t\bar{t}$ events are simulated using Powheg Box v2 [87, 88, 89, 90] generator at NLO with the NNPDF 3.0nlo PDF set and the settings recommended in ATLAS [91]. The A14 tune is used to interface the events to Pythia 8.230. The decays of charm and bottom hadrons are performed by EvtGen 1.6.0.

The Sherpa 2.2.1 generator is used to model Z+jets MC samples. The production of $Z\gamma$ events is modeled using Sherpa 2.2.8. $t\bar{t}\gamma$ events are generated using MadGraph5_aMC@NLO 2.3.3 generator at Leading Order (LO). A complete list of MC samples for the background processes is shown in table 5.2.

Sample	Generator	Background	Events
$t\bar{t}Z$	MadGraph5_aMC@NLO 2.3.3	$t\bar{t}Z$	4925000
WZ	Sherpa 2.2.1	WZ	90799300
tZq	MadGraph5_aMC@NLO 2.3.3	tZ	13863261
tWZ	MadGraph5_aMC@NLO 2.3.3	tZ	380000
$t\bar{t}W$	MadGraph5_aMC@NLO	rare	20000000
$t\bar{t}H$	Powheg Box v2	rare	59370000
WWZ,WZZ, ZZZ	Sherpa 2.2.2	rare	1225000
ZZ	Sherpa 2.2.2	rare	79689700
Z+jets	Sherpa 2.2.1	non-prompt electrons	799088990
$t\bar{t}$	Powheg Box v2	non-prompt electrons	1263222000
$Z\gamma$	Sherpa 2.2.8	conversions	27439000
$t\bar{t}\gamma$	MadGraph5_aMC@NLO 2.3.3	conversions	7472015
$t\bar{t}a$	MadGraph5_aMC@NLO 2.7.3	signal	10000000

Table 5.2: Summary of background and signal MC samples used in the $e\mu\mu$ and $\mu\mu\mu$ analysis.

Chapter 6

Analysis Strategy

6.1 Overview

The goal of this analysis is to discover a novel $t\bar{t}a$ process, by measuring the branching fraction of the same. In case of no discovery, exclusion limits will be put on the branching fraction times the production cross-section of the process, using the Run 2 dataset. The observable used in this analysis is the dimuon mass spectrum of the two muon candidates from the a-boson, $m^a_{\mu\mu}$. The analysis targets a narrow dimuon invariant mass peak, where the width of the peak is dictated by the detector resolution, within the mass window of 12 - 77 GeV. The mass window is chosen as such to avoid the resonances from the Υ-meson at the lower edge and the Z^0-boson at higher edge of the mass range. A dimuon mass scan is performed within the above mass range, using steps smaller than the expected resolution.

Each mass hypothesis for the a-boson is tested, by using a binned fit for the signal and background events, in order to determine the signal significance at each mass hypothesis. The choice of binning in this mass region is detailed in Section 7.1. This analysis was partly developed in parallel with $H^+ \to aW, a \to \mu\mu$ analysis and may bear resemblance to it [92].

Signal candidates are expected to have a muon pair from the a-boson, along with decay products from the top quark pair. In the scope of this thesis, semileptonic decays of the top quark are considered, where the decay product of one of the top quarks contains a prompt electron or a muon, and the other top quark decays solely into quarks. This decay mode gives rise to two distinct three-lepton final state signatures, in terms of the flavour of the lepton from the top quark: one electron and a pair of muons ($e\mu\mu$) and three muons ($\mu\mu\mu$). The two relevant signal topologies are shown in Figure 6.1, and the two signal regions will be referred as $e\mu\mu$ and $\mu\mu\mu$ channels in the subsequent chapters. In case of the $e\mu\mu$ channel, the two muons are required to be oppositely charged, and in the $\mu\mu\mu$ channel, at least one oppositely charged pair of muons is required (refer sections 6.3, 6.4). Dileptonic decays of both the top-quarks are not considered in the analysis, due to a reduced branching fraction (25% of the semileptonic scenario), smaller acceptance and person power.

The next step in the analysis is to design a method for selecting signal-like events, which are candidates for the $t\bar{t}a$ process, and simultaneously reducing events from background physics processes. The analysis is performed in two separate decay channels, as mentioned above: $e\mu\mu$ and $\mu\mu\mu$ channels, with very similar selections applied, as described in the

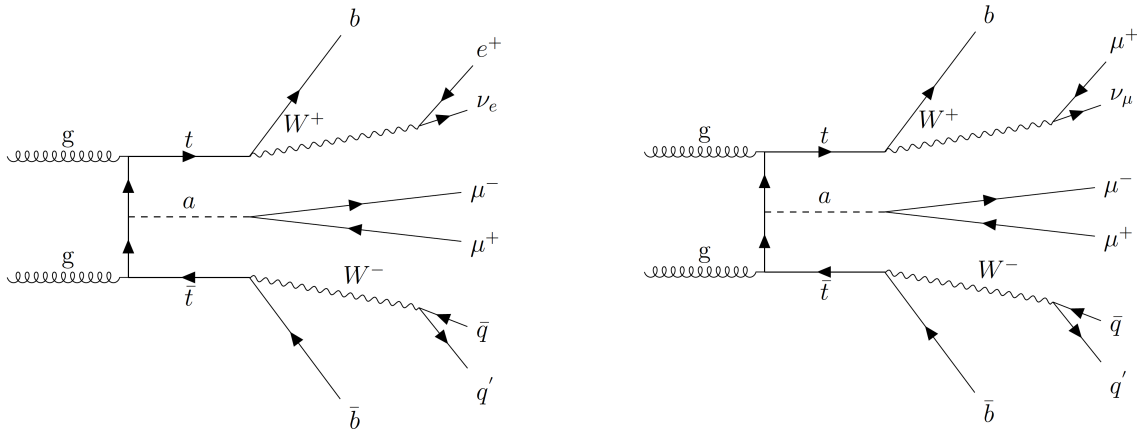

Figure 6.1: $t\bar{t}a$ signal topologies, showing semileptonic $t\bar{t}$ decay mode. Left - $e\mu\mu$ channel. Right - $\mu\mu\mu$ channel.

subsequent sections.

6.2 Trigger and preselection

As mentioned in Section 3.3.5, it is nearly impossible to store all recorded events from the collisions, hence ATLAS deploys various triggers to select standard final state objects, such as electrons, muons and jets. The event is selected only if it passes the required set of triggers in the analysis. In the context of this analysis, lepton triggers are implemented and discussed. Both data and simulated events have to pass the respective triggers for the analysis.

In both the channels, the lepton from the $W^{\pm}$-boson decay is usually the lepton with the highest transverse momentum, also known as the "leading lepton". The transverse momentum of the leading lepton is mostly independent of the a-boson mass. Hence,

selecting a $t\bar{t}a$ event based on this lepton is a good trigger strategy, as it minimises any possible trigger effects in the dimuon invariant mass spectrum for the a-boson.

In the $e\mu\mu$ channel, an event is selected if it has at least one electron, hence, the natural choice of the trigger is a "single electron trigger". Single electron triggers require at least one electron in the event, with transverse momentum, p_T, greater than 24 GeV or 26 GeV at the HLT. The p_T requirement depends on the specific data-taking periods. Other single electron triggers, requiring a higher p_T threshhold for the electron, are combined in a logical OR, in order to increase overall efficiency (refer table 6.1).

"Single muon triggers" are used to select events in the $\mu\mu\mu$ channel. This set of triggers is also combined in a logical OR, for increased efficiency, at both low and high muon p_T regimes. They require at least one muon with $p_T > 20$ GeV or $p_T > 26$ GeV depending on the specific year, and are combined with an "OR" condition with another trigger requiring muon $p_T > 50$ GeV, at the HLT. Table 6.1 lists the trigger names used in the analysis across different data-taking years.

Year	**Single Electron Triggers,** $e\mu\mu$	**Single Muon Triggers,** $\mu\mu\mu$
2015	HLT_e24_lhmedium_L1EM20VH HLT_e60_lhmedium HLT_e120_lhloose	HLT_mu20_iloose_L1MU15 HLT_mu50
2016-2018	HLT_e26_lhtight_nod0_ivarloose HLT_e60_lhmedium_nod0 HLT_e140_lhloose_nod0	mu26_ivarmedium HLT_mu50

Table 6.1: List of triggers used for each year of data collection, for the $e\mu\mu$ and $\mu\mu\mu$ channels

Events are required to have at least one reconstructed interaction vertex and to satisfy standard quality criteria. In a collision event, there are usually many interaction vertices due to pileup, and the vertex with the highest $\sum p_T^2$ is chosen to be "interesting", also known as the "primary vertex" of the physics interaction. Both channels, namely, $e\mu\mu$ and $\mu\mu\mu$, require at least three jets and at least one b-jet, satisfying $p_T > 20$ GeV. Jet and b-jet definitions can be referred in sections 4.3 and 4.4. Other selection criteria specific to each channel are described in the following sections.

6.3 $e\mu\mu$ event selection

The $e\mu\mu$ signal region requires exactly one *tight* electron, with p_T >27 GeV in an event. The p_T value mentioned above, refers to the "offline" p_T, after the calibration and reconstruction of the lepton in the event. This p_T threshold is chosen to be slightly higher than the trigger p_T threshold, to ensure that trigger effects, due to "online" reconstruction, do not contribute to additional systematic uncertainties. Beyond the electron object definition in Section 4.2, the electron has to be matched to the trigger object which was used in the single electron trigger decision. In addition to the electron requirement, two opposite-sign *tight* muons, passing the quality criterion mentioned in Section 4.1, are required. The leading muon has to satisfy p_T >15 GeV, and the sub-leading muon has to pass p_T >10 GeV. The dimuon mass of the opposite-sign pair, $m^a_{\mu\mu}$ has to be within 12 - 77 GeV.

Due to the application of the isolation correction to the muons candidates in the event,

the analysis is sensitive to cascade decays of hadrons producing multiple leptons. These leptons are non-prompt, and they pass the isolation correction requirements, leading to the contamination of the signal region with non-prompt leptons. In order to reject such processes, all lepton pairs (l_i, l_j) in the final state, have to satisfy an additional ΔR requirement : $\Delta R(l_i, l_j) > 0.1$, here i and j are the respective lepton indices.

6.4 $\mu\mu\mu$ event selection

In the $\mu\mu\mu$ signal region, exactly three *tight* muons are required, in which the sum of the charge of the muons is $\pm$ 1. The charge requirement placed on the three muons leads to exactly two opposite-sign muon pairs. Two dimuon mass hypothesis are possible in this scenario. The opposite-sign pair with mass closest to the m_a hypothesis is chosen as the pair from the decay of the a-boson, $m^a_{\mu\mu}$. These two muons, which are selected to form the pair, are known as "a muons". The third muon in the event is known as the "top-muon". The leading and sub-leading a muons are required to satisfy $p_T > 15$ GeV and $p_T > 10$ GeV respectively, and the top-muon must have $p_T > 27$ GeV. The top-muon is also required to match the trigger object, which was used in the single muon trigger. Beyond these requirements, muons have to pass the object definitions listed in Section 4.1. Additionally, $\Delta R(l_i, l_j) > 0.1$ is required of all the muon pairs, for reasons mentioned in the above section (in this case, l_i and l_j refer to the various combination of the leptons (muons)). The invariant mass of the two a-muons is required to satisfy $12 < m^a_{\mu\mu} < 77$ GeV. In order to reduce background from muon pairs

originating from the Z^0-boson, a veto is applied on the other opposite-sign dimuon pair, by requiring the mass to be outside the region $77 < m_{\mu\mu}^{other} < 107$ GeV. Table 6.2 summarizes the selection criteria for both the signal region channels in the analysis.

In this analysis, the signal region is blinded. This means that we do not look at data in the signal region, to avoid experimental biases in designing the event selection of signal-like candidates.

Region	Final State	Selection	Observable
Signal Region	$e\mu\mu$	1 tight electron 2 tight muons ≥ 3 jets, $\geq 1b$-jet $12 < m_{\mu\mu}^{a} < 77$ GeV	$m_{\mu\mu}^{a}$
	$\mu\mu\mu$	3 tight muons ≥ 3 jets, $\geq 1b$-jet $12 < m_{\mu\mu}^{a} < 77$ GeV ($m_{\mu\mu}^{other} \leq 77$ GeV or $m_{\mu\mu}^{other} > 107$ GeV)	$m_{\mu\mu}^{a}$

Table 6.2: Summary of signal region definitions used in the search for $t\bar{t}a$ events. All regions require an opposite-sign muon pair and trigger matching.

Chapter 7

Signal and Background Modeling

The next step in the analysis is to estimate the amount of SM background present in the two signal regions. Since we cannot look at data in the signal region, during the process of designing the event selection, backgrounds in the signal region are estimated based on interpolation and extrapolation of measured background yields in signal-free regions. These regions are known as control regions. Two control regions are used in this case, for estimating contributions from prompt and non-prompt leptons, respectively. Prompt lepton yields are estimated from simulations, and are compared with data events, whereas non-prompt lepton backgrounds are directly estimated from data in the control region and extrapolated to the signal region. An in-depth discussion about control region definitions will be presented in Section 7.3.

7.1 Binning of the dimuon mass spectrum

The primary observable in the analysis is the dimuon invariant mass, hence, it is essential to optimize the bin width of the mass distribution, based on dimuon mass resolution of the detector. This variable binning ensures that at every mass hypothesis for the a, we are able to extract a signal corresponding to the decay width of the a-boson, as accurately as possible.

The measured width of the dimuon mass peak is limited entirely by the detector resolution, which is known to a great extent, hence signal simulation is used to quantify the binning of the search region, within dimuon mass values of 12 - 77 GeV . $t\bar{t}a$ simulation is used to fit a double Crystal Ball (dCB) function to the dimuon mass, $m^a_{\mu\mu}$ [93], as shown in Figure 7.1. The dCB function is a combination of a Gaussian center and two power-law fits for fitting the two tails on either sides [93]. Further details about the parametrization of the signal model will be described in Section 7.2. The core dimuon mass resolution in the y-axis of Figure 7.2 is defined as the Gaussian width obtained from the dCB fit. As seen in the figure, the resolution grows as a linear function with the mass of the a-boson. A linear model is used to define the binning of the mass spectrum, such that 2σ of the signal events are almost entirely contained within a single bin, leading to 43 bins, listed in appendix A.

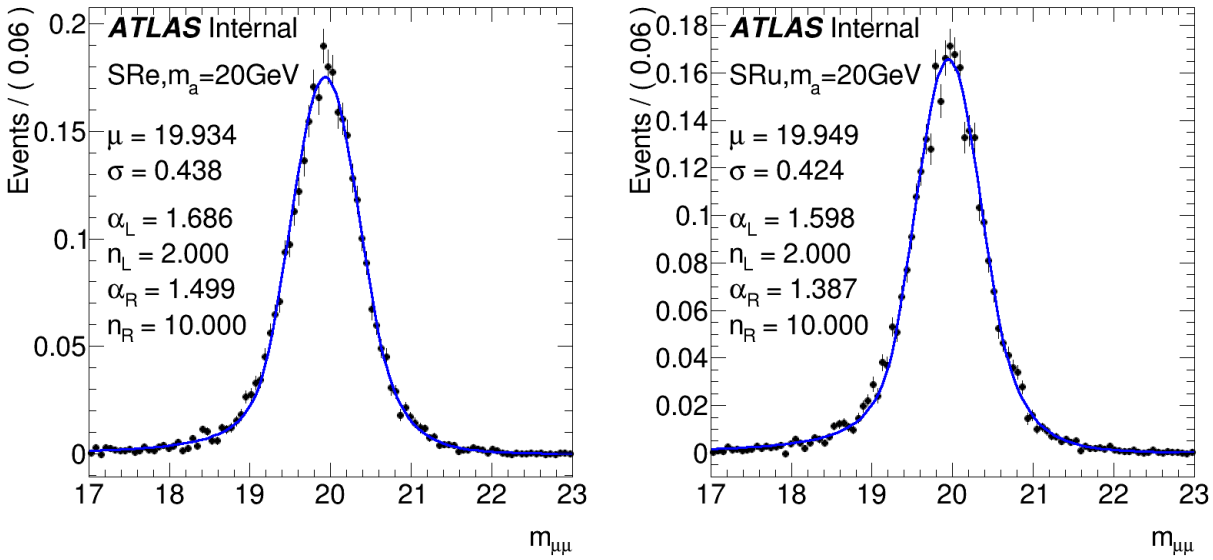

Figure 7.1: Signal fitting in $e\mu\mu$ (left) and $\mu\mu\mu$ (right) regions. A Double Crystal Ball fit is used for both the cases. Mean (μ) and sigma (σ) are obtained from the Gaussian part of the fit. α_L, n_L and α_R, n_R refer to the parameters of the left and right power-law functions.

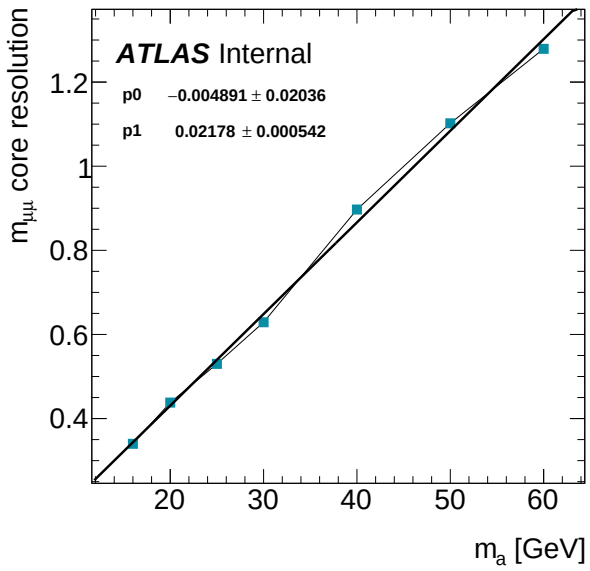

Figure 7.2: Dimuon mass resolution as a function of the a-boson mass.

7.2 Signal Modeling

In order to estimate signal yields at any arbitrary mass hypothesis of m_a, detailed knowledge about the behaviour of the signal has to be studied. The binning of the signal region is chosen such that the signal peak is contained in a couple of bins, as seen in Section 7.1. The parametrization of the signal is required to determine the test statistics for signal hypotheses between the masses generated in the MC signal samples, as discussed later in Chapter 9.

A double Crystal Ball (dCB) function [93] is used to model the signal shape seen in the MC signal samples, as seen in Figure 7.1. The shape and normalization of the signal distribution are parameterized separately. Normalized dimuon mass distributions from different simulated masses are fitted to a dCB density and then interpolated using the parameter morphing technique. Parameters from the dCB fit are analysed as a function of m_a. The values of α_L, α_R, n_L and n_R are found to be constant as a function of m_a and are set to 1.5, 1.4, 2.0 and 10.0 respectively, for both signal regions. Mean (μ) and sigma (σ) as a function of m_a is shown in Figure 7.3.

In order to validate the technique, one of the mass points for which the simulated sample is available, is removed from the inputs to the parameter morphing algorithm and the parameterized model is compared to the simulated sample. Figure 7.4 shows comparisons of the dCB-parameterized model to the m_a=20 GeV sample when this sample is removed from the parameter morphing. The deformations observed are within statistical uncertainties and are not significant, since the binning of signal regions is chosen such that

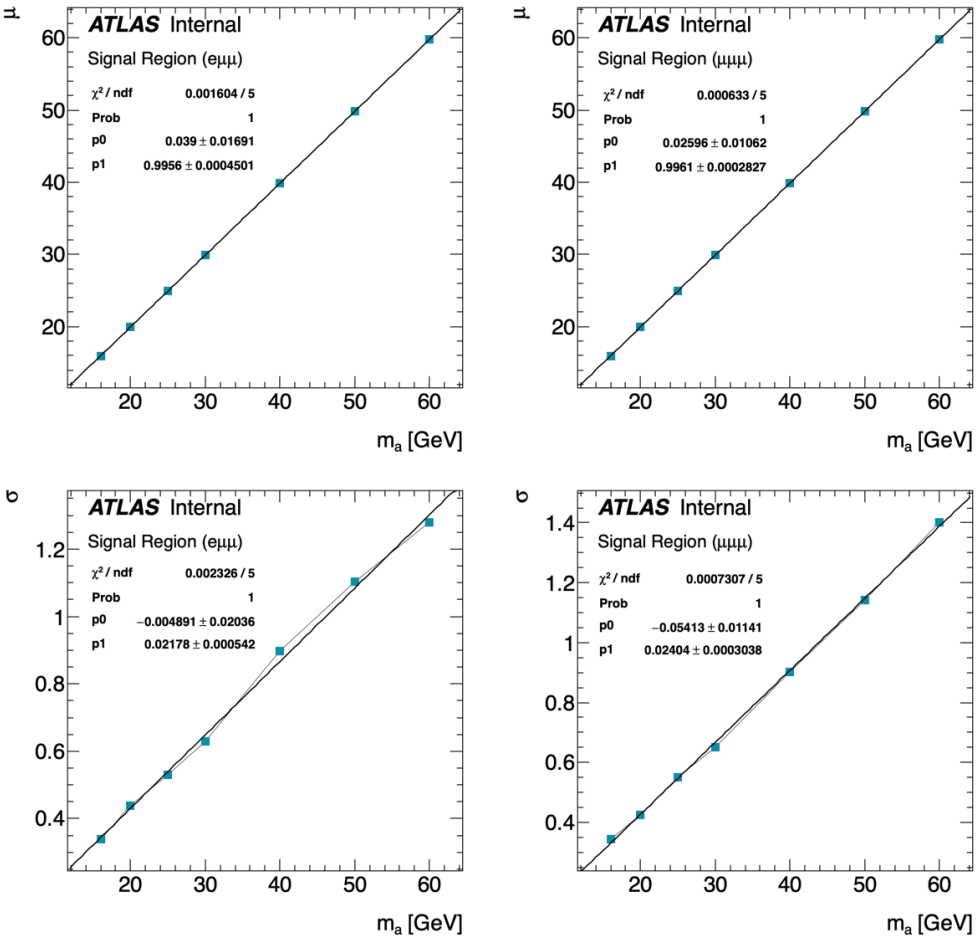

Figure 7.3: Mean, μ (top row) and σ (bottom row) from the dCB fits, as a function of m_a, for $e\mu\mu$ and $\mu\mu\mu$ signal regions. The values of α_L, α_R, n_L and n_R are set to 1.5, 1.4, 2.0 and 10.0 respectively, for both signal regions.

most of the signal is concentrated in one or atmost two bins. The normalization parametrization is obtained by fitting a linear function to the yield obtained from simulated signal samples. The total yields were found to be consistent with a linear fit as a function of m_a, in the $e\mu\mu$ and $\mu\mu\mu$ channels, as shown in Figure 7.5.

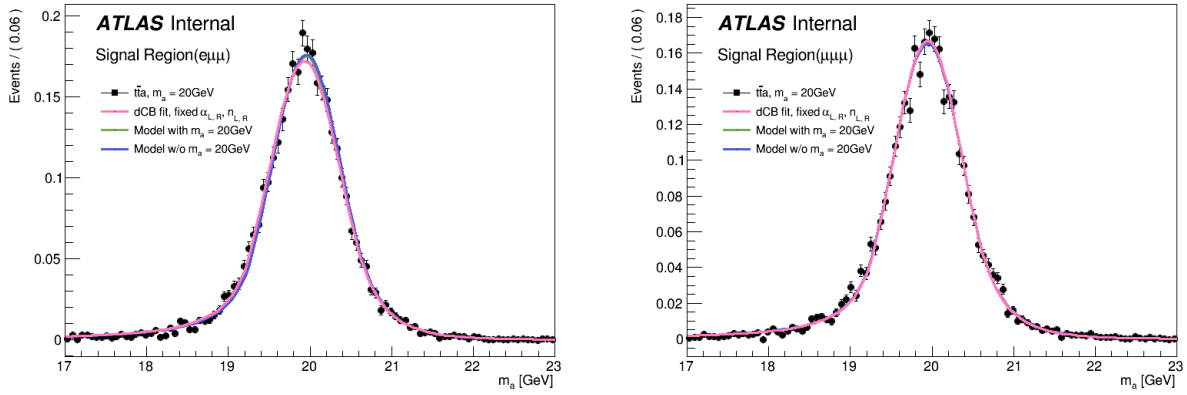

Figure 7.4: Validation of signal morphing for $t\bar{t}a$ sample, $m_a = 20$ GeV.

7.3 Background Modeling

7.3.1 Prompt Lepton background

Prompt lepton backgrounds arise from irreducible backgrounds as outlined in Section 5.3.1. The dominant source of background in this region comes from $t\bar{t}Z$ events, and from WZ processes. A specific control region, enriched in the above backgrounds, is designed to verify the modeling of the backgrounds and extract the value of its normalization factor from data. Since the majority of the events arise from the $t\bar{t}Z$ process, the muons forming the dimuon

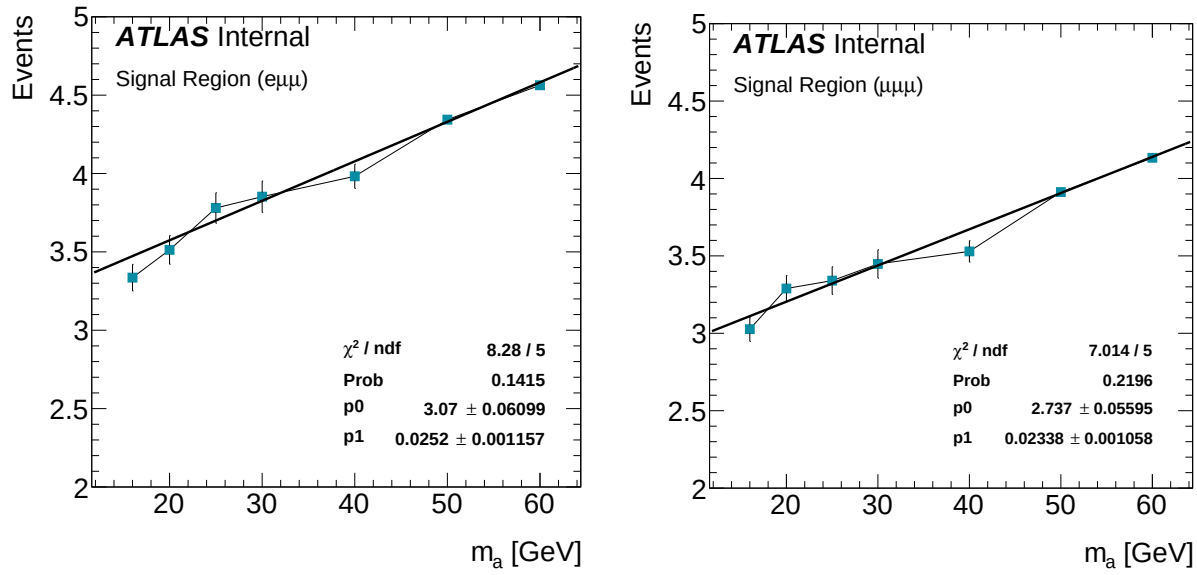

Figure 7.5: Signal yield parametrization in the $e\mu\mu$ (left) and $\mu\mu\mu$ (right) signal regions.

invariant mass are mostly from the on-shell Z^0-boson. Hence, this control region is known as the on-Z^0 control region. The control region is defined for both the $e\mu\mu$ and $\mu\mu\mu$ channels. In the $e\mu\mu$ channel, the control region is defined by requiring $77 < m^a_{\mu\mu}$ <107 GeV. Events in the $\mu\mu\mu$ channel, where either of the opposite-sign dimuon masses is within the 77 - 107 GeV dimuon mass window, is considered to be in the control region.

Apart from the dimuon mass window requirements, the control regions for both channels are selected in the exact same way as the signal region. Requiring the same multiplicity of jets and b-jets avoids additional uncertainties related to jet and heavy-flavor production in diboson and $t\bar{t}$ processes. Control regions are binned in number of jets and b-jets, to encompass contributions from different processes, including, WZ, $t\bar{t}Z$, and tZ. The binning used is as follows: the first bin contains events with exactly 1 b-jet and exactly 3 jets, the

second bin contains events with exactly 1 b-jet and $\geq$ 4 jets, and the final bin considers events with $\geq$ 2 b-jets and $\geq$ 4 jets. In all the above cases, b-jets are a subset of the total number of jets.

MC samples are used to model the prompt lepton backgrounds. A floating normalisation parameter is assigned to the dominant background, $t\bar{t}Z$. The normalization is constrained by the on-Z^0-boson control region. The prompt background yield in the signal region is determined by fitting the control region, and then using simulation to interpolate to the signal region. Details about the fitting procedure are presented in Chapter 9.

Figure 7.6 shows the distributions of the on-Z^0 control region for simulation and data in the $e\mu\mu$ and $\mu\mu\mu$ channels, binned in jets and b-jets. Figure 7.7 shows the data and expected background contribution, binned in dimuon mass. The binning is chosen to visualise the on-shell Z^0-boson mass. Good agreement is observed for data and simulation, which validates the background estimation technique in the control region.

7.3.2 Non Prompt Lepton background

The other source of background events are processes with non-prompt leptons, as mentioned in Section 5.3.2. These leptons originate from heavy quark decays, misidentification of hadrons as leptons and from photon conversions. $t\bar{t}$ and Z^0+jets processes are the major contributors in this scenario. These backgrounds are highly suppressed by the isolation and identification requirements placed on electrons and muons as described in chapters 4 and 6.

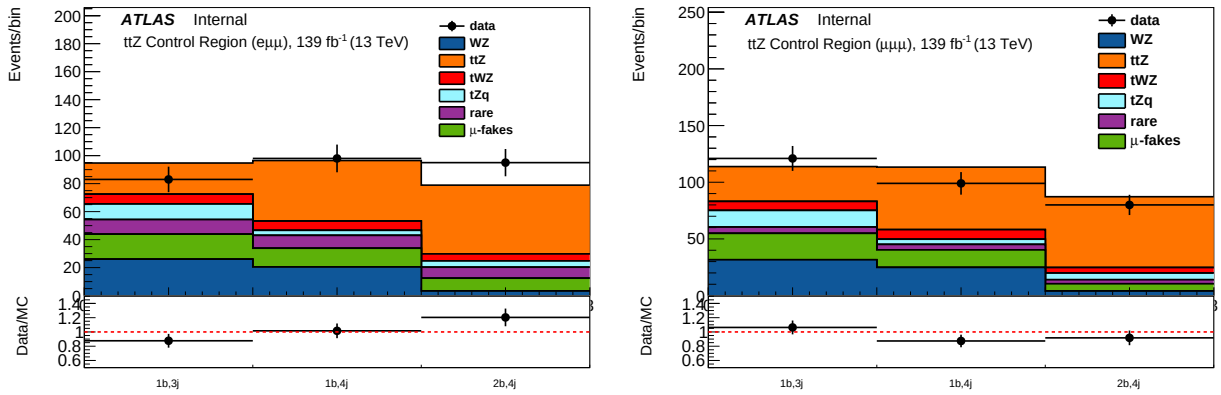

Figure 7.6: Comparison of data and expected background composition in the $e\mu\mu$ (left) and $\mu\mu\mu$ (right) on-Z^0-boson control region as a function of number of jets and b-jets.

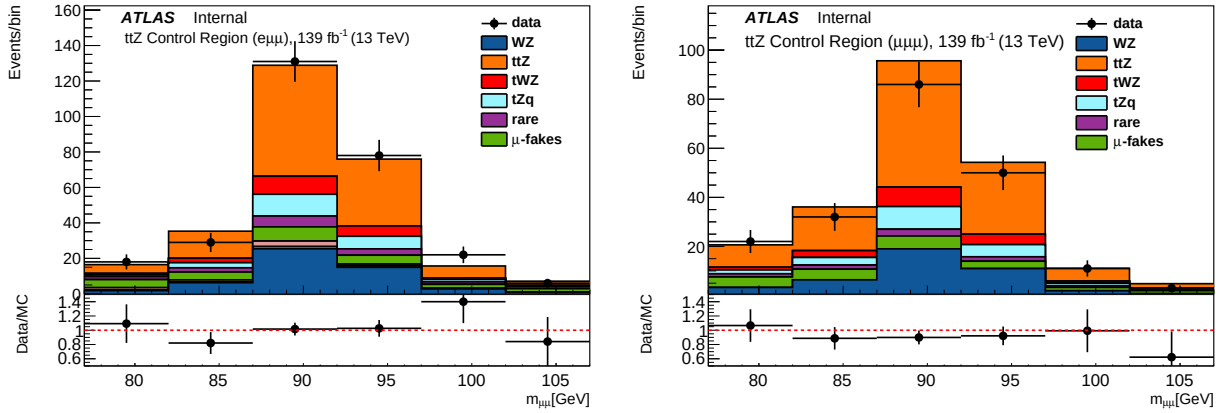

Figure 7.7: Comparison of data and expected background composition in the $e\mu\mu$ (left) and $\mu\mu\mu$ (right) on-Z^0-boson control region as a function of the dimuon mass corresponding to the a-boson.

In the $e\mu\mu$ signal region, non-prompt electron contribution is highly reduced by applying the PLVTight working point [71] for electron isolation. The Z^0+jets process is negligible in the $e\mu\mu$ signal region because the mass of two opposite-sign muons can only be within 12 - 77 GeV, which is below the Z^0-boson mass. In the $\mu\mu\mu$ channel, the contribution of Z^0+jets is suppressed by the Z^0-boson veto included in the event selection, as mentioned in Section 6.4.

In spite of the stringent selection cuts to reduce the background processes, non-prompt leptons enter significantly in the signal regions. An estimation of events, where the non-prompt lepton mimics a prompt lepton to enter the signal region, is necessary. These events are further classified depending on the flavour and multiplicity of the non-prompt leptons, and the physics processes involved, namely $t\bar{t}$ and Z^0+jets processes. Each muon in simulated events, used in the analysis, are truth-matched.

$t\bar{t}$ events are classified according to dileptonic and semileptonic decay modes of the top quarks. In the case of dileptonic $t\bar{t}$ events, two decay scenarios enter the non-prompt contribution in the two signal region final states. Both permutations of $W^{\pm}$-boson decays are included.

- Case 1: $t \to W^+(\to e^+\nu_e)\, b$, $\bar{t} \to W^-(\to \mu^-\bar{\nu_\mu})\, \bar{b}$
- Case 2: $t \to W^+(\to \mu^+\nu_\mu)\, b$, $\bar{t} \to W^-(\to \mu^-\bar{\nu_\mu})\, \bar{b}$

For case 1, in the $e\mu\mu$ signal region, one electron and one muon would come from the

top quarks, and the third muon has to be non-prompt. Similarly, in the $\mu\mu\mu$ signal region, one muon would come from the top decay and two muons would be considered non-prompt. In case 2, $e\mu\mu$ channel, two muons come from the top quarks and the electron has to be non-prompt. For the $\mu\mu\mu$ signal region, two muons originate from the top quarks and the other muon would be non-prompt.

In semileptonic top decays, two cases are possible as shown below. As mentioned previously, permutations of $W^{\pm}$-boson decays are considered.

- Case 3: $t \to W^{+}(\to e^{+}\nu_{e})\, b$, $\bar{t} \to W^{-}(\to q\bar{q})\, \bar{b}$
- Case 4: $t \to W^{+}(\to \mu^{+}\nu_{\mu})\, b$, $\bar{t} \to W^{-}(\to q\bar{q})\, \bar{b}$

In the $e\mu\mu$ signal region, for case 3, the electron will come from the top quark, and both the muons would be non-prompt, and in $\mu\mu\mu$ signal region, all three muons would be non-prompt. For case 4, one muon would come from the top decay and the electron and the other muon would be non-prompt, in the $e\mu\mu$ signal region. In the $\mu\mu\mu$ signal region, one muon would be prompt, and the other two muons would be non-prompt.

The other sub-dominant background in this regime arises from $Z(\to \mu\mu)$+jets processes. In this case, the electron will mostly be non-prompt, and the two muons will be prompt, coming from the decay of the Z^{0}-boson, in the $e\mu\mu$ signal region. For the $\mu\mu\mu$ signal region, two muons will originate from the Z^{0}, and one additional muons will be non-prompt.

Table 7.1 summarizes each of the physics processes and number of events with non-prompt leptons entering the signal regions. The majority of the non-prompt leptons

	$e\mu\mu$ signal region		$\mu\mu\mu$ signal region	
Process	MC yield	non-prompt leptons	MC yield	non-prompt leptons
$t \to W^+(\to e^+\nu_e)\, b$, $\bar{t} \to W^-(\to \mu^-\bar{\nu_\mu})\, \bar{b}$	23.0 ± 0.9	1μ	0.12 ± 0.07	2μ
$t \to W^+(\to \mu^+\nu_\mu)\, b$, $\bar{t} \to W^-(\to \mu^-\bar{\nu_\mu})\, \bar{b}$	4.9 ± 0.4	$1e$	8.6 ± 0.6	1μ
$t \to W^+(\to e^+\nu_e)\, b$, $\bar{t} \to W^-(\to q\bar{q})\, \bar{b}$	0 ± 0	2μ	0 ± 0	3μ
$t \to W^+(\to \mu^+\nu_\mu)\, b$, $\bar{t} \to W^-(\to q\bar{q})\, \bar{b}$	0 ± 0	$1e + 1\mu$	0.27 ± 0.20	2μ
$Z \to \mu^+\mu^- +$ jets	1.9 ± 0.3	$1e$	1.3 ± 0.3	1μ

Table 7.1: Expected number of events with non-prompt leptons from MC simulation of dominant processes. Numbers include the respective permutations for $W^{\pm}$-boson decays in $t\bar{t}$ decays. For the $\mu\mu\mu$ signal region, the numbers correspond to the $m_a = 30$ GeV hypothesis. Errors are statistical only.

arise from dileptonic decays of the top quarks, with non-prompt muons being the dominant contribution. In order to model the non-prompt muons precisely, we need to know the leading source of such muons. Figure 7.8 shows that most of the muons arise from heavy-flavour decays in $t\bar{t}$ and Z^0+jets processes. Events with double and triple non-prompt muons is negligible and such events are ignored in the analysis (refer table 7.1). Non-prompt electrons are directly estimated from simulation (non-prompt electrons in table 5.2), and a data-driven estimation is used to quantify the contribution from non-prompt muons.

A "tight-to-loose" data-driven method is used for measuring factors, known as "non-prompt factors" in a new control region, for estimating non-prompt muons in the signal regions. This control region is specifically enriched in non-prompt muons, and will be referred as the $t\bar{t}$ control region. The region is defined by requiring three leptons in the final state, where one of the leptons almost always comes from the hadronization of the b-jets. The

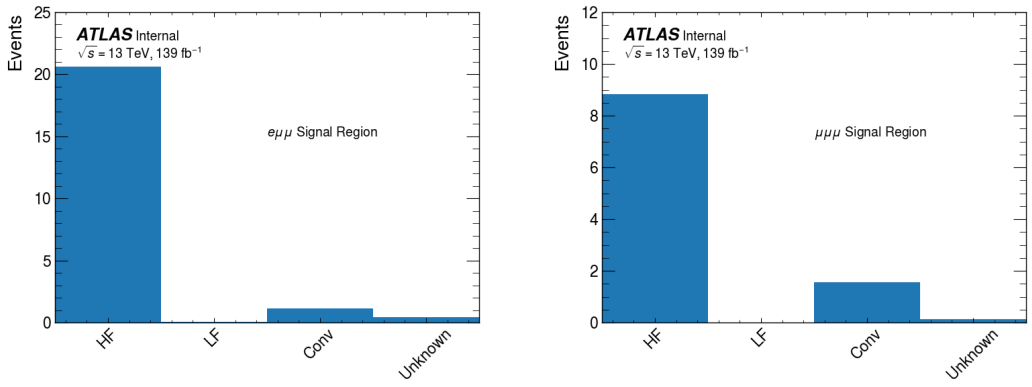

Figure 7.8: Expected composition of non-prompt muons in the $e\mu\mu$ (left) and $\mu\mu\mu$ (right) signal region. HF - Heavy Flavour, LF - Light Flavour, Conv - Conversions.

yield in the $t\bar{t}$ control region is proportional to the probability of a non-prompt muon to pass the *tight* selection criteria. The same probability can be applied to predict the non-prompt lepton background in the signal regions. *Tight* and *Loose* definitions are defined in Section 4.1.

The $t\bar{t}$ control region is designed by selecting events which pass the single electron trigger and have exactly one electron, with $p_T > 27$ GeV. The electron has to be matched to the object which fired the trigger. Exactly two opposite-sign muons are required, which have to satisfy $p_T > 15$ GeV, $p_T > 10$ GeV for the leading and the sub-leading muon, respectively. In order to be orthogonal to the signal regions and the on-Z^0 control region, a maximum of 2 jets and exactly 1 b-jet, is required. In order to prevent contamination from Z^0-boson + heavy flavour processes, a mass cut is placed on the two opposite-sign muons, $12 < m_{\mu\mu} < 77$ GeV.

Amongst the three leptons required in the $t\bar{t}$ control region, the muon with the same

electric charge as the electron is termed as the *non-prompt muon*, and the other muon is referred as the *prompt muon*. The region is defined in three bins, depending on the p_T of the *non-prompt muon*: $\alpha : 10 < p_T^{\mu_{non-prompt}} <$20 GeV, $\beta : 20 \leq p_T^{\mu_{non-prompt}} <$40 GeV and $\gamma : p_T^{\mu_{non-prompt}} \geq 40$ GeV.

The *non-prompt correction*, f_i is calculated in each of the three bins independently, using Equation 7.1, where $i \in \alpha, \beta, \gamma$, respectively. In the equation, "N_{Data}(*Tight non-prompt muon*)", refers to events in which the *non-prompt muon* passes *tight* criteria. Similarly, "N_{MC}(*Tight non-prompt muon*)" considers events where the *non-prompt muon* satisfies the *tight* criteria. "N_{Data}" and "N_{MC}" refer to total events in the data and simulation, respectively.

$$f_i = \frac{N_{Data}(Tight\, non-prompt\, muon) - N_{MC}(Tight\, non-prompt\, muon)}{N_{Data} - N_{MC}} \tag{7.1}$$

The *non-prompt factor*, F_i is calculated using f_i as shown in Equation 7.2.

$$F_i = \frac{f_i}{1 - f_i} \tag{7.2}$$

In order to apply the tight-to-loose method, every signal region and control region (refer tables 6.2, 7.2), is accompanied by its respective *isolation sidebands*. These sidebands have the exact same cuts as the signal regions and control regions, except the fact that one of the

muons fails the isolation or the $|d_{0\text{sig}}| < 3$ criterion. The fraction of events with more than one muon failing the *tight* criterion is negligible and these events are not considered (refer table 7.1).

Backgrounds with non-prompt muons are estimated from the data yields in the above isolation sidebands. This isolation sideband yield is multiplied by the *non-prompt factors* to estimate the non-prompt muon background in the signal regions. Each bin of the analysis (dimuon invariant mass bins in the signal region and bins in the on-Z^0 and $t\bar{t}$ control regions) has its corresponding isolation sideband, and the *non-prompt factors* only depend on the muon p_T (in three bins: $10 \leq p_T^{\mu} < 20$ GeV, $20 \leq p_T^{\mu} < 40$ GeV, and $p_T^{\mu} \geq 40$ GeV) and are common for the signal and control regions. The three *non-prompt factors* are constrained by the $t\bar{t}$ control region. A summary of the control regions used in estimating prompt and non-prompt lepton backgrounds in table 7.2.

7.3.3 Validation of $t\bar{t}$ control region

A validation of the tight-to-loose method is obtained by comparing the predicted number of events with non-prompt leptons with observed events, in a region with a selection identical to the signal region, but requiring two muons with same electric charge in the $e\mu\mu$ final state. Figure 7.9 shows this comparison, when using the methods described in Chapter 9. The binning used in the comparison is a merged version of the binning in the signal region because of the low number of events. Good agreement is observed between data and non-

Region	Final State	Selection	Observable
On-Z^0 Control Region	$e\mu\mu$	1 tight electron 2 tight muon ≥ 3 jets, $\geq 1b$-jet $77 < m^{a}_{\mu\mu} < 107$ GeV	$n_{b-\text{jets}}$, n_{jets}
	$\mu\mu\mu$	3 tight muons ≥ 3 jets, $\geq 1b$-jet ($77 < m^{a}_{\mu\mu} < 107$ GeV or $77 < m^{other}_{\mu\mu} < 107$ GeV)	$n_{b-\text{jets}}$, n_{jets}
$t\bar{t}$ Control Region	$e\mu\mu$	1 tight electron 2 tight muons < 3 jets, $1b$-jet $12 < m_{\mu\mu} < 77$ GeV	$p_T^{\mu_{non-prompt}}$

Table 7.2: Control regions used in background modeling for the analysis. All regions require an opposite-charge muon pair.

prompt background modeled by simulation, after the non-prompt correction is applied, which validates the tight-to-loose method.

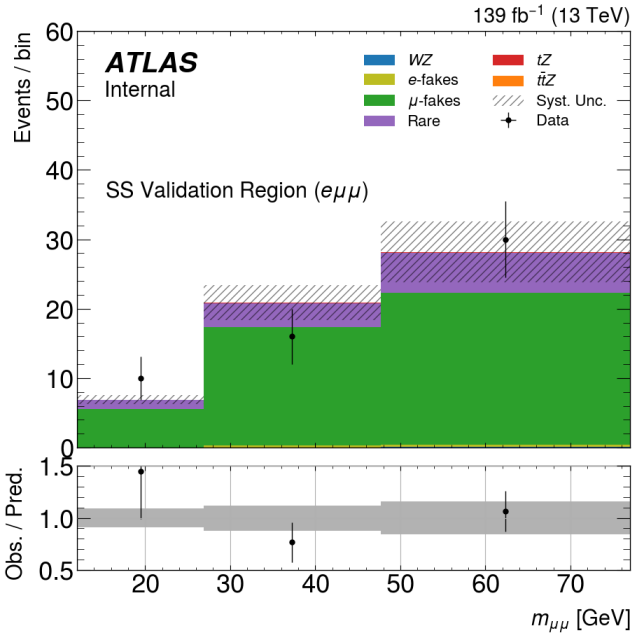

Figure 7.9: Comparison of the expected background with data in a region dominated by non-prompt background. SS- Same-sign for electric charge of the two muons.

Chapter 8

Uncertainties

Sources of uncertainties in the analysis are broadly classified into statistical and sytematic uncertainties. The following sections will describe each type of uncertainty in detail. Signal uncertainties are applied in a slightly different manner and will be described in Section 8.2.6. Implementation of the statistical and systematic uncertainties uses methods from HistFactory and is documented in [94], as well as in Section 9.0.2.

8.1 Statistical Uncertainties

Statistical uncertainties in this analysis arise from the data used from the detector, especially from the data yield in the two signal regions. It is described as the standard error of a Poisson distribution. The relevant errors arising from data in the signal region can be seen in Figure 10.1.

8.2 Systematic Uncertainties

This analysis is dominated by statistical uncertainty, due to the low number of expected events in the signal region, as will be seen in chapter 10. Figure 10.1 shows the statistical Poisson error on data to be compared with the grey shaded region arising from systematic uncertainties (from simulations), in the bottom section of the plot, for both the signal regions. It can be clearly seen that the statistical error is much larger than the systematic uncertainties. Nevertheless, systematic uncertainties have been considered to verify the fact that most of the variations in the systematic uncertainties are relatively small to substantially affect the result.

Systematic uncertainties arise from uncertainties in the calibration and acceptance of the detector (experimental uncertainties), from limitations in defining theoretical parameters (theoretical uncertainties) in simulations, and from the fact that simulations have finite number of events and carry an associated uncertainty with them. These uncertainties are studied using simulations, within the ATLAS collaboration, and are provided by the various ATLAS *Combined Performance* groups [95]. The uncertainties are evaluated by varying the relevant parameter to $\pm 1\sigma$ of its nominal value, set by the recommendations, and further evaluating the effects of these variations on the analysis. The following sections describe each type of systematic uncertainty used in the analysis. The choices made for the categories of systematic uncertainties follow recommendations from the *Combined Performance* groups, at the time of writing.

The error related to the limited number of events in the simulation is calculated per bin of the dimuon invariant mass distribution, based on the prescription defined by standard ROOT definition [96], which is set to the square root of weighted events in each bin.

8.2.1 Luminosity

The total uncertainty for the integrated luminosity measurement is computed by combining various uncertainties listed in [97]. The total uncertainty value is 1.7% for full Run 2 [97].

8.2.2 Jet and Missing Energy uncertainties

Systematic uncertainties affecting the reconstruction and identification of jets arise from energy calibration of the detector. Several simulated samples such as dijet, multijet Z^0+jets, and γ+jet are used in estimating the jet energy scale and resolution, and their respective uncertainties. Simulations are compared with data for calibration studies, an in-depth analysis can be found in [98]. The uncertainties related to the jet energy scale and jet energy resolution uncertainties are described by the JES STRONG REDUCTION scheme [99] and R4_SR_Scenario1_SimpleJER scheme [99], respectively (refer table 8.1). Uncertainties related to the identification of jets using the jet vertex tagger algorithm are considered as well [74]. These uncertainties are calculated by using Z^0+jets simulation to study the data and simulation comparison. Additional uncertainties related to b-jets and jets from charm hadrons are considered [100, 101]. Standard missing energy

uncertainties are used, as recommended by the collaboration [102].

Systematic Uncertainty Details	
JET_JER_EffectiveNP_1	Jet Energy Resolution
JET_JER_EffectiveNP_2	Jet Energy Resolution
JET_JER_EffectiveNP_3	Jet Energy Resolution
JET_JER_EffectiveNP_4	Jet Energy Resolution
JET_JER_EffectiveNP_5	Jet Energy Resolution
JET_JER_EffectiveNP_6	Jet Energy Resolution
JET_JER_EffectiveNP_7restTerm	Jet Energy Resolution
JET_EtaIntercalibration_NonClosure_highE	Jet η calibration
JET_EtaIntercalibration_NonClosure_negEta	Jet η calibration
JET_EtaIntercalibration_NonClosure_posEta	Jet η calibration
JET_GroupedNP_1	Jet Energy Scale
JET_GroupedNP_2	Jet Energy Scale
JET_GroupedNP_3	Jet Energy Scale
jvtWeight_JET_JvtEfficiency	Jet Vertex Tagger
JET_Flavor_Response	Flavour Physics
FT_EFF_B_systematics	Flavour Physics
FT_EFF_C_systematics	Flavour Physics
FT_EFF_Light_systematics	Flavour Physics
FT_EFF_extrapolation	Flavour Physics
FT_EFF_extrapolation_from_charm	Flavour Physics
MET_SoftTrk_Scale	Missing Energy Scale

Table 8.1: Jets and b-jets systematic uncertainties. Detailed explanation of each uncertainty can be found in [72] and [103].

8.2.3 Electron uncertainties

Uncertainties in the electron energy scale and resolution are calibrated using $Z \to e^+e^-$ simulations [104, 105]. Events from the simulation are compared to observed data, in terms of energy deposits in the electromagnetic calorimeter, electronics and material effects. The

differences in measurements is studied by considering the electron p_T and $|\eta|$ region. The systematic uncertainties are provided for electron reconstruction, identification, isolation and the relevant electron triggers. A SIMPLIFIED MODEL is used, as prescribed by the relevant *Combined Performance* group, and is listed in table 8.2.

Systematic Uncertainty	Details
EG_RESOLUTION_ALL	Resolution
EG_SCALE_AF2	Momentum scale variation
EG_SCALE_ALL	Momentum scale variation
EL_EFF_ID_TOTAL_1NPCOR_PLUS_UNCOR	Identification efficiency
EL_EFF_Iso_TOTAL_1NPCOR_PLUS_UNCOR	Isolation efficiency
EL_EFF_Reco_TOTAL_1NPCOR_PLUS_UNCOR	Reconstruction efficiency
EL_EFF_TriggerEff_TOTAL_1NPCOR_PLUS_UNCOR__1down	Trigger Efficiency
EL_EFF_TriggerEff_TOTAL_1NPCOR_PLUS_UNCOR__1up	Trigger Efficiency
EL_EFF_Trigger_TOTAL_1NPCOR_PLUS_UNCOR__1down	Trigger Efficiency
EL_EFF_Trigger_TOTAL_1NPCOR_PLUS_UNCOR__1up	Trigger Efficiency

Table 8.2: Electron systematic uncertainties. Detailed explanation of each uncertainty can be found in [106].

8.2.4 Muon uncertainties

Systematic uncertainties in the reconstruction, identification and trigger efficiency of muons are studied by using $Z \to \mu^+\mu^-$ and $J/\psi \to \mu^+\mu^-$ simulations [107]. Correction factors are calculated for a set of uncertainties listed in table 8.3, and are considered in the interpretation of the final result. These uncertainties are used based on the recommendation of the *Muon Combined Performance* group in the collaboration [108].

Systematic Uncertainty	Details
MUON_ID	ID track resolution
MUON_MS	MS track resolution
MUON_SAGITTA_RESBIAS	Momentum scale variation
MUON_SAGITTA_RHO	Momentum scale variation
MUON_SCALE	Momentum scale variation
MUON_EFF_BADMUON_SYS	Error on the bad muon veto efficiency
MUON_EFF_ISO_STAT	Isolation efficiency
MUON_EFF_ISO_SYS	Isolation efficiency
MUON_EFF_RECO_STAT	Reconstruction efficiency
MUON_EFF_RECO_SYS	Reconstruction efficiency
MUON_EFF_TTVA_STAT	Track-to-vertex association efficiency
MUON_EFF_TTVA_SYS	Track-to-vertex association efficiency
MUON_EFF_TrigStatUncertainty__1down	Trigger Efficiency
MUON_EFF_TrigStatUncertainty__1up	Trigger Efficiency
MUON_EFF_TrigSystUncertainty__1down	Trigger Efficiency
MUON_EFF_TrigSystUncertainty__1up	Trigger Efficiency

Table 8.3: Muon systematic uncertainties. Detailed explanation of each uncertainty can be found in [109].

8.2.5 Theoretical uncertainties

In this analysis, two sources of theoretical uncertainties are considered for tWZ $t\bar{t}Z$, WZ and $t\bar{t}a$ simulations. The first kind of uncertainty arises from the fact that the cross-section of a physics process is truncated at higher order perturbative terms. The uncertainty associated with the missing terms is estimated by varying the renormalization and factorization scales [110]. A 7-point uncertainty is recommended by the collaboration, where the renormalization (μ_R) and factorization (μ_F) scales are varied independently by a factor 0.5 and 2.0. A pair-wise variation of $\{\mu_R \times \mu_F\}$ is used as follows: {0.5,0.5}, {1,0.5}, {0.5,1}, {1,1}, {2,1} {1,2}, {2,2}. Further details about this method can be found in [111]. The highest and lowest difference with respect to the nominal yields is calculated by exploiting `LHE` weights [112]. The highest and lowest yields are referred to as the up and down scale variations, respectively, as shown in table 8.4. Another source of theoretical uncertainty arises from the choice of parton distribution function for parton showering in the simulation. A total of 100 values of parton distribution function uncertainties is considered for the simulation samples mentioned above.

Type	Systematic Uncertainty	Details
Scale up	`muR05muF05_260000`	Upper edge of 7-point uncertainty
Scale down	`muR20muF20_260000`	Lower edge of 7-point uncertainty
PDFs	`muR10muF10_260001 - 260100`	Parton distribution function variations

Table 8.4: Scale and parton distribution function systematic uncertainties

Implementation of the above systematic uncertainties in the analysis is detailed in chapter

9.

8.2.6 Uncertainties for Signal

Detailed studies of the impact of systematic uncertainties in the signal yields is carried out with $t\bar{t}a$ simulations for different values of m_a. As shown in Figure 8.1, no dependence is observed across the various hypotheses for m_a for various systematic uncertainties, in both the signal regions. The variation in yields is consistent with statistical fluctuations of the simulated samples. Hence, the values of systematic uncertainties for $m_a = 30$ GeV is considered as a reference for all of the signal hypotheses. Table 8.5 shows the maximum variation for each systematic uncertainty for $m_a = 30$ GeV in the $e\mu\mu$ and $\mu\mu\mu$ signal regions.

Table 8.5: Systematic uncertainties affecting $t\bar{t}a$ in the $e\mu\mu$ and $\mu\mu\mu$ signal regions (SRs). $m_a = 30$ GeV is used as a representative mass for the various mass hypotheses for m_a. NA refers to the systematic uncertainties having no effect on the nominal yield.

Systematic Uncertainty	**Uncertainty(%)**	
	$e\mu\mu$ SR	$\mu\mu\mu$ SR
EG_RESOLUTION_ALL	0.036	0.0013
EG_SCALE_AF2	0.026	0.00080
EG_SCALE_ALL	0.078	0.010
EL_EFF_ID_TOTAL_1NPCOR_PLUS_UNCOR	0.62	0.12

Continued on next page

Table 8.5 – Continued from previous page

Systematic Uncertainty	Uncertainty(%)	
	$e\mu\mu$ SR	$\mu\mu\mu$ SR
EL_EFF_Iso_TOTAL_1NPCOR_PLUS_UNCOR	0.19	0.026
EL_EFF_Reco_TOTAL_1NPCOR_PLUS_UNCOR	0.15	0.036
MUON_ID	0.075	0.076
MUON_MS	0.021	0.022
MUON_SAGITTA_RESBIAS	0.031	0.067
MUON_SAGITTA_RHO	NA	NA
MUON_SCALE	0.079	0.15
MUON_EFF_BADMUON_SYS	NA	NA
MUON_EFF_ISO_STAT	1.23	1.80
MUON_EFF_ISO_SYS	2.98	3.90
MUON_EFF_RECO_STAT	0.11	0.15
MUON_EFF_RECO_SYS	0.47	0.70
MUON_EFF_TTVA_STAT	0.10	0.14
MUON_EFF_TTVA_SYS	0.11	0.15
JET_EtaIntercalibration_NonClosure_highE	NA	NA
JET_EtaIntercalibration_NonClosure_negEta	0.0099	0.016

Continued on next page

Table 8.5 – Continued from previous page

Systematic Uncertainty	Uncertainty(%)	
	$e\mu\mu$ SR	$\mu\mu\mu$ SR
JET_EtaIntercalibration_NonClosure_posEta	0.011	0.011
JET_Flavor_Response	0.91	0.82
JET_GroupedNP_1	1.66	1.58
JET_GroupedNP_2	1.62	1.59
JET_GroupedNP_3	0.14	0.17
JET_JER_EffectiveNP_1	0.087	0.038
JET_JER_EffectiveNP_2	0.13	0.083
JET_JER_EffectiveNP_3	0.12	0.011
JET_JER_EffectiveNP_4	0.17	0.0422
JET_JER_EffectiveNP_5	0.068	0.0065
JET_JER_EffectiveNP_6	0.022	0.014
JET_JER_EffectiveNP_7restTerm	0.148	0.045
jvtWeight_JET_JvtEfficiency	0.28	0.27
FT_EFF_B_systematics	0.93	0.94
FT_EFF_C_systematics	0.083	0.067
FT_EFF_extrapolation	0.013	0.0022

Continued on next page

Table 8.5 – Continued from previous page

Systematic Uncertainty	Uncertainty(%)	
	$e\mu\mu$ SR	$\mu\mu\mu$ SR
FT_EFF_extrapolation_from_charm	0.011	0.015
FT_EFF_Light_systematics	0.081	0.042
MET_SoftTrk_Scale	NA	NA
pileupWeight	0.51	0.49
MUON_EFF_TrigStatUncertainty	2.00	2.00
MUON_EFF_TrigSystUncertainty	2.00	2.00
EL_EFF_TriggerEff_TOTAL_1NPCOR_PLUS_UNCOR	2.00	2.00
EL_EFF_Trigger_TOTAL_1NPCOR_PLUS_UNCOR	2.00	2.00
scale	0.5	0.6
PDF	0.3	0.3

As seen in the above table, MUON_EFF_ISO_SYS has the maximum deviation from the nominal yield in both the signal regions. This uncertainty is related to the isolation definition of the muons used in the analysis [109].

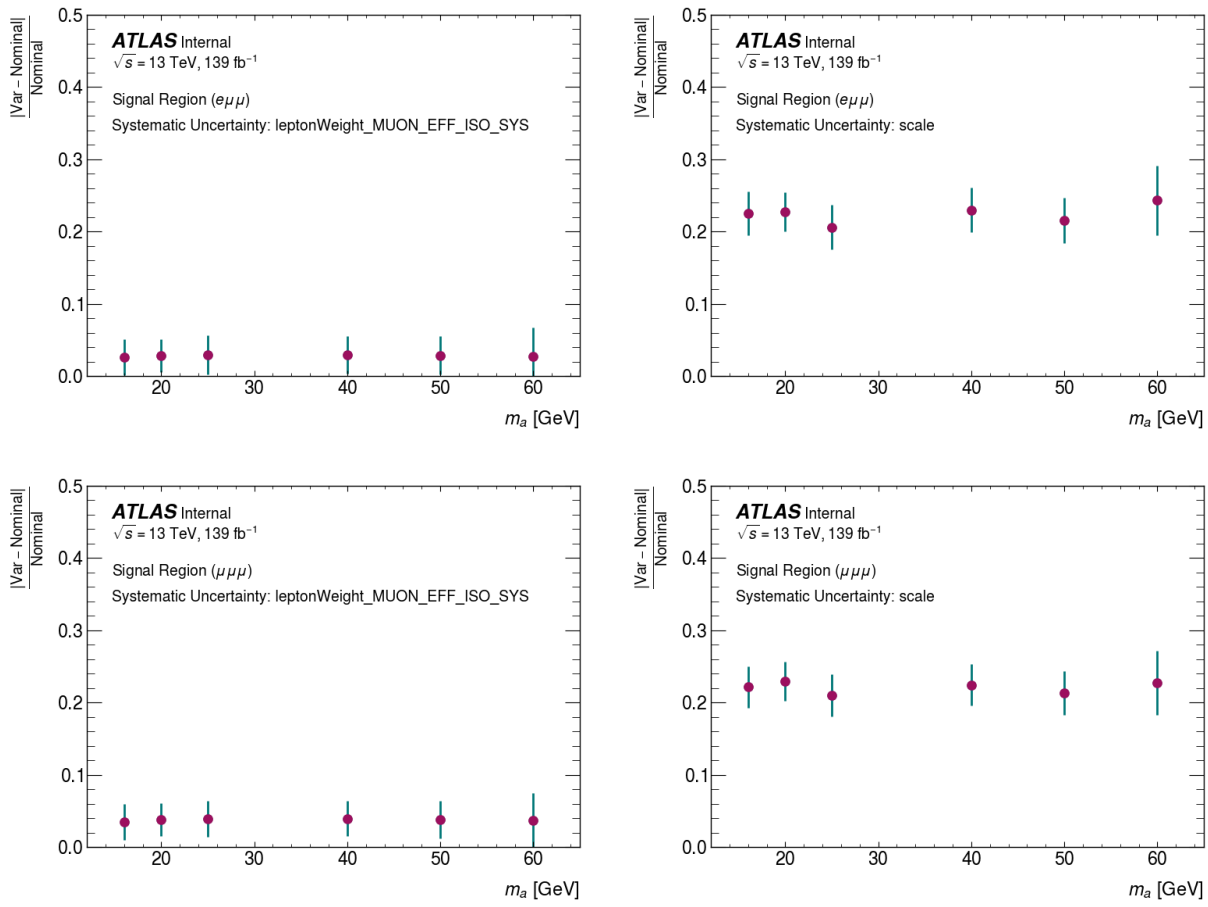

Figure 8.1: Systematic uncertainties in the $e\mu\mu$ (top row) and $\mu\mu\mu$ channels (bottom row) are shown for various m_a hypotheses.

Chapter 9

Statistical Framework

This chapter will present an overview of statistical methods used in the analysis. Statistical methods in experimental high-energy physics rely on comparing predicted parameters of a probabilistic model with the data collected by the detector. Frequentist statistics will be used in the analysis, where the probability is expressed as the frequency of the outcome of a repeatable experiment [12].

9.0.1 Method of Maximum likelihood

We start with the construction of a hypothesis, H, which is comprised of a number of parameters, $\vec{\theta}$, on which the outcome of the experiment, $\vec{x}$, is dependent. Here, the vectors represent a set of parameters and outcomes, respectively. The probability of the outcome of the experiment, given the hypothesis, H, can be written as $P(\vec{x}|\vec{\theta}, H)$. $P(\vec{x}|\vec{\theta}, H)$ can be

further expressed as the product of the individual probability distribution functions, $f(x_i|\vec{\theta})$ of the experiment, this product is known as the likelihood, $L(\vec{\theta})$ [12]. Note that in this scenario, the individual outcomes of the experiment, x_i are independent of each other.

$$L(\vec{\theta}) = \prod_{i=1}^{N} f\left(x_i \mid \vec{\theta}\right) \tag{9.1}$$

The above equation is valid only in the scenarios where N is fixed. If the probability to observe a total of N events, depends on the parameters, $\vec{\theta}$, the dependency has to be included in the likelihood function. If we consider N to follow a Poisson distribution, Equation 9.1 can be re-written as below, where n is mean of the distribution. Equation 9.2 is also known as the extended likelihood [12].

$$L(\vec{\theta}) = \frac{n^N}{N!} e^{-N} \prod_{i=1}^{N} f\left(x_i \mid \vec{\theta}\right) \tag{9.2}$$

After building an optimum likelihood function for the analysis, as will be described in Section 9.0.2, parameter estimation is carried out. For the purposes of this thesis, the maximum likelihood estimator (MLE) method is chosen. In this method, the "best" parameter is chosen, such that it maximises the likelihood function, for a given hypothesis.

9.0.2 Statistical Model for the analysis

As seen in chapters 6 and 7, the analysis has three specific regions (signal region, on-Z^0 control region, $t\bar{t}$ control region) and their corresponding binning, for each of the two channels, $e\mu\mu$ and $\mu\mu\mu$. The signal region is binned in dimuon mass in 43 bins, the on-Z^0 control region has three bins in the number of jets and b-jets, and the $t\bar{t}$ control region is binned in the three muon p_T bins. Each of the above-mentioned bins have an *isolation sideband* region associated with it, as detailed in Section 7.3.2. The next step is to build a likelihood model encapsulating the above information, to measure an exclusion limit for the signal significance or observe a signal, for a given number of observed events in data. The likelihood model for the analysis is based on the Poisson distribution, as it is a basic counting experiment, as shown in Equation 9.3. The likelihood is maximised for a given number of observed events in data, N_{data}, for values of the signal significance, μ, which is also known as the *parameter of interest*. The procedure is implemented using `Histfactory` family of statistical models [94, 113] and is based on the `pyhf` framework [114, 115].

$$
\begin{aligned}
L(\mu) = \prod_I [& \text{Pois}\left(N^I_{\text{data}} \mid \mu n^I_s + \mu_{t\bar{t}Z} n^I_{t\bar{t}Z} + F_\alpha n^{\alpha_I} + F_\beta n^{\beta_I} + F_\gamma n^{\gamma_I} + n^I_{\text{other}}\right) \\
& \times \text{Pois}\left(N^{\alpha_I}_{\text{data}} \mid \mu n^{\alpha_I}_s + \mu_{t\bar{t}Z} n^{\alpha_I}_{t\bar{t}Z} + n^{\alpha_I} + n^{\alpha_I}_{\text{other}}\right) \\
& \times \text{Pois}\left(N^{\beta_I}_{\text{data}} \mid \mu n^{\beta_I}_s + \mu_{t\bar{t}Z} n^{\beta_I}_{t\bar{t}Z} + n^{\beta_I} + n^{\beta_I}_{\text{other}}\right) \\
& \times \text{Pois}\left(N^{\gamma_I}_{\text{data}} \mid \mu n^{\gamma_I}_s + \mu_{t\bar{t}Z} n^{\gamma_I}_{t\bar{t}Z} + n^{\gamma_I} + n^{\gamma_I}_{\text{other}}\right)]
\end{aligned}
\tag{9.3}
$$

In Equation 9.3, the various Poisson distributions are multiplied for each bin, I, since the regions in the analysis are independent of each other. Here, I refers to the total number of bins in the two signal regions, the on-Z^0 control regions and the *tight* $t\bar{t}$ control region.

The first line represents the observed number of events in data, N_{data} and the summation of the total signal and background events in the signal and control regions. μn_s refers to the signal significance, μ is multiplied by the number of expected events in the signal region, n_s. The next term corresponds to the free-floating parameter, $\mu_{t\bar{t}Z}$, which is derived from events observed in data. This parameter is multiplied by the expected number of $t\bar{t}Z$ events from the $t\bar{t}Z$ simulation, which is the dominant prompt lepton background in the analysis (refer 7.3.1). As mentioned previously, the on-Z^0 control region is designed to constrain the $\mu_{t\bar{t}Z}$ parameter in the statistical fit. The next three terms refer to the *non-prompt factors*, F_i, where $i \in (\alpha, \beta, \gamma)$, and follow the same p_T criteria as mentioned in Section 7.3.2. In a specific bin in the signal region, we can have background contribution from any of the three p_T regions for the non-prompt muons, hence it is a summation of background events in the three p_T bins of the non-prompt muon. n^{α}, n^{β} , n^{γ} refer to the non-prompt lepton background events in the corresponding three bins. The last term n_{other} refers to the remaining sub-dominant prompt lepton background contributions.

As we know, each bin in the analysis is associated with a corresponding *isolation sideband*, which is not directly estimated from simulations, and depends on the p_T of the muon, which fails the isolation or the d_0^{sig} criteria. These regions are written as a product of Poisson

distribution in the last three lines of Equation 9.3. Here, N^{α}_{data} refers to the observed number of data events in the isolation sideband, corresponding to the $10 < p_T < 20$ GeV of the muon which failed either the isolation or the d_0^{sig} criterion. Similarly, N^{β}_{data} and N^{γ}_{data} denote the following muon p_T ranges, respectively: $20 < p_T < 40$ GeV and $p_T > 40$ GeV. The terms n^{α}_{s}, $n^{\alpha}_{t\bar{t}Z}$ and $n^{\alpha}_{\text{other}}$ refer to the contributions from the signal, $t\bar{t}Z$ and sub-dominant simulations, in this specific *isolation sideband*. The same notation is followed for the other two muon p_T ranges, denoted by β and γ.

Statistical and systematic uncertainties are added as constraint terms to Equation 9.3. These uncertainties are also known as nuisance parameters. The complete likelihood can be written in a slightly different manner, in order to include these extra parameters, as shown in Equation 9.4. Here, S and B refer to signal and background events, respectively. $\boldsymbol{a}$ denotes nuisance parameters related to experimental and theoretical systematic uncertainties (Section 8.2), $\boldsymbol{b}$ refers to statistical uncertainties (Section 8.1). $\boldsymbol{c}$ refer to the free floating parameters related to the normalisation of the background composition. In this analysis, $\mu_{t\bar{t}Z}$ and F_i, $(i \in \alpha, \beta, \gamma)$ are the four free-floating parameters used to contrain the prompt and non-prompt lepton backgrounds (sections 7.3.1, 7.3.2).

$$L_{\text{Pois}}(\mu, \boldsymbol{a}, \boldsymbol{b}, \boldsymbol{c}) = \prod_{i \in n_{bin}} P\left(n_i \mid \mu S_i(\boldsymbol{a}) + B_i(\boldsymbol{a}, \boldsymbol{b}, \boldsymbol{c})\right) \tag{9.4}$$

In order to estimate systematic uncertainties, the likelihood is multiplied by a constraint term as shown in Equation 9.5. These constraints are modeled as a Gaussian term, with mean

value of 0 and variance value is set to 1 [116]. It is useful to note that some uncertainties, such as the electron, muon, jet and b-jet uncertainties are correlated, which means that it affects the signal and the background simultaneously. Other systematic uncertainties, such as the theoretical uncertainties are specific to each simulated sample, as they are dependent on the sample generation process.

$$L_{\text{constrain}}\left(\boldsymbol{a}\right) = \prod_{i=1}^{n} G\left(a_i \mid 0, 1\right) = \prod_{i=1}^{n} \frac{1}{\sqrt{2\pi}} e^{-\frac{a_i^2}{2}} \tag{9.5}$$

The statistical uncertainties denoted by $\boldsymbol{b}$, are calculated for each bin of the analysis, and are included as a constraint term along with the systematic uncertainties. The modeling of statistical uncertainties follows a simplified recipe given by Beeston and Barlow [117, 94], wherein we consider one nuisance parameter per bin, which is associated with the total uncertainty on the total estimate from the simulation and the total statistical uncertainty, per region of the analysis. A Poisson distribution, $P(d_i|b_i d_i)$, is used to include these uncertainties, where d_i refers to the number of events in any given bin. A complete discussion on the involved nature of such errors and its simplification can be found in [94, 117, 116]. For the remaining discussions regarding both systematic and statistical uncertainties, and free floating parameters, $\boldsymbol{\theta}$ will be used to represent the complete set of nuisance parameters. Hence, the likelihood is now written as $L(\mu, \boldsymbol{\theta})$. The best fit value for $\mu, (\hat{\mu})$, and $\boldsymbol{\theta}, (\hat{\boldsymbol{\theta}})$, is obtained by using the maximum likelihood method as described in Section 9.0.1. More often, instead of maximising the likelihood function, the

value for the negative log-likelihood is minimized, to find the best fit parameter, as shown in Equation 9.6.

$$-\frac{\partial \ln(L(\mu,\boldsymbol{\theta})}{\partial \theta_j} = 0, \text{ and } \quad -\frac{\partial \ln(L(\mu,\boldsymbol{\theta})}{\partial \mu} = 0 \tag{9.6}$$

Next, we need to construct a variable from data, which can be used to test various hypotheses relevant to the analysis, and quantify its level of agreement with the observed data. This variable is often known as a *test statistic*, $\tilde{q}(\mu)$, and is defined using a *profile likelihood ratio* [12, 116], as shown in Equation 9.7.

$$\tilde{t}(\mu) = \begin{cases} \frac{L(\mu,\hat{\hat{\boldsymbol{\theta}}}(\mu))}{L(\hat{\mu},\hat{\boldsymbol{\theta}})} & \hat{\mu} \geq 0 \\ \frac{L(\mu,\hat{\hat{\boldsymbol{\theta}}}(\mu))}{L(0,\hat{\hat{\boldsymbol{\theta}}}(0))} & \hat{\mu} < 0 \end{cases} \tag{9.7}$$

In the above equation, $\hat{\mu}, \hat{\theta}$ maximise the value of L in the given domain $\mu \in [0, \infty)$, and $\hat{\hat{\theta}}$ maximises L for a fixed μ value. Since we are interested in knowing the significance of a discovery, in which the value of μ would be non-zero, the values of $\tilde{q}(\mu)$ can be written in the following manner [116].

$$\tilde{q}_\mu = \begin{cases} -2\ln\tilde{t}(\mu) & \hat{\mu} > 0 \\ 0 & \hat{\mu} \leq 0 \end{cases} \tag{9.8}$$

This test-statistic is used to perform a confidence limit hypothesis test using asymptotic theorems [118, 119] and MC toys, detailed in Chapter 10.

Chapter 10

Results

10.1 Maximum Likelihood Fit Results

The different regions in the analysis are described by the likelihood function, as we have already seen in the previous chapter. The negative log-likelihood is minimized for the best fit values of μ and $\boldsymbol{\theta}$, using `MINUIT` [120]. As reasoned in Section 7, the data in the signal regions is not accessible to us, meaning that the analysis is blinded, whereas the data is not blinded in the two control regions. The validation of the fit and the expected exclusion limits of the search are studied in blinded signal regions for the $e\mu\mu$ and $\mu\mu\mu$ channels. The fit is carried out using the procedure in Section 9.0.2.

In order to carry out several pseudo-experiments, we need to construct an artificial dataset, referred to as the Asimov dataset [113]. The dataset is constructed in such a way

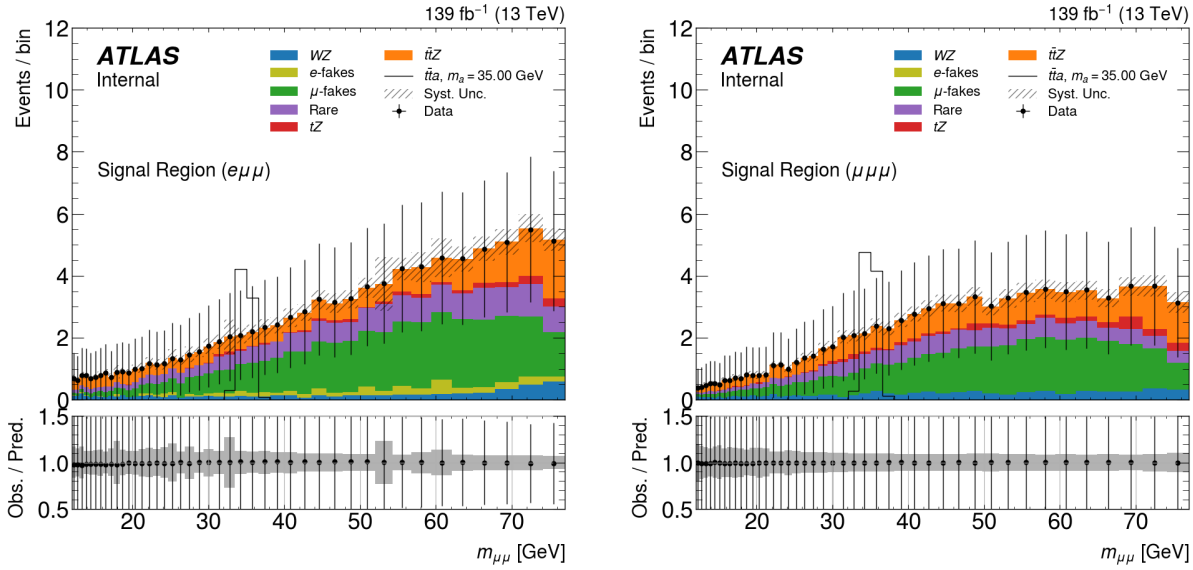

Figure 10.1: Predicted background and signal distributions for the (left) $e\mu\mu$ and (right) $\mu\mu\mu$ channels. The data points refer to the sum of the backgrounds.

that we obtain the true parameter values when we evaluate the estimators for all the given parameters. In the context of this search, the initial values of the free-floating parameters, $\mu_{t\bar{t}Z}$, F_α, F_β and F_γ are used to estimate the (pseudo) data in the signal regions, and collider data is used for the on-Z^0 and $t\bar{t}$ control regions. This dataset is used to determine an expected exclusion limit on the cross-section and branching fraction of the $t\bar{t}a$ process and $a \to \mu\mu$, respectively, which will be written as $\sigma(t\bar{t}a)\mathrm{Br}(a \to \mu\mu)$ in the succeeding sections.

Using the above Asimov dataset, the results from the fit are obtained for a background-only hypothesis, for the two signal regions, as shown in Figure 10.1. The error bins represent statistical errors only (Poisson errors). The dimuon invariant mass peak from the expected

signal, $t\bar{t}a$, is shown for $m_a = 35$ GeV, assuming $\sigma(t\bar{t}a)\text{Br}(a \to \mu\mu) = 2$ fb, along with the prompt and non-prompt lepton backgrounds. Along with fitting a background-only hypothesis as shown above, maximum likelihood fits are performed for signal and background hypotheses, for a total of 43 masses for the a-boson. The number of mass points are motivated from the binning in the dimuon mass spectrum, as detailed in Section 7.1.

The on-Z^0 control regions are shown in Figure 10.2, after the fit is performed. It is seen that collider data and the estimated background events from simulation are in agreement, within uncertainties.

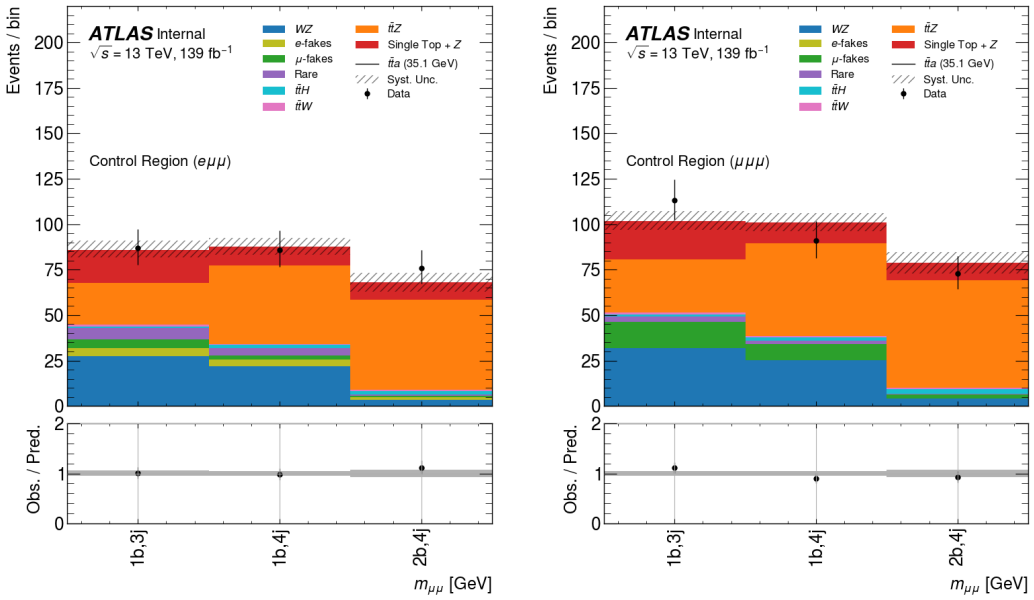

Figure 10.2: Comparison between data and expected background for the on-Z^0-boson control regions in the $e\mu\mu$ and $\mu\mu\mu$ final states.

The unblinded data, $t\bar{t}a$ simulation and the respective background processes for both

the signal regions, are shown in Figure 10.3[1]. The plots show the observed data, simulated background processes and the $t\bar{t}a$ simulation for two mass hypothesis, $m_a = 35.10$ GeV and $m_a = 51.90$ GeV.

Figure 10.4 shows the MLEs of the various nuisance parameters, related to the systematic uncertainties. In the figure, four different mass hypotheses are shown, $m_a = 21.7$, 35.1, 51.9 and 70.2 GeV. We can observe that there are no significant constraints in any of the nuisance parameters. This means that none of the systematic uncertainties play a major role in constraining the expected limit of the search. In addition to the constrained nuisance parameters, we also have four free-floating (unconstrained) parameters in the maximum likelihood fit. In this case, the MLEs are calculated for multiple sets of signal and background hypotheses, depending on the mass of the a-boson. Figure 10.5 shows the MLE for the unconstrained parameters, as a function of m_a. It is observed that the variation of the parameters are stable with respect to the various mass hypotheses.

In order to visualize the impact of the constrained and unconstrained parameters on the signal significance (μ in Figure 10.6), we can calculate the difference in the MLE of the parameter of interest (here, μ), when a specific nuisance parameter is shifted by $\pm\Delta\hat{\theta}$ around their MLE value, $\hat{\theta}$. The impact values are shown in Figure 10.6, for constrained and unconstrained parameters separately. We observe that the largest impact arises from the muon efficiency uncertainties and the uncertainties from the unconstrained parameters

[1]Plots are not public and cannot be shared outside the context of this particular thesis.

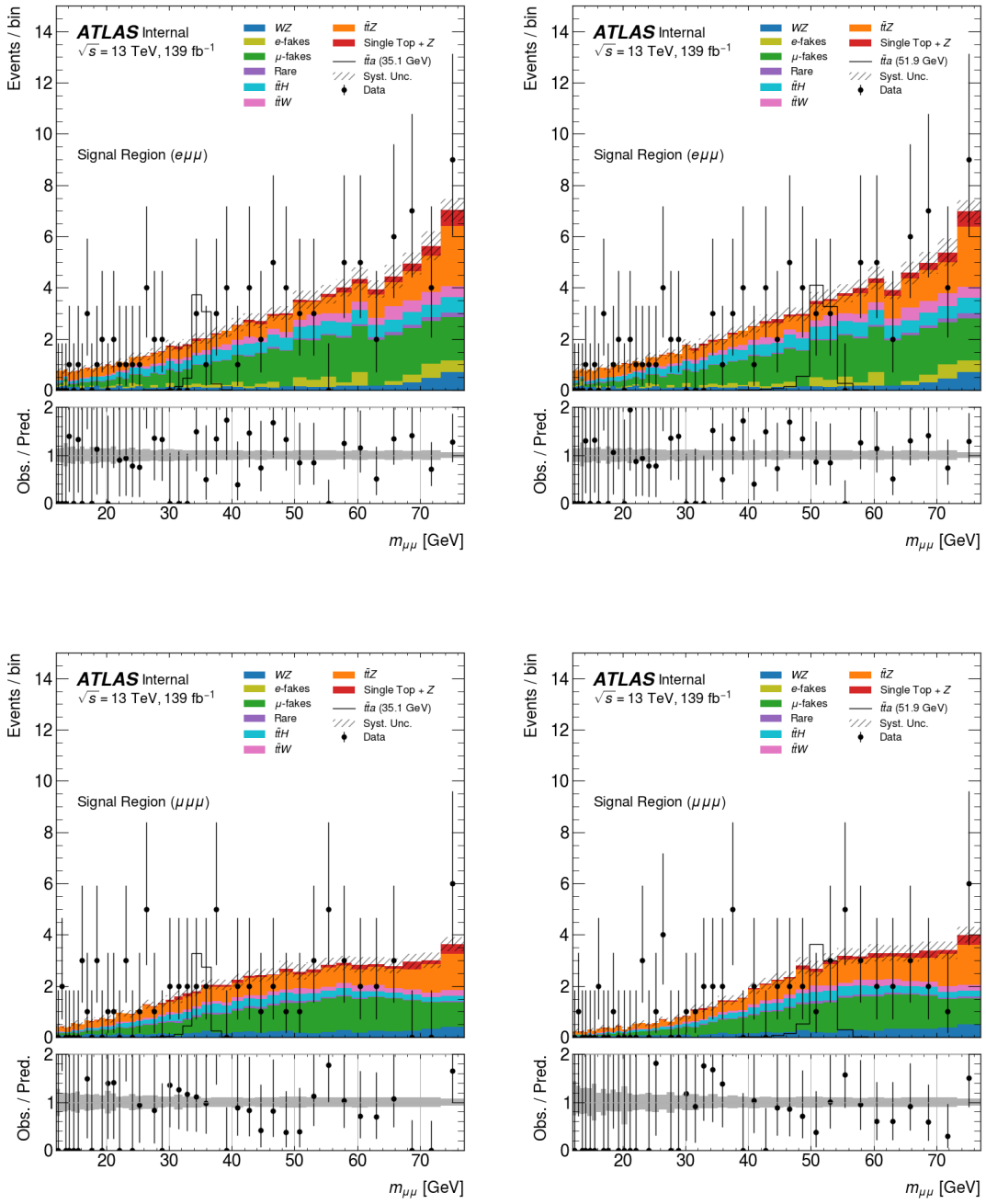

Figure 10.3: Signal region with data (unblinded) and background processes, for $m_a = 35.10$ GeV and $m_a = 51.90$ GeV is shown assuming $\sigma(t\bar{t}a)\mathrm{Br}(a \to \mu\mu) = 2$ fb, for $e\mu\mu$ SR (top) and $\mu\mu\mu$ SR (bottom). The value of 2 fb is arbitrary and is chosen solely for the purposes of visualization.

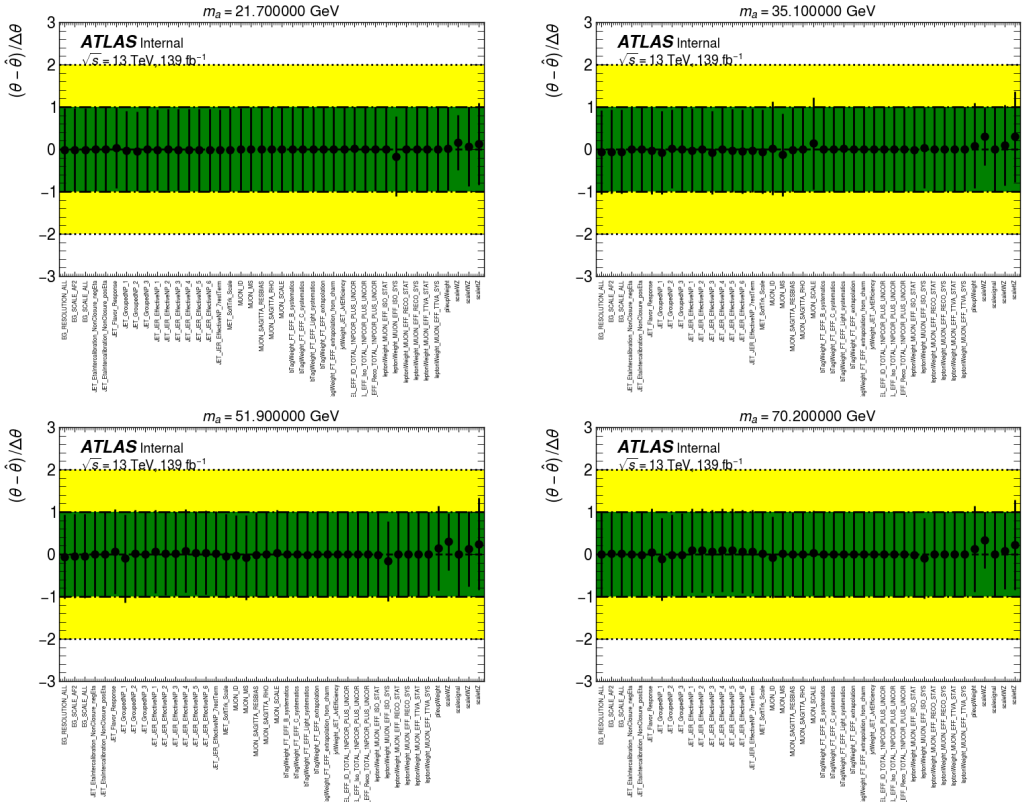

Figure 10.4: MLEs for the constrained nuisance parameters associated with systematic uncertainties from the fit of signal and background hypotheses for masses, m_a = 21.7, 35.1, 51.9 and 70.2 GeV.

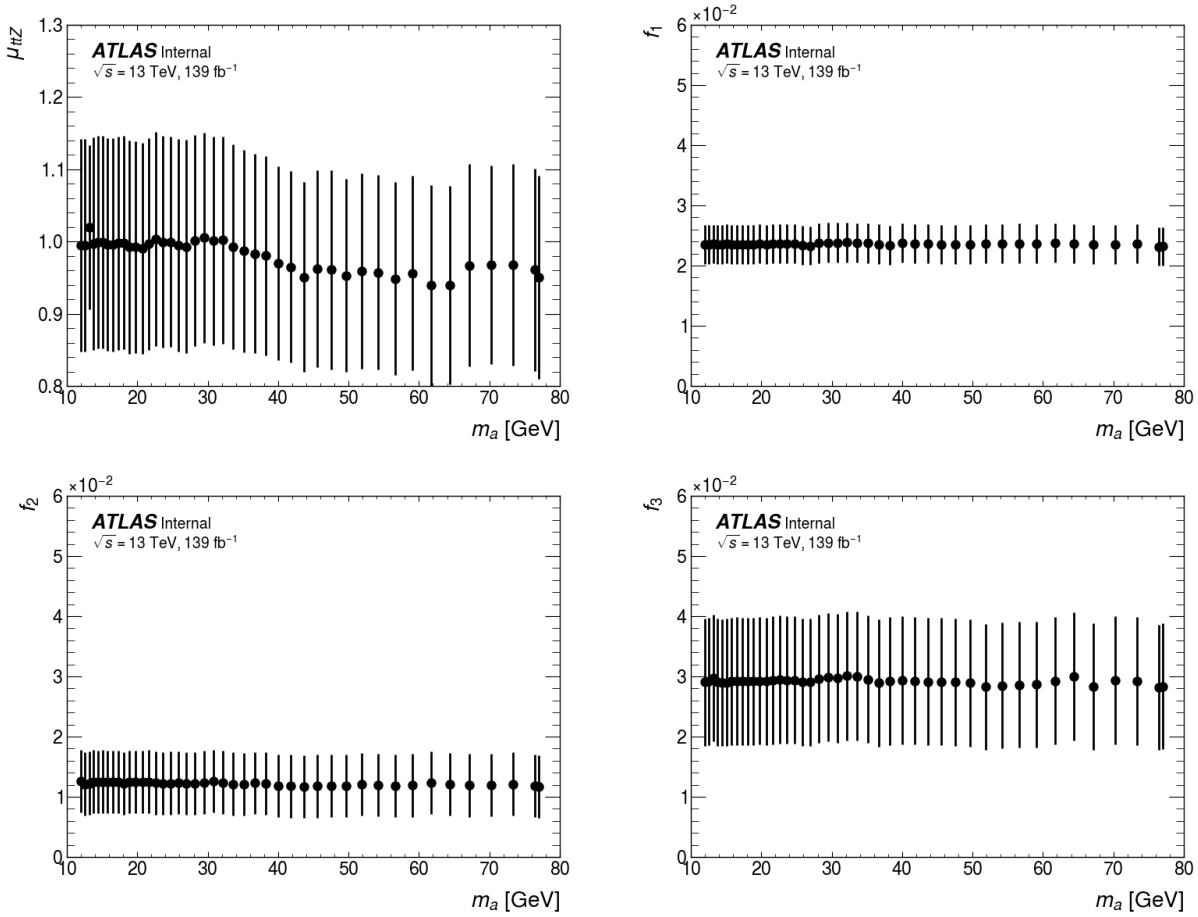

Figure 10.5: MLE for the unconstrained nuisance parameters associated to the $t\bar{t}Z$ normalization (top left) and fake factors (top right, bottom left, bottom right) for different mass hypotheses.

related to the normalization of the $t\bar{t}Z$ and non-prompt lepton backgrounds.

Figure 10.7[1] shows the corresponding signal significance as a function of the mass of the a-boson. As seen in the figure, there is no bin with local significance above 3σ in the dimuon mass range of 12 - 77 GeV. We observe the presence of a 2.4σ fluctuation around 27 GeV, which is not unlikely, given the number of trials in the analysis. The global significance has not been explicitly evaluated in this scenario. We observe no evidence of a $t\bar{t}a$ signal, hence a 95% confidence limit is set on the $\sigma(t\bar{t}a)\mathrm{Br}(a \to \mu\mu)$. Figure 10.8[1] shows the expected and observed limit for $\sigma(t\bar{t}a)\mathrm{Br}(a \to \mu\mu)$, considering the relevant statistical and systematic uncertainties. We expect to exclude a $t\bar{t}a$ signal at a value of $\sigma(t\bar{t}a)\mathrm{Br}(a \to \mu\mu) = 0.5$ - 3 fb, at a 95% confidence level, as seen in the figure.

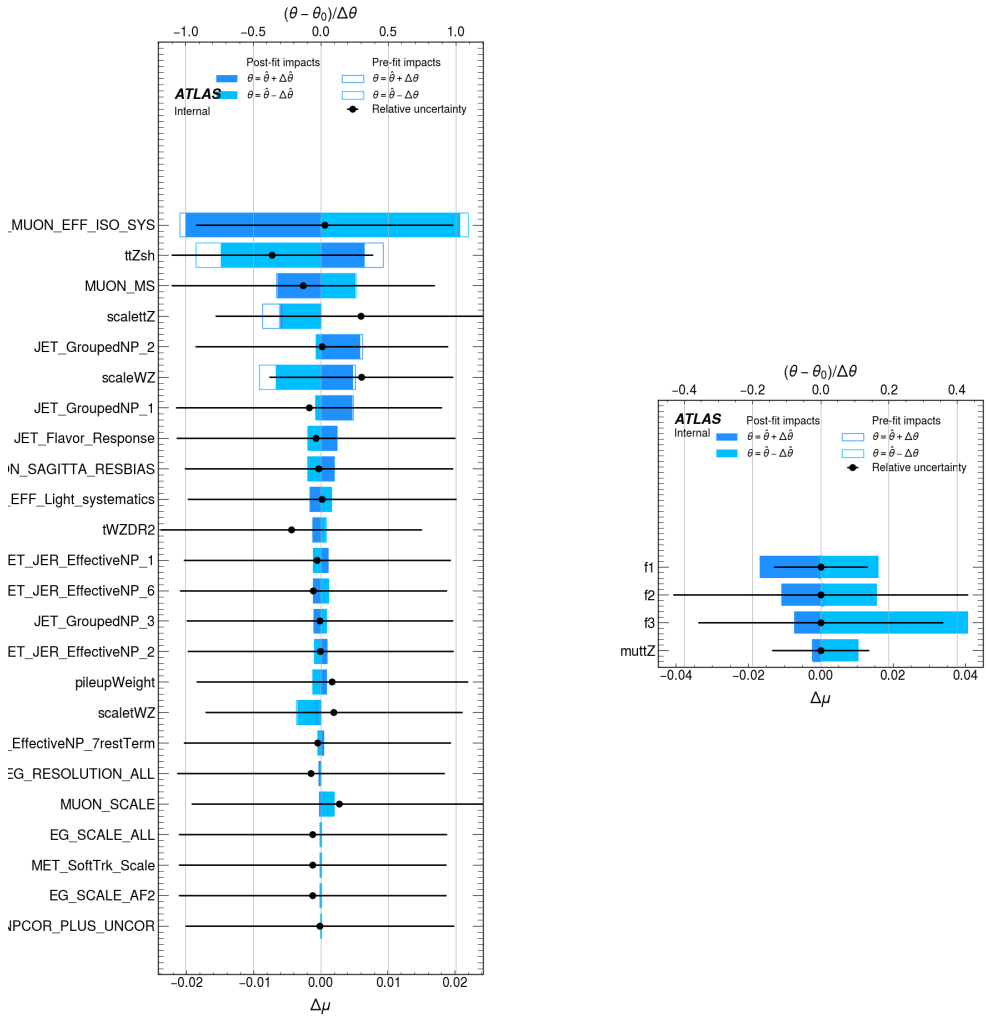

Figure 10.6: Impact of the constrained (left) and unconstrained (right) nuisance parameters in the parameter of interested μ, for $m_a = 35.10$ GeV.

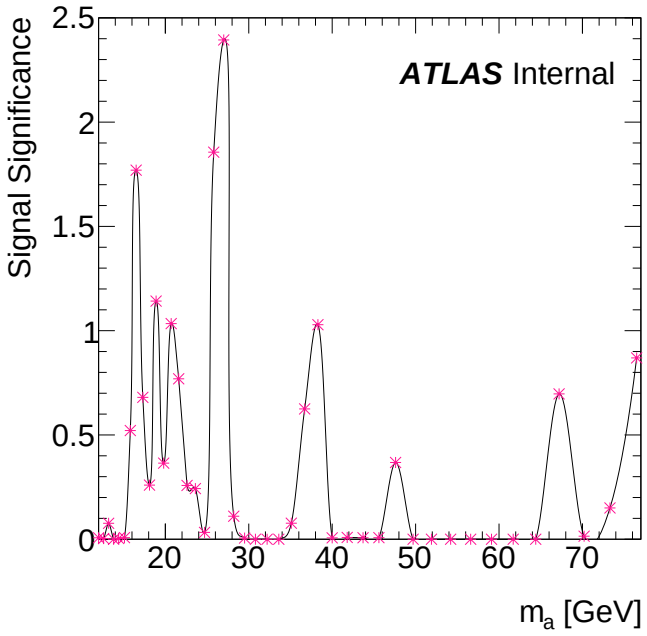

Figure 10.7: Signal significance is shown as a function of m_a.

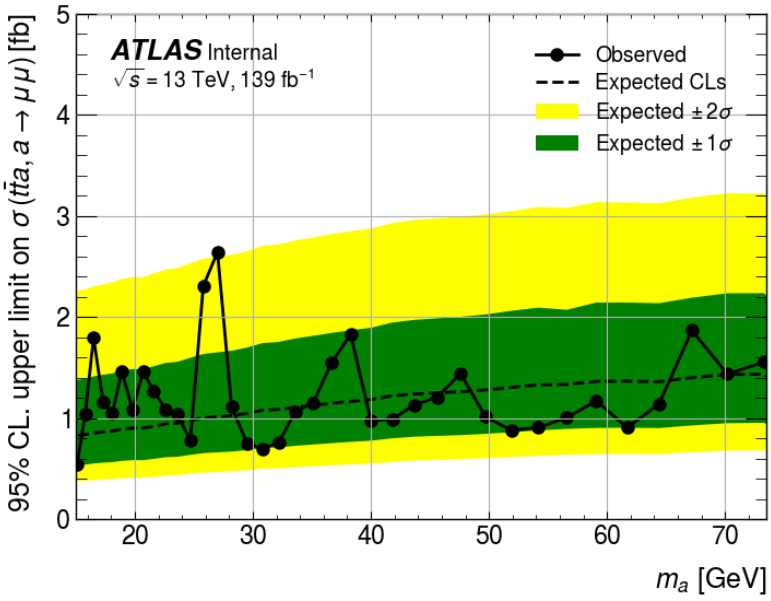

Figure 10.8: Observed upper limit on signal cross-section as a function of m_a, considering statistical and systematic uncertainties.

Chapter 11

Conclusion and Outlook

A search for a non SM pseduoscalar boson (a) produced in association with a top quark pair ($t\bar{t}$), is presented in this thesis. The decay of the a-boson is chosen to be a pair of muons and two distinct signal regions are studied, based on the flavour of the lepton originating from one of decays of the top quark. The invariant dimuon mass range for the targeted a-boson is set between 12 - 77 GeV.

Several sources of Standard Model physics processes are studied, which form the potential background sources for the analysis. The two signal regions, $e\mu\mu$ and $\mu\mu\mu$ are designed to maximise signal efficiency, and the dominant backgrounds are estimated from simulation as well as data. A dedicated statistical model is built in order to include statistical and systematic uncertainties. Maximum likelihood method approach is used to maximise the likelihood of achieving a $t\bar{t}a$ signal, and expected and observed exclusion limits on the value

of $\sigma(t\bar{t}a)\text{Br}(a \to \mu\mu)$ as well as the signal significance are presented as a function of m_a. As seen previously, we expect to exclude a $t\bar{t}a$ signal at a value of $\sigma(t\bar{t}a)\text{Br}(a \to \mu\mu) = 0.5$ - 3 fb, at a 95% confidence level, within 12 - 77 GeV dimuon mass range. This is the first-of-its kind search for this unique topology within the ATLAS collaboration.

The results presented in this thesis are currently undergoing review within the ATLAS collaboration, and are targeted for a journal publication in the near future, hence this is a private unblinding of data, which is highly confidential. Inclusion of systematic uncertainties in the limit calculation, evaluation of the global significance, using the look-elsewhere effect, will be completed in the future. This search targets a 3-lepton final state of $e\mu\mu$ and $\mu\mu\mu$ in $t\bar{t}$ events, which can be sensitive to other Beyond Standard Model searches. Hence, these results will be re-cast into various models with a similar signature, specifically, $t\bar{t} \to b\bar{b}H^+W^-, H^+ \to aW^+, a \to \mu^+\mu^-$. Other analyses which target a different decay mode for the a-boson, $a \to b\bar{b}$ and $a \to \tau\tau$ decays, can be used as a combination result, along with the muon decay channel. Another interesting addition to the present analysis will be to include a scalar interpretation for the a-boson, but is beyond the scope of this thesis.

Appendix A

Binning of dimuon mass spectrum

The following array of numbers (in GeV) shows the steps in which the binning of the dimuon invariant mass spectrum is optimised, based on details provided in Chapter 7.1.

$$\begin{aligned}\text{bin edges} = \{&12.0, 12.6, 13.2, 13.8, 14.4, 15.1, 15.8, 16.5, 17.3, 18.1, 18.9, 19.8, 20.7, 21.6, 22.6,\\ &23.6, 24.7, 25.8, 27.0, 28.2, 29.5, 30.8, 32.2, 33.6, 35.1, 36.7, 38.3, 40.0, 41.8, 43.7,\\ &45.6, 47.6, 49.7, 51.9, 54.2, 56.6, 59.1, 61.7, 64.4, 67.2, 70.2, 73.3, 76.5, 77.0\}\end{aligned}$$

Appendix B

Signal Fits

The full set of Double Crystal Ball fits for all the simulated $t\bar{t}a$ samples are presented as follows:

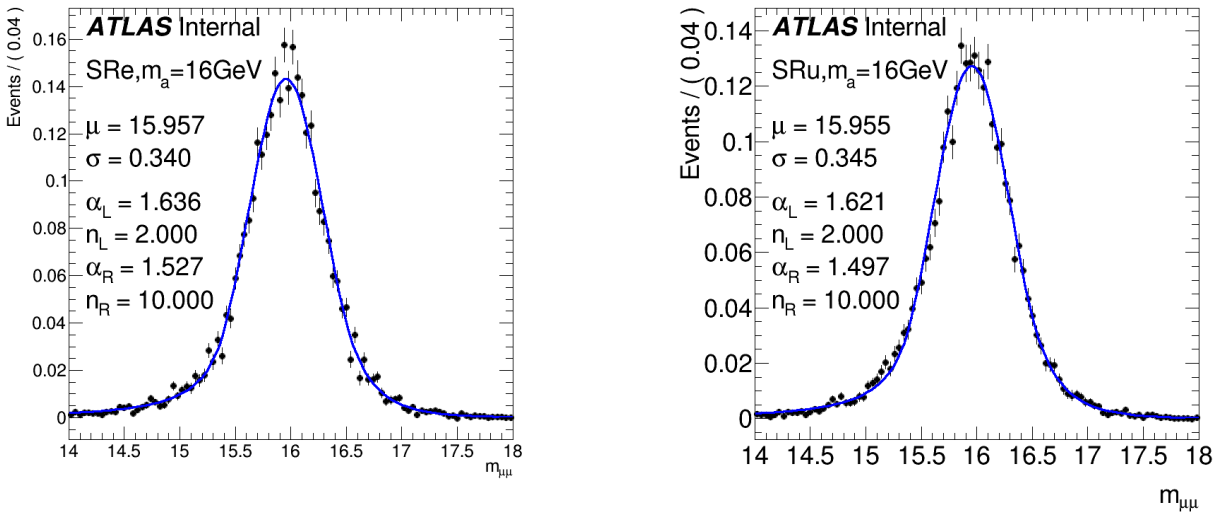

Figure B.1: Dimuon invariant mass peak for $t\bar{t}a$ simulation, $m_a = 16$ GeV in $e\mu\mu$ (left) and $\mu\mu\mu$ (right) regions.

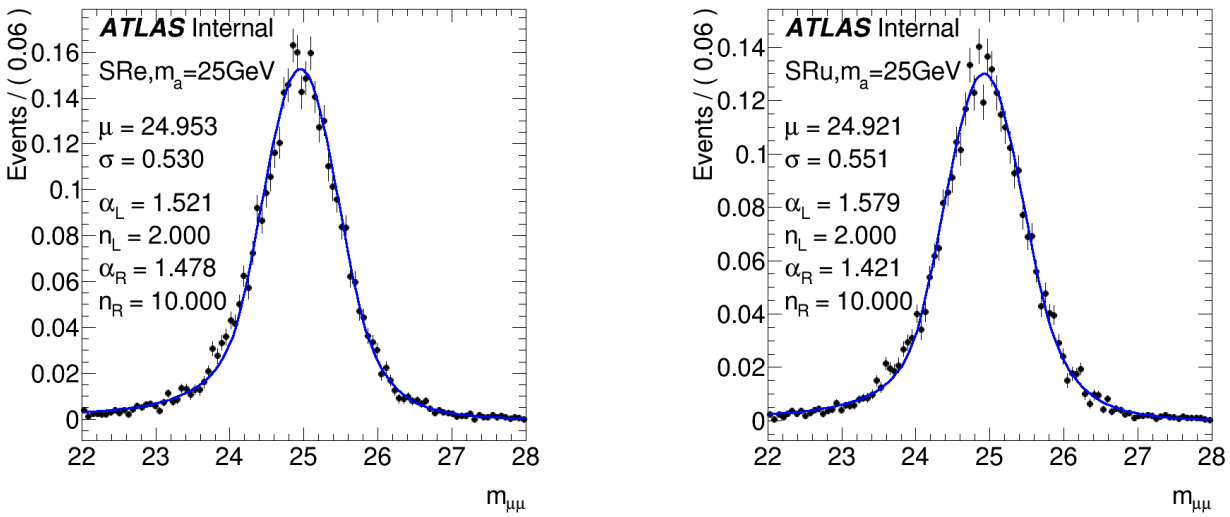

Figure B.2: Dimuon invariant mass peak for $t\bar{t}a$ simulation, $m_a = 25$ GeV in $e\mu\mu$ (left) and $\mu\mu\mu$ (right) regions.

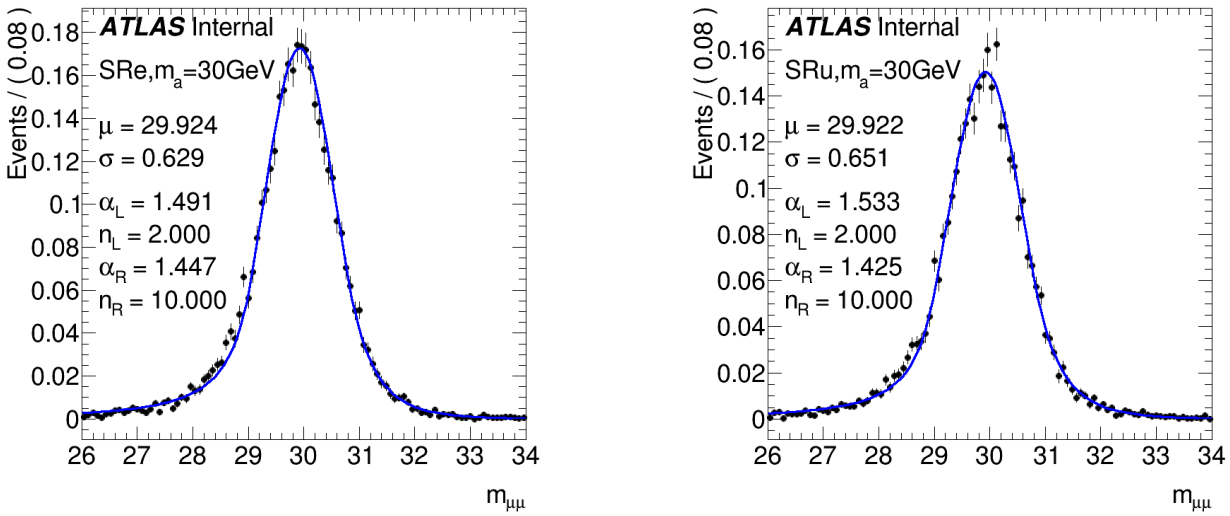

Figure B.3: Dimuon invariant mass peak for $t\bar{t}a$ simulation, $m_a = 30$ GeV in $e\mu\mu$ (left) and $\mu\mu\mu$ (right) regions.

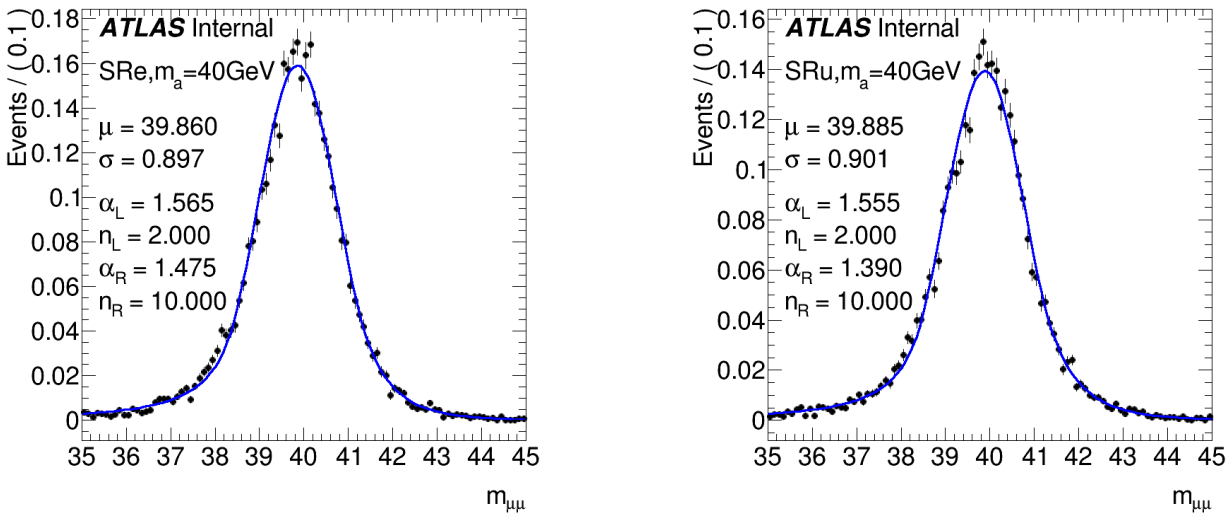

Figure B.4: Dimuon invariant mass peak for $t\bar{t}a$ simulation, $m_a = 40$ GeV in $e\mu\mu$ (left) and $\mu\mu\mu$ (right) regions.

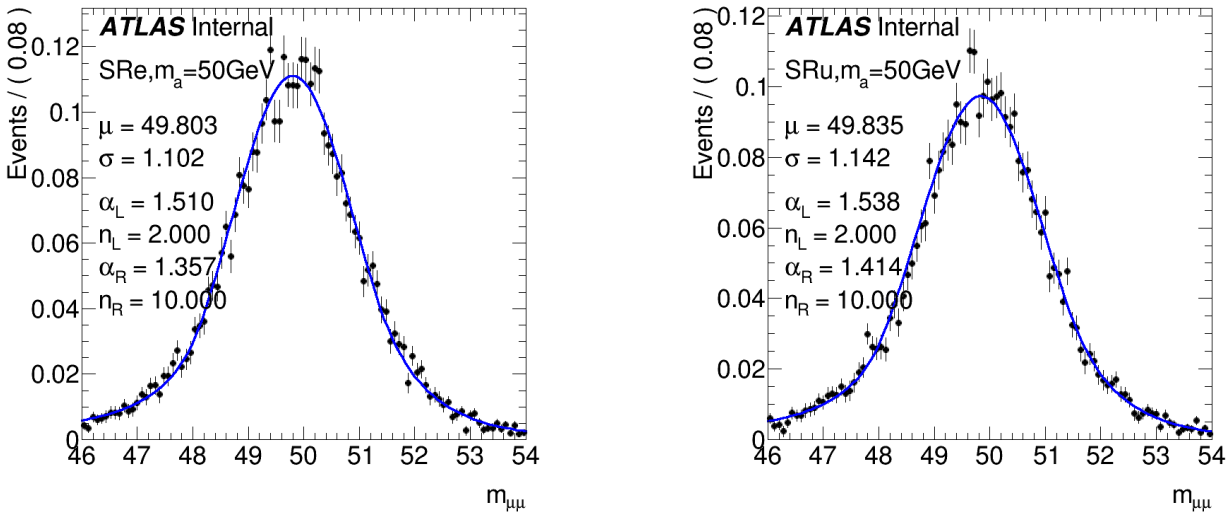

Figure B.5: Dimuon invariant mass peak for $t\bar{t}a$ simulation, $m_a = 50$ GeV in $e\mu\mu$ (left) and $\mu\mu\mu$ (right) regions.

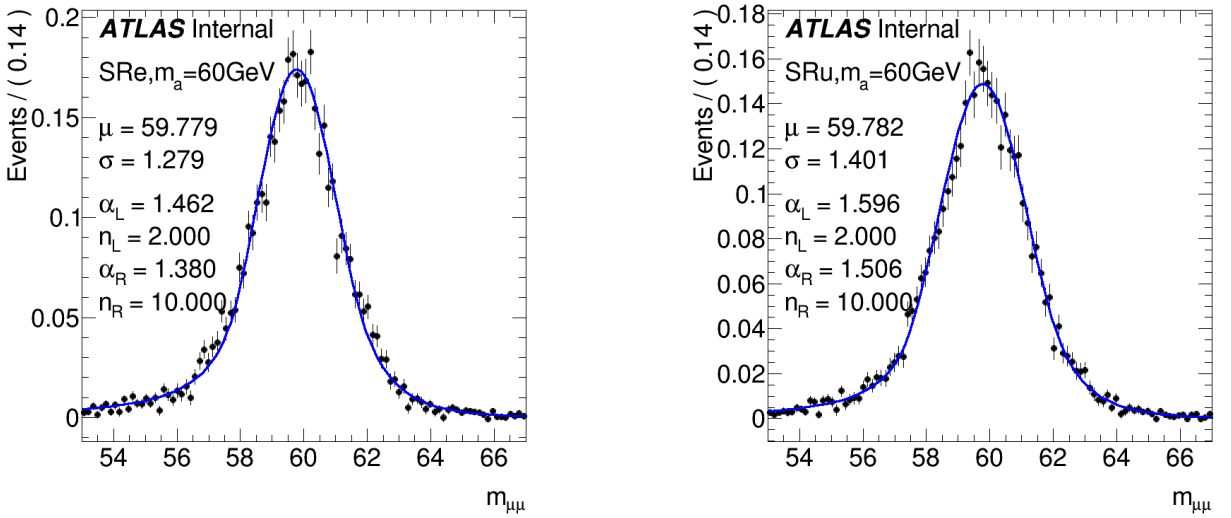

Figure B.6: Dimuon invariant mass peak for $t\bar{t}a$ simulation, $m_a = 60$ GeV in $e\mu\mu$ (left) and $\mu\mu\mu$ (right) regions.

Appendix C

Cutflow Tables

Cutflow tables for two signal masses $m_a = 20$ GeV and $m_a = 60$ GeV, and the main background, $t\bar{t}Z$, have been made for both the $e\mu\mu$ and $\mu\mu\mu$ channels. The term "pass xAOD cuts" refers to event cleaning, harmonized across analyses in the collaboration, and a requirement of at least 2 *Medium* quality muons with $p_T > 10$ GeV, $|z_0 \sin\theta| < 0.5$mm.

Table C.2 show the cutflow for the muon channel. Two mass hypotheses are shown, near the two ends of the spectrum, $m_a = 20$ GeV and the $m_a = 60$ GeV. The respective MC signal $t\bar{t}Z$ samples are used for the masses of a. The cutflow for $t\bar{t}Z$ is shown for both the mass hypotheses.

$e\mu\mu$-channel	m_a=20 GeV		m_a=60 GeV		$t\bar{t}Z$	
Signal Region selection	**Events**	**Tot. Eff.**	**Events**	**Tot. Eff.**	**Events**	**Tot. Eff.**
pass xAOD cuts	51.58	1	58.91	1	3864.14	1
2 loose muons	34.49	66.87	38.55	65.44	3105.55	80.36
$p_T(\mu_1, \mu_2) > (15, 10)$ GeV	34.39	66.67	38.54	65.42	3099.23	80.20
$N_{\text{jets}} \geq 3$	29.20	56.61	33.0	56.01	2840.60	73.51
$N_{b-\text{jets}} >= 1$	25.77	49.96	29.11	49.41	2451.78	63.45
1 electron	6.44	12.49	7.55	12.81	309.82	8.02
electron $p_T > 27$ GeV	6.44	12.49	7.55	12.81	309.81	8.02
Trigger matching	5.66	10.97	6.66	11.31	277.05	7.16
Electron isolation	5.05	9.79	6.0	10.18	243.90	6.31
Electron $d_{0\text{sig}}$	5.04	9.77	5.98	10.15	242.50	6.28
2 OS tight muons	3.56	6.90	4.60	7.81	170.69	4.42
$12 < m_a < 77$ GeV	3.51	6.80	4.56	7.74	23.29	0.60

Table C.1: Cutflow for two signal mass points $t\bar{t}a$, $m_a = 20$ GeV and $m_a = 60$ GeV, as well as the dominant background $t\bar{t}Z$, for the electron channel $e\mu\mu$. For the signal yields, a cross section times branching ratio of $\sigma(t\bar{t}a)\text{Br}(a \to \mu\mu) = 1$ fb is assumed. The total efficiency is shown as a percentage. The yields are shown for simulations.

$\mu\mu\mu$-channel	m_a=20 GeV		$t\bar{t}Z$, 20 GeV		m_a=60 GeV		$t\bar{t}Z$, 60 GeV	
Signal Region selection	**Events**	**Tot. Eff.**	**Events**	**Tot. Eff.**	**Events**	**Tot. Eff.**	**Events**	**Tot. Eff.**
pass xAOD cuts	51.81	1	3875.31	1	59.17	1	3875.31	1
3 loose muons	15.75	30.39	703.84	18.16	18.73	31.65	703.84	18.16
$N_{jets} \geq 3$	12.22	23.59	575.66	14.85	14.59	24.66	575.66	14.85
$N_{b\text{-jets}} \geq 1$	10.80	20.85	493.78	12.74	12.83	21.68	493.78	12.74
2 OS tight muons	10.02	19.34	434.33	11.21	12.19	20.60	434.33	11.21
$p_T(\mu_1^a, \mu_2^a) > (15, 10)$ GeV	9.98	19.26	430.77	11.12	12.18	20.58	433.31	11.18
$p_T(\mu^{\text{top}}) \geq 27$ *GeV* and trigger matched	6.27	12.10	296.49	7.65	7.53	12.73	291.32	7.52
$12 < m_{\mu\mu}^a < 77$ GeV								
$m_{\mu\mu}^{other} \leq 77$ or ≥ 107 GeV	3.56	6.87	21.79	0.56	4.48	7.57	22.48	0.58

Table C.2: Cutflow for two signal mass points $t\bar{t}a$, $m_a = 20$ GeV and $m_a = 60$ GeV, as well as the dominant background $t\bar{t}Z$ for each of the two signal mass hypotheses, for the muon channel $\mu\mu\mu$. For the signal yields, a cross section times branching ratio of $\sigma(t\bar{t}a)\text{Br}(a \to \mu\mu) = 1$ fb is assumed. The total efficiency is shown as a percentage. The yields are shown for simulations.

Bibliography

[1] Lisa Goodenough and Dan Hooper. "Possible Evidence For Dark Matter Annihilation In The Inner Milky Way From The Fermi Gamma Ray Space Telescope". In: (Oct. 2009). arXiv: 0910.2998 [hep-ph].

[2] Dan Hooper and Lisa Goodenough. "Dark Matter Annihilation in The Galactic Center As Seen by the Fermi Gamma Ray Space Telescope". In: *Phys. Lett. B* 697 (2011), pp. 412–428. DOI: 10.1016/j.physletb.2011.02.029. arXiv: 1010.2752 [hep-ph].

[3] Kevork N. Abazajian and Manoj Kaplinghat. "Detection of a Gamma-Ray Source in the Galactic Center Consistent with Extended Emission from Dark Matter Annihilation and Concentrated Astrophysical Emission". In: *Phys. Rev. D* 86 (2012). [Erratum: Phys.Rev.D 87, 129902 (2013)], p. 083511. DOI: 10.1103/PhysRevD.86.083511. arXiv: 1207.6047 [astro-ph.HE].

[4] Tansu Daylan et al. "The characterization of the gamma-ray signal from the central Milky Way: A case for annihilating dark matter". In: *Phys. Dark Univ.* 12 (2016), pp. 1–23. DOI: 10.1016/j.dark.2015.12.005. arXiv: 1402.6703 [astro-ph.HE].

[5] Céline Boehm et al. “Extended gamma-ray emission from Coy Dark Matter”. In: *JCAP* 05 (2014), p. 009. DOI: 10.1088/1475-7516/2014/05/009. arXiv: 1401.6458 [hep-ph].

[6] Andi Hektor and Luca Marzola. “Coy Dark Matter and the anomalous magnetic moment”. In: *Phys. Rev. D* 90.5 (2014), p. 053007. DOI: 10.1103/PhysRevD.90.053007. arXiv: 1403.3401 [hep-ph].

[7] Chiara Arina, Eugenio Del Nobile, and Paolo Panci. “Dark Matter with Pseudoscalar-Mediated Interactions Explains the DAMA Signal and the Galactic Center Excess”. In: *Phys. Rev. Lett.* 114 (2015), p. 011301. DOI: 10.1103/PhysRevLett.114.011301. arXiv: 1406.5542 [hep-ph].

[8] Stefano Profumo et al. “Singlet Higgs phenomenology and the electroweak phase transition”. In: *JHEP* 08 (2007), p. 010. DOI: 10.1088/1126-6708/2007/08/010. arXiv: 0705.2425 [hep-ph].

[9] Karim Ghorbani and Parsa Hossein Ghorbani. “Strongly First-Order Phase Transition in Real Singlet Scalar Dark Matter Model”. In: *J. Phys. G* 47.1 (2020), p. 015201. DOI: 10.1088/1361-6471/ab4823. arXiv: 1804.05798 [hep-ph].

[10] Tania Robens and Tim Stefaniak. “Status of the Higgs Singlet Extension of the Standard Model after LHC Run 1”. In: *Eur. Phys. J. C* 75 (2015), p. 104. DOI: 10.1140/epjc/s10052-015-3323-y. arXiv: 1501.02234 [hep-ph].

[11] Figure obtained from https://en.wikipedia.org/wiki/File:Standard_Model_of_Elementary_Particles.svg.

[12] C. Patrignani et al. "Review of Particle Physics". In: *Chin. Phys.* C40.10 (2016), p. 100001. DOI: 10.1088/1674-1137/40/10/100001.

[13] Jochen Cammin. "Top Quark Physics at Hadron Colliders". In: *AIP Conference Proceedings* 828.1 (Apr. 2006). ISSN: 0094-243X. DOI: 10.1063/1.2197410. URL: https://www.osti.gov/biblio/20800071.

[14] Mark Srednicki. *Quantum Field Theory*. Cambridge University Press, 2007. DOI: 10.1017/CBO9780511813917.

[15] Sheldon L. Glashow. "Partial-symmetries of weak interactions". In: *Nuclear Physics* 22.4 (1961), pp. 579–588. ISSN: 0029-5582. DOI: https://doi.org/10.1016/0029-5582(61)90469-2. URL: https://www.sciencedirect.com/science/article/pii/0029558261904692.

[16] Steven Weinberg. "A Model of Leptons". In: *Phys. Rev. Lett.* 19 (21 Nov. 1967), pp. 1264–1266. DOI: 10.1103/PhysRevLett.19.1264. URL: https://link.aps.org/doi/10.1103/PhysRevLett.19.1264.

[17] Cliff Burgess and Guy Moore. *The Standard Model: A Primer*. Cambridge University Press, 2006. DOI: 10.1017/CBO9780511819698.

[18] David J. Gross and Frank Wilczek. "Ultraviolet Behavior of Non-Abelian Gauge Theories". In: *Phys. Rev. Lett.* 30 (26 June 1973), pp. 1343–1346. DOI: 10.1103/PhysRevLett.30.1343.

[19] B.C. Allanach et al. "SUSY Parameter Analysis at TeV and Planck Scales". In: *Nuclear Physics B - Proceedings Supplements* 135 (2004), pp. 107–113. ISSN: 0920-5632. DOI: https://doi.org/10.1016/j.nuclphysbps.2004.09.052. URL: https://www.sciencedirect.com/science/article/pii/S0920563204003512.

[20] T Nakano and K Nishijima. "Charge independence for V-particles". In: *Progr. Theoret. Phys. (Japan)* Vol: 10 (Nov. 1953). DOI: 10.1143/PTP.10.581. URL: https://www.osti.gov/biblio/4411995.

[21] F. Englert and R. Brout. "Broken Symmetry and the Mass of Gauge Vector Mesons". In: *Phys. Rev. Lett.* 13 (9 Aug. 1964), pp. 321–323. DOI: 10.1103/PhysRevLett.13.321. URL: https://link.aps.org/doi/10.1103/PhysRevLett.13.321.

[22] P.W. Higgs. "Broken symmetries, massless particles and gauge fields". In: *Physics Letters* 12.2 (1964), pp. 132–133. ISSN: 0031-9163. DOI: https://doi.org/10.1016/0031-9163(64)91136-9. URL: https://www.sciencedirect.com/science/article/pii/0031916364911369.

[23] John Ellis. *Higgs Physics*. 2013. DOI: 10.48550/ARXIV.1312.5672. URL: https://arxiv.org/abs/1312.5672.

[24] Nicola Cabibbo. "Unitary Symmetry and Leptonic Decays". In: *Phys. Rev. Lett.* 10 (12 June 1963), pp. 531–533. DOI: 10.1103/PhysRevLett.10.531. URL: https://link.aps.org/doi/10.1103/PhysRevLett.10.531.

[25] I.C. Brock and T. Schörner-Sadenius. *Physics at the Terascale*. Apr. 2011. DOI: 10.1002/9783527634965.

[26] Georges Aad et al. "Combined Measurement of the Higgs Boson Mass in p p Collisions at s= 7 and 8 TeV with the ATLAS and CMS Experiments". In: *Physical review letters* 114.19 (2015), p. 191803.

[27] John Ellis. "Beyond the standard model for hillwalkers". In: *arxiv hep-ph/9812235* (1998).

[28] R.D. Peccei and Helen Quinn. "CP Conservation in the Presence of Pseudoparticles". In: *Physical Review Letters - PHYS REV LETT* 38 (June 1977), pp. 1440–1443. DOI: 10.1103/PhysRevLett.38.1440.

[29] Roberto D Peccei. "The Strong CP problem and axions". In: *Axions*. Springer, 2008, pp. 3–17.

[30] Daniele Alves et al. "Simplified models for LHC new physics searches". In: *Journal of Physics G: Nuclear and Particle Physics* 39.10 (2012), p. 105005.

[31] Tania Robens. "The THDMa Revisited". In: *Symmetry* 13.12 (2021), p. 2341. DOI: 10.3390/sym13122341. arXiv: 2106.02962 [hep-ph].

[32] Mirkoantonio Casolino et al. “Probing a light CP-odd scalar in di-top-associated production at the LHC”. In: *Eur. Phys. J. C* 75 (2015), p. 498. DOI: 10.1140/epjc/s10052-015-3708-y. arXiv: 1507.07004 [hep-ph].

[33] We-Fu Chang et al. “Signal for a light singlet scalar at the LHC”. In: *Phys. Rev. D* 97.5 (2018), p. 055020. DOI: 10.1103/PhysRevD.97.055020. arXiv: 1711.05722 [hep-ph].

[34] Clifford Cheung et al. “NMSSM Interpretation of the Galactic Center Excess”. In: *Phys. Rev. D* 90.7 (2014), p. 075011. DOI: 10.1103/PhysRevD.90.075011. arXiv: 1406.6372 [hep-ph].

[35] Jinrui Huang et al. “Supersymmetric subelectroweak scale dark matter, the Galactic Center gamma-ray excess, and exotic decays of the 125 GeV Higgs boson”. In: *Phys. Rev. D* 90.11 (2014), p. 115006. DOI: 10.1103/PhysRevD.90.115006. arXiv: 1407.0038 [hep-ph].

[36] Figure obtained from https://twiki.cern.ch/twiki/bin/view/{ATLAS}Public/LuminosityPublicResults#2012_data.

[37] Figure obtained from https://twiki.cern.ch/twiki/bin/view/ATLASPublic/LuminosityPublicResultsRun2.

[38] ATLAS Collaboration. “The ATLAS Experiment at the CERN Large Hadron Collider”. In: *Journal of Instrumentation* 3.08 (2008), S08003–S08003. DOI: 10.1088/1748-0221/3/08/s08003.

[39] CMS Collaboration. “The CMS experiment at the LHC”. In: *Journal of Instrumentation* 3.08 (Aug. 2008), S08004–S08004. DOI: 10.1088/1748-0221/3/08/s08004.

[40] LHCb Collaboration. “The LHCb Detector at the LHC”. In: *Journal of Instrumentation* 3.08 (Aug. 2008), S08005–S08005. DOI: 10.1088/1748-0221/3/08/s08005.

[41] The ALICE Collaboration. “The ALICE experiment at the CERN LHC. A Large Ion Collider Experiment”. In: *JINST* 3 (2008). Also published by CERN Geneva in 2010, S08002. 259 p. DOI: 10.1088/1748-0221/3/08/S08002.

[42] Christiane Lefèvre. “The CERN accelerator complex. Complexe des accélérateurs du CERN”. 2008. URL: https://cds.cern.ch/record/1260465.

[43] Andreas Hoecker. “Physics at the LHC Run-2 and Beyond”. In: *2016 European School of High-Energy Physics (ESHEP 2016) Skeikampen, Norway, June 15-28, 2016*. 2016. arXiv: 1611.07864 [hep-ex]. URL: https://inspirehep.net/record/1499881/files/arXiv:1611.07864.pdf.

[44] Joao Pequenao. “Computer generated image of the whole ATLAS detector”. 2008. URL: https://cds.cern.ch/record/1095924.

[45] Joao Pequenao. “Computer generated image of the ATLAS inner detector”. 2008. URL: https://cds.cern.ch/record/1095926.

[46] Alessandro La Rosa. “The ATLAS Insertable B-Layer: from construction to operation”. In: *JINST* 11.12 (2016), p. C12036. DOI: 10.1088/1748-0221/11/12/C12036. arXiv: 1610.01994 [physics.ins-det].

[47] Vasiliki A. Mitsou. “The ATLAS transition radiation tracker”. In: *Astroparticle, particle and space physics, detectors and medical physics applications. Proceedings, 8th Conference, ICATPP 2003, Como, Italy, October 6-10, 2003*. 2003, pp. 497–501. DOI: 10.1142/9789812702708_0073. arXiv: hep-ex/0311058 [hep-ex]. URL: http://weblib.cern.ch/abstract?ATL-CONF-2003-012.

[48] C. W. Fabjan and F. Gianotti. “Calorimetry for particle physics”. In: *Reviews of Modern Physics* 75 (Oct. 2003), pp. 1243–1286. DOI: 10.1103/RevModPhys.75.1243.

[49] Joao Pequenao. “Computer Generated image of the ATLAS calorimeter”. 2008. URL: https://cds.cern.ch/record/1095927.

[50] Paolo Francavilla and on behalf of the ATLAS Collaboration. “The ATLAS Tile Hadronic Calorimeter performance at the LHC”. In: *Journal of Physics: Conference*

Series 404.1 (2012), p. 012007. URL: http://stacks.iop.org/1742-6596/404/i=1/a=012007.

[51] Claus Grupen and Boris Shwartz. *Particle Detectors ,2nd Edition*. Cambridge Monographs on Particle Physics, Nuclear Physics and Cosmology, 2008.

[52] Joao Pequenao. "Computer generated image of the ATLAS Muons subsystem". 2008. URL: https://cds.cern.ch/record/1095929.

[53] Sandro Palestini. "The muon spectrometer of the ATLAS experiment". In: *Nuclear Physics B - Proceedings Supplements* 125 (2003). Innovative Particle and Radiation Detectors, pp. 337–345. ISSN: 0920-5632. DOI: https://doi.org/10.1016/S0920-5632(03)91013-9. URL: https://www.sciencedirect.com/science/article/pii/S0920563203910139.

[54] "ATLAS muon spectrometer: Technical Design Report". In: Technical design report. ATLAS (1997). URL: https://cds.cern.ch/record/331068.

[55] Andrew Hamilton. "The ATLAS Trigger System Commissioning and Performance". In: *Hadron collider physics. Proceedings, 22nd Conference, H2010, Toronto, Canada, August 23-27, 2010*. 2010. arXiv: 1010.0017 [physics.ins-det]. URL: https://inspirehep.net/record/871608/files/arXiv:1010.0017.pdf.

[56] C Ay et al. “Monte Carlo generators in ATLAS software”. In: *Journal of Physics: Conference Series* 219.3 (2010), p. 032001. URL: http://stacks.iop.org/1742-6596/219/i=3/a=032001.

[57] Torbjörn Sjöstrand et al. “An Introduction to PYTHIA 8.2”. In: *Comput. Phys. Commun.* 191 (2015), pp. 159–177. DOI: 10.1016/j.cpc.2015.01.024. arXiv: 1410.3012 [hep-ph].

[58] M. Bahr et al. “Herwig++ Physics and Manual”. In: *Eur. Phys. J.* C58 (2008), pp. 639–707. DOI: 10.1140/epjc/s10052-008-0798-9. arXiv: 0803.0883 [hep-ph].

[59] T. Gleisberg et al. “Event generation with SHERPA 1.1”. In: *JHEP* 02 (2009), p. 007. DOI: 10.1088/1126-6708/2009/02/007. arXiv: 0811.4622 [hep-ph].

[60] Stefano Frixione et al. “The MCaNLO 4.0 Event Generator”. In: (2010). arXiv: 1010.0819 [hep-ph].

[61] Carlo Oleari. “The POWHEG-BOX”. In: *Nucl. Phys. Proc. Suppl.* 205-206 (2010), pp. 36–41. DOI: 10.1016/j.nuclphysbps.2010.08.016. arXiv: 1007.3893 [hep-ph].

[62] S. M. Berman, J. D. Bjorken, and J. B. Kogut. “Inclusive Processes at High Transverse Momentum”. In: *Phys. Rev. D* 4 (11 Dec. 1971), pp. 3388–3418. DOI: 10.1103/PhysRevD.4.3388. URL: https://link.aps.org/doi/10.1103/PhysRevD.4.3388.

[63] F. Sauerburger. *LHC cross section plot*. Figure obtained from https://lhc-xsecs.org/.

[64] Stefan Höche. "Introduction to parton-shower event generators". In: *Theoretical Advanced Study Institute in Elementary Particle Physics: Journeys Through the Precision Frontier: Amplitudes for Colliders (TASI 2014) Boulder, Colorado, June 2-27, 2014*. 2014. arXiv: 1411.4085 [hep-ph]. URL: https://inspirehep.net/record/1328513/files/arXiv:1411.4085.pdf.

[65] B. R. Webber. "Fragmentation and hadronization". In: *Int. J. Mod. Phys.* A15S1 (2000). [eConfC990809,577(2000)], pp. 577–606. DOI: 10.1142/S0217751X00005334. arXiv: hep-ph/9912292 [hep-ph].

[66] S. Agostinelli et al. "GEANT4: A Simulation toolkit". In: *Nucl. Instrum. Meth.* A506 (2003), pp. 250–303. DOI: 10.1016/S0168-9002(03)01368-8.

[67] G. Aad et al. "Muon reconstruction performance of the ATLAS detector in proton–proton collision data at $\sqrt{s}$ =13 TeV". In: *The European Physical Journal C* 76.5 (May 2016). ISSN: 1434-6052. DOI: 10.1140/epjc/s10052-016-4120-y. URL: http://dx.doi.org/10.1140/epjc/s10052-016-4120-y.

[68] ATLAS Twiki. https://twiki.cern.ch/twiki/bin/viewauth/AtlasProtected/InDetTrackingDC14. (Accessed: 20.04.2022).

[69] ATLAS Isolation and Fake Forum. https://twiki.cern.ch/twiki/bin/view/AtlasProtected/Run2IsolationHarmonisation. 2019 (accessed June, 2019).

[70] W. Lampl et al. "Calorimeter Clustering Algorithms: Description and Performance". In: (Apr. 2008). URL: https://cds.cern.ch/record/1099735.

[71] M Aaboud et al. "Electron reconstruction and identification in the ATLAS experiment using the 2015 and 2016 LHC proton–proton collision data at $\sqrt{s} = 13$ TeV". In: *The European Physical Journal C* 79.8 (Aug. 2019). ISSN: 1434-6052. DOI: 10.1140/epjc/s10052-019-7140-6. URL: http://dx.doi.org/10.1140/epjc/s10052-019-7140-6.

[72] ATLAS Jet and Missing Energy Performance. https://twiki.cern.ch/twiki/bin/view/AtlasPublic/JetEtmissPublicResults?redirectedfrom=AtlasPublic.JetEtMissPublicCollisionResults.

[73] M Aaboud et al. "Jet reconstruction and performance using particle flow with the ATLAS Detector". In: *The European Physical Journal C* 77.7 (July 2017). ISSN: 1434-6052. DOI: 10.1140/epjc/s10052-017-5031-2. URL: http://dx.doi.org/10.1140/epjc/s10052-017-5031-2.

[74] *Tagging and suppression of pileup jets*. Tech. rep. Geneva: CERN, 2014. URL: https://cds.cern.ch/record/1643929.

[75] Figure obtained from https://amva4newphysics.wordpress.com/2016/01/04/b-tagging-101/.

[76] Georges Aad et al. "ATLAS b-jet identification performance and efficiency measurement with $t\bar{t}$ events in pp collisions at $\sqrt{s} = 13$ TeV". In: *Eur. Phys. J. C* 79.11 (2019), p. 970. DOI: 10.1140/epjc/s10052-019-7450-8. arXiv: 1907.05120 [hep-ex].

[77] Johan Alwall et al. "Searching for directly decaying gluinos at the Tevatron". In: *Phys. Lett. B* 666 (2008), p. 34. DOI: 10.1016/j.physletb.2008.06.065. arXiv: 0803.0019 [hep-ph].

[78] Richard D. Ball et al. "Parton distributions for the LHC run II". In: *JHEP* 04 (2015), p. 040. DOI: 10.1007/JHEP04(2015)040. arXiv: 1410.8849 [hep-ph].

[79] Torbjörn Sjöstrand et al. "An introduction to PYTHIA 8.2". In: *Comput. Phys. Commun.* 191 (2015), p. 159. DOI: 10.1016/j.cpc.2015.01.024. arXiv: 1410.3012 [hep-ph].

[80] D. J. Lange. "The EvtGen particle decay simulation package". In: *Nucl. Instrum. Meth. A* 462 (2001), p. 152. DOI: 10.1016/S0168-9002(01)00089-4.

[81] D. Costanzo et al. "The Geant4-Based Simulation Software of the ATLAS Detector". In: *2006 IEEE Nuclear Science Symposium Conference Record*. Vol. 1. 2006, pp. 5–11. DOI: 10.1109/NSSMIC.2006.356099.

[82] ATLAS Collaboration. *ATLAS Pythia 8 tunes to 7 TeV data*. ATL-PHYS-PUB-2014-021. 2014. URL: https://cds.cern.ch/record/1966419.

[83] Richard D. Ball et al. "Parton distributions with LHC data". In: *Nucl. Phys. B* 867 (2013), p. 244. DOI: 10.1016/j.nuclphysb.2012.10.003. arXiv: 1207.1303 [hep-ph].

[84] Enrico Bothmann et al. "Event generation with Sherpa 2.2". In: *SciPost Phys.* 7.3 (2019), p. 034. DOI: 10.21468/SciPostPhys.7.3.034. arXiv: 1905.09127 [hep-ph].

[85] ATLAS Collaboration. "Measurement of the Z/γ^* boson transverse momentum distribution in pp collisions at $\sqrt{s} = 7\,\text{TeV}$ with the ATLAS detector". In: *JHEP* 09 (2014), p. 145. DOI: 10.1007/JHEP09(2014)145. arXiv: 1406.3660 [hep-ex].

[86] ATLAS Physics Modelling Group. https://twiki.cern.ch/twiki/bin/view/ATLASProtected/PhysicsModellingGroup. 2022 (accessed April, 2022).

[87] Stefano Frixione et al. "A positive-weight next-to-leading-order Monte Carlo for heavy flavour hadroproduction". In: *JHEP* 09 (2007), p. 126. DOI: 10.1088/1126-6708/2007/09/126. arXiv: 0707.3088 [hep-ph].

[88] Paolo Nason. "A new method for combining NLO QCD with shower Monte Carlo algorithms". In: *JHEP* 11 (2004), p. 040. DOI: 10.1088/1126-6708/2004/11/040. arXiv: hep-ph/0409146.

[89] Stefano Frixione, Paolo Nason, and Carlo Oleari. "Matching NLO QCD computations with parton shower simulations: the POWHEG method". In: *JHEP* 11 (2007), p. 070. DOI: 10.1088/1126-6708/2007/11/070. arXiv: 0709.2092 [hep-ph].

[90] Simone Alioli et al. "A general framework for implementing NLO calculations in shower Monte Carlo programs: the POWHEG BOX". In: *JHEP* 06 (2010), p. 043. DOI: 10.1007/JHEP06(2010)043. arXiv: 1002.2581 [hep-ph].

[91] ATLAS Collaboration. *Studies on top-quark Monte Carlo modelling for Top2016*. ATL-PHYS-PUB-2016-020. 2016. URL: https://cds.cern.ch/record/2216168.

[92] "Search for $H^{\pm} \to W^{\pm}A \to W^{\pm}\mu\mu$ in $pp \to t\bar{t}$ events using an $e\mu\mu$ signature with the ATLAS detector at $\sqrt{s} = 13$ TeV". In: (Sept. 2021). URL: https://cds.cern.ch/record/2780092.

[93] M. Oreglia. "A Study of the Reactions $\psi' \to \gamma\gamma\psi$". Dec. 1980.

[94] Kyle Cranmer et al. *HistFactory: A tool for creating statistical models for use with RooFit and RooStats*. Tech. rep. New York: New York U., Jan. 2012. URL: https://cds.cern.ch/record/1456844.

[95] ATLAS Combined Performance Group. URL: https://twiki.cern.ch/twiki/bin/view/AtlasPublic/WebHome#Performance_Groups_Simulation_an.

[96] Rene Brun and Fons Rademakers. “ROOT - An Object Oriented Data Analysis Framework”. In: *Nucl. Inst. Meth. in Phys. Res. A* (1997), pp. 81–86. URL: https://root.cern/.

[97] “Luminosity determination in pp collisions at $\sqrt{s} = 13$ TeV using the ATLAS detector at the LHC”. In: (2019).

[98] ATLAS Collaboration. “Jet energy scale and resolution measured in proton-proton collisions at $\sqrt{s}$= 13 TeV with the ATLAS detector”. In: *arXiv:2007.02645* (2020).

[99] Morad Aaboud et al. “Jet energy scale measurements and their systematic uncertainties in proton-proton collisions at s= 13 TeV with the ATLAS detector”. In: *Physical Review D* 96.7 (2017), p. 072002.

[100] ATLAS Collaboration. “Configuration and performance of the ATLAS b-jet triggers in Run 2”. In: *arXiv:2106.03584* (2021).

[101] ATLAS Collaboration. “Measurements of b-jet tagging efficiency with the ATLAS detector using $t\bar{t}$ events at $\sqrt{s}$= 13 TeV”. In: *arXiv:1805.01845* (2018).

[102] ATLAS Collaboration. “Performance of missing transverse momentum reconstruction with the ATLAS detector using proton-proton collisions at $\sqrt{s}$= 13 TeV”. In: *arXiv:1802.08168* (2018).

[103] ATLAS Flavour Tagging Performance. https://twiki.cern.ch/twiki/bin/view/AtlasPublic/FlavourTaggingPublicResultsCollisionData.

[104] Georges Aad et al. “Electron and photon performance measurements with the ATLAS detector using the 2015–2017 LHC proton-proton collision data”. In: (2019).

[105] Thibault Guillemin et al. *Energy scale and resolution systematics: summary and correlations*. Tech. rep. Geneva: CERN, June 2017. URL: https://cds.cern.ch/record/2268796.

[106] ATLAS Electron and Photon Performance. https://twiki.cern.ch/twiki/bin/view/AtlasPublic/ElectronGammaPublicCollisionResults.

[107] Magnar Kopangen Bugge et al. *Muon Selection and Identification Working Points*. Tech. rep. Geneva: CERN, Mar. 2019. URL: https://cds.cern.ch/record/2665711.

[108] Georges Aad et al. “Muon reconstruction and identification efficiency in ATLAS using the full Run 2 pp collision data set at $\sqrt{s} = 13$ TeV”. In: *The European Physical Journal C* 81.7 (2021), pp. 1–44.

[109] ATLAS Muon Performance. URL: https://twiki.cern.ch/twiki/bin/view/AtlasPublic/MuonPublicResults.

[110] Frank Siegert et al. *Treatment of theory predictions in ATLAS*. Tech. rep. Geneva: CERN, Feb. 2018. URL: https://cds.cern.ch/record/2305435.

[111] Matteo Cacciari et al. “The $t\bar{t}$ cross-section at 1.8 and 1.96 TeV: a study of the systematics due to parton densities and scale dependence”. In: *Journal of High Energy Physics* 2004.04 (2004), p. 068.

[112] Johan Alwall et al. “A standard format for Les Houches event files”. In: *Computer Physics Communications* 176.4 (2007), pp. 300–304.

[113] Glen Cowan et al. “Asymptotic formulae for likelihood-based tests of new physics”. In: *The European Physical Journal C* 71.2 (2011), pp. 1–19.

[114] Lukas Heinrich et al. “pyhf: pure-Python implementation of HistFactory statistical models”. In: *Journal of Open Source Software* 6.58 (2021), p. 2823. DOI: 10.21105/joss.02823. URL: https://doi.org/10.21105/joss.02823.

[115] Lukas Heinrich, Matthew Feickert, and Giordon Stark. *pyhf: v0.7.0rc1*. Version 0.7.0rc1. https://github.com/scikit-hep/pyhf/releases/tag/v0.7.0rc1. DOI: 10.5281/zenodo.1169739. URL: https://doi.org/10.5281/zenodo.1169739.

[116] Kyle Cranmer. “Practical Statistics for the LHC”. In: *arXiv:1503.07622* (2015).

[117] Roger J. Barlow and Christine Beeston. “Fitting using finite Monte Carlo samples”. In: *Comput. Phys. Commun.* 77 (1993), pp. 219–228. DOI: 10.1016/0010-4655(93)90005-W.

[118] Thomas Junk. “Confidence level computation for combining searches with small statistics”. In: *Nucl. Instrum. Meth. A* 434 (1999), pp. 435–443. DOI: 10.1016/S0168-9002(99)00498-2. arXiv: hep-ex/9902006.

[119] Alexander L. Read. “Presentation of search results: the CL_S technique”. In: *J. Phys. G* 28 (2002), p. 2693. DOI: 10.1088/0954-3899/28/10/313.

[120] F. James and M. Roos. “Minuit - a system for function minimization and analysis of the parameter errors and correlations”. In: *Computer Physics Communications* 10.6 (1975), pp. 343–367. ISSN: 0010-4655. DOI: https://doi.org/10.1016/0010-4655(75)90039-9. URL: https://www.sciencedirect.com/science/article/pii/0010465575900399.